WIND/RAIN BACKSCATTER MODELING AND WIND/RAIN RETRIEVAL FOR SCATTEROMETER AND SYNTHETIC APERTURE RADAR

by

Congling Nie

A dissertation submitted to the faculty of

Brigham Young University

in partial fulfillment of the requirements for the degree of

Doctor of Philosophy

Department of Electrical and Computer Engineering

Brigham Young University

April 2008

BRIGHAM YOUNG UNIVERSITY

GRADUATE COMMITTEE APPROVAL

of a dissertation submitted by

Congling Nie

This dissertation has been read by each member of the following graduate committee and by majority vote has been found to be satisfactory.

Date	David G. Long, Chair
Date	Brain D. Jeffs
Date	Karl F. Warnick
Date	Richard W. Christiansen
Date	Dah-Jye Lee

BRIGHAM YOUNG UNIVERSITY

As chair of the candidate's graduate committee, I have read the dissertation of Congling Nie in its final form and have found that (1) its format, citations, and bibliographical style are consistent and acceptable and fulfill university and department style requirements; (2) its illustrative materials including figures, tables, and charts are in place; and (3) the final manuscript is satisfactory to the graduate committee and is ready for submission to the university library.

Date

David G. Long
Chair, Graduate Committee

Accepted for the Department

Michael J. Wirthlin
Graduate Coordinator

Accepted for the College

Alan R. Parkinson
Dean, Ira A. Fulton College of
Engineering and Technology

ABSTRACT

WIND/RAIN BACKSCATTER MODELING AND WIND/RAIN RETRIEVAL FOR SCATTEROMETER AND SYNTHETIC APERTURE RADAR

Congling Nie

Department of Electrical and Computer Engineering

Doctor of Philosophy

Using co-located space-borne satellite (TRMM PR, ESCAT on ERS 1/2) measurements, and numerical predicted wind fields (ECMWF), the sensitivity of C-band backscatter measurement to rain is evaluated. It is demonstrated that C-band radar backscatter can be significantly altered by rain surface perturbation, an effect that has been previously neglected. A low-order wind/rain backscatter model is developed that has inputs of surface rain rate, incidence angle, wind speed, wind direction, and azimuth angle. The wind/rain backscatter model is accurate enough for describing the total backscatter in raining areas with relatively low variance. Rain has a more significant impact on measurements at high incidence angles than at low incidence angles. Using three distinct regimes, the conditions for which wind, rain, and both wind and rain can be retrieved from scatterometer backscatter measurements are determined.

The effects of rain on ESCAT wind-only retrieval are evaluated. The additional scattering from rain causes estimated wind speeds to be biased high and estimated wind directions to be biased toward the along-track direction in heavy rains. To compensate for rain-induced backscatter, we develop a simultaneous wind/rain retrieval method (SWRR), which simultaneously estimates wind and rain from ESCAT backscatter measurements with an incidence angle of over 40 degrees. The performance of SWRR under typical wind/rain conditions is evaluated through simulation and validation with collocated TRMM PR and ECMWF data sets. SWRR is shown to significantly improve wind velocity estimates and the SWRR-estimated rain rate has relatively high accuracy in moderate to heavy rain cases.

RADARSAT-1 ScanSAR SWA images of Hurricane Katrina are used to retrieve surface wind vectors over the ocean. Collocated H*wind wind directions are used as the wind direction estimate and the wind speed is derived from SAR σ° by inversion of a C-band HH-polarization Geophysical Model Function (GMF) that is derived from the VV-polarization GMF, CMOD5, using a polarization ratio model. Because existing polarization models do not fit the ScanSAR SWA data well, a recalibration model is proposed to "recalibrate" the ScanSAR SWA images. Validated with collocated H*wind wind speed estimates, the mean difference between SAR-retrieved and H*wind speed is small and the root mean square (RMS) error is below 4 m/s. Rain effects on the ScanSAR measurements are analyzed for three different incidence angle ranges using collocated ground-based Doppler weather radar (NEXRAD) rain measurements. Compared with the scatterometer-derived model, the rain-induced backscatter observed by the ScanSAR at incidence angles $44^\circ - 45.7^\circ$ is consistent with the scatterometer-derived model when the polarization difference between HH and VV polarizations is considered.

ACKNOWLEDGMENTS

I want to thank my advisor, Dr. David Long, for his continuous guidance and vast support that help me to progress and advance. I am thankful to my committee members for their help during writing this dissertation.

Thank you to my wife, Jun, for her support and patience. Thank you to my parents for always encouraging me to work hard.

Table of Contents

List of Tables

List of Figures

Chapter 1

Introduction

Oceans contain the bulk of the water on Earth and cover approximately 70% of the Earth's surface. Since water has a significantly higher heat capacity than air or rocks, the majority of the thermal energy at the Earth surface is stored in the oceans; hence the large thermal inertia of the oceans is a key factor in stabilizing Earth's climate. Due to the important role of oceans in global energy circulation, meteorological observations including winds, rain rate, and surface pressure over the ocean are essential for understanding the global climate and setting up numerical weather prediction models.

Since conventional observations provided by ships and buoys are extremely limited and have sparse coverage, space-borne microwave remote sensing instruments, including scatterometers, provide a better understanding of the global ocean surface winds. A scatterometer is an instrument designed to provide high quality near-surface wind estimates over the ocean. The radar backscattering cross-section measurements acquired by the scatterometer are related to near-surface wind speed and direction. Current scatterometers cover 90% of the Earth's surface each day. Microwaves penetrate cloud over and are independent of solar illumination, providing accurate, all-weather measurements night and day.

Previous and contemporary scatterometers operate in Ku-band and C-band. The SeaWinds scatterometers on-board QuickSCAT and the Advanced Earth Observing Satellite (ADEOS II), launched in 1999 and 2003, respectively, are conically scanning Ku-band (14 GHz) radars. The C-band 5.3 GHz scatterometer mode (ESCAT) on European Remote Sensing (ERS) satellite utilizes fixed fan-beam antennas. ESCAT has a narrow swath (500 km), providing near-surface winds at 50 km res-

olution [1]. The newly launched Advanced Scatterometer Instrument (ASCAT) on Metop-A satellite uses a similar design but the swath width is extended to 1000 km.

Sensors, such as synthetic aperture radar (SAR), have been conventionally used to study coastal processes, currents, and sea ice at high spatial resolution. Over the ocean, SAR measurements can be related to the near-surface wind velocity using a model similar to that used in scatterometery. Compared to a scatterometer, SAR lacks azimuth diversity and thus wind speed and direction cannot be estimated directly. However, SAR has higher resolution and is thus useful for studying micro-scale weather events such as rain cells, currents, and tropical cyclones over the ocean.

1.1 Description of the Problem

For fair weather conditions (average sea state and absence of rain), a scatterometer backscatter measurement is mainly from wind-driven gravity-capillary waves (Bragg waves). The normalized radar backscattering cross-section is related to wind speed and wind direction through an empirical model, known as the Geophysical Model Function (GMF). Near-surface wind speed and direction can be determined by inversion of the GMF from radar backscatter measurements. The winds retrieved by the scatterometers have been shown to be highly accurate in areas with moderate wind speeds and no rain.

However, in a raining area the wind-induced scatterometer backscatter measurements are altered by rain. Rain has two effects on the scatterometer signal. First, in the atmosphere the scatterometer signal is attenuated and scattered by the raindrops. Second, raindrops striking the water alter the Bragg wave over the ocean, inducing additional surface backscatter. Since the GMF does not consider the attenuation and backscatter induced by rain, the wind estimates in raining areas can be degraded.

For a Ku-band scatterometer, rain is well-known to be a major factor that contaminates the wind retrieval process. Globally, rain is estimated to affect between 4% and 10% of the SeaWinds data [2] [3]. A significant amount of work has already been peformed to study the rain effects on Ku-band scatterometer measure-

ment [4] [5] [6]. Huddleston and Stiles developed a multi-dimensional histogram (MUDH) rain flagging technique for SeaWinds [2]. To improve rain contaminated wind estimates, Draper and Long developed a new wind/rain GMF accounting for rain using collocated Tropical Rain Measurement Mission (TRMM) Precipitation Radar (PR) and SeaWinds measurements. Using the wind/rain GMF, a new method has been developed to simultaneously estimate corrected wind estimates and integrated rain rate [7] [8].

Unlike Ku-band scatterometers, however, C-band scatterometer signals are traditionally considered to be immune to rain. The radar backscattering and attenuation by raindrops in the atmosphere is negligibly small in low to moderate rains. However, recent studies from laboratory experiments and from C-band SAR measurements reveal that the surface effects caused by rain may significantly modify the total backscatter of the C-band radar signal [7] [9]. Therefore, evaluating the various surface effects of rain is imperative for improving the accuracy of C-band wind estimation in raining areas.

Compared with scatterometers, SAR measurements are more vulnerable to rain events due to their high resolution. Rain cells can be observed in C-band SAR images. In the past, several investigations have analyzed the SAR signatures of rain cells over the ocean. Melshimer et al. [10] analyzed the SAR signatures of rain cells over the ocean using C- and X-band SAR measurements, showing that rain generally damps the surface backscatter at low incidence angles and enhances the backscatter at high incidence angles [11]. However, no quantitative analysis has been made for C-band SAR measurements.

1.2 Research Contributions

In this dissertation, rain effects on C-band scatterometer and SAR backscatter measurements are modeled. The wind/rain backscatter model is employed to develop a new wind retrieval method to improve rain-contaminated wind estimates and provide rain rate estimates. To achieve this goal, space-borne and ground-based precipitation radar rain measurements are collocated with scatterometer or SAR mea-

surements, providing rain observation comparison data. Numerical predicted wind fields from the European Centre for Medium Range Weather Forecasts (ECMWF) or Hurricane Research Division (HRD) at the National Oceanic and Atmospheric Administration (NOAA) are used in this study as the true near-ocean surface winds. A low-order wind/rain backscatter model for multiple incidence angles is developed and validated. The wind/rain backscatter model is shown to be accurate enough to represent the rain-contaminated radar signal. Based on the wind/rain backscatter model, a C-band simultaneous wind/rain retrieval (SWRR) method is developed for incidence angles above 40°. The SWRR can significantly improve wind velocity estimates and estimate rain rate with surprisingly high accuracy in moderate to heavy rains. In addition, a recalibration model is developed to recalibrate RADARSAT ScanSAR data, and wind retrieval is performed using the recalibrated data. The recalibration model improves the wind speed estimates in hurricanes. Complicated rain effects on C-band SAR images of hurricane Katrina are quantitatively analyzed and studied.

Valuable contributions are made by this dissertation in modeling rain effects on C-band scatterometer and SAR signals over the ocean and improving wind/rain retrieval from C-band scatterometer and SAR data. These contributions are discussed in the following paragraphs.

First, by using co-located TRMM PR, ESCAT on ERS, and ECMWF data, we develop and evaluate a simple low-order wind/rain backscatter model which has inputs of surface rain rate, radar incidence angle, wind speed, wind direction, and azimuth angle. By applying the model to the co-located data set, we demonstrate that the wind/rain backscatter model is accurate enough for describing the total backscatter in raining areas with relatively low variance. We also show that the rain surface perturbation is a dominating factor of the rain-induced backscatter. Using three distinct regimes, we identify under what conditions wind and rain can be retrieved from the measurements. In regime 1 where rain dominates, only rain information may be retrieved from the measurements. In regime 3 where wind dominates, only wind information can be retrieved. In regime 2 where rain and wind are comparable, wind

and rain information may be simultaneously retrieved from the measurements. In regime 1 and regime 2, wind-only retrieval methods are inadequate for retrieving the correct wind information. Therefore, the rain model should be incorporated into the retrieval algorithm. For incidence angle bins 40° to 44°, 44° to 49°, 49° to 53°, and 53° to 57°, about 0.9%, 1.3%, 1.74%, and 1.67% of all the co-located ESCAT measurements are affected by rain (falling in regime 1 or 2). We also show that rain has more impact on C-band measurements at higher incidence angles. This study is published in the *IEEE Transactions on Geoscience and Remote Sensing* [11]. Although the same underlying phenomenological backscatter model is used in both Ku-band and C-band rain model, the two frequencies are radically different. For Ku-band, rain atmospheric attenuation and atmospheric back-scattering are dominant while they are insignificant for C-band rain. Rain surface perturbation dominates the total rain-induced back-scatter at C-band, which makes the behavior of C-band model fundamentally different from the Ku-band rain model. The C-band rain model provides an accurate estimate of rain surface perturbation whereas the Ku-band model cannot. Furthermore, rain surface effects on C-band signal are much more complicated than Ku-band. For a C-band signal at low incidence angles the total effect of rain on surface wave spectrum is damping while rain enhances the total surface backscatter at high incidence angle. At moderate incidence angle, the total rain effect can be damping and enhancing, varying with rain type, drop size distribution, wind speed and other parameters. The dissertation analyzes the behavior of rain surface effects for C-band at various incidence angles and develops a multi-incidence-angle rain back-scatter model. The dissertation also reveals for the first time that rain can dominate the C-band total signal which was thought negligible before.

The next contribution of the research is developing a new simultaneous wind/rain retrieval method for C-band scatterometers. Using collocated TRMM PR, ESCAT on ERS-1/2, and ECMWF data, rain effects on ESCAT wind-only retrieval are evaluated and analyzed. Wind speed retrieved by wind-only retrieval is biased high due to the rain-induced backscatter. Rain contamination causes the wind direction estimates to be biased toward the along-track directions under heavy rain conditions,

no matter what the true wind direction. Rain effects on the wind-only retrieval vary with incidence angles. The higher the incidence angle, the more significant the rain impact is on the wind-only retrieval. To compensate for rain-induced backscatter, we develop a simultaneous wind/rain retrieval method for a C-band scatterometer for incidence angle $> 40^\circ$ based on a wind/rain backscatter model. Through simulation and validation with collocated ESCAT, TRMM PR, and ECMWF data, we find that SWRR can significantly improve wind speed and wind direction estimates in regimes 1 and 2 where rain and wind-induced backscatter are on the same order or rain dominates the total backscatter. In addition, SWRR can retrieve rain rate from ESCAT measurements. The rain estimates have relatively high accuracy in regimes 1 and 2. In regime 3 where the wind-induced backscatter dominates the total backscatter, the accuracy of SWRR-retrieved rain rates is degraded and spurious rain rates may be derived. SWRR does not perform well when the wind direction aligns with the along-track direction. In regime 3, the performance of SWRR is close to that of wind-only retrieval, though it is somewhat noisier due to introduction of a new parameter (the rain) to the retrieval. Therefore, SWRR wind/rain should only be used when the rain ratio τ is over a specific threshold. This work has been accepted for publication in the *IEEE Transactions on Geoscience and Remote Sensing*. Although the big idea is similar to Draper's Ku-band SWRR, the C-band SWRR is totally reformulated due to different behavior of the C-band rain model, instrument geometry, and noise model. As a result, the behavior of the two methods are quite different. Ku-band SWRR retrieves rain with relatively high accuracy, while Ku-band SWRR does not significantly improve the rain-contaminated wind vectors. On the other hand, C-band SWRR significantly improves the rain-contaminated wind speed and wind direction, while the rain estimates are relatively less accurate. Moreover, the dissertation systematically evaluates the effect of rain on the conventional wind-only retrieval and analyzes the reason causing these effects, which has never been done before.

RADARSAT-1 ScanSAR SWA images of Hurricane Katrina are used to retrieve surface wind vectors over the ocean. Collocated H*wind wind directions are used as the wind direction estimate. The wind speed is derived from σ° by inversion

of a C-band HH-polarization Geophysical Model Function (GMF), which is derived from the C-band VV-polarization GMF, CMOD5, using a polarization ratio model. Because existing polarization models do not fit the ScanSAR SWA data well, a new recalibration model is proposed to "recalibrate" the ScanSAR SWA images. The coefficients of the recalibration model are "tuned" using collocated H*wind surface wind fields. To validate the SAR-retrieved wind speed, the mean and the RMS difference between SAR-retrieved and H*wind wind speed estimates are calculated. The mean of difference is negligibly small and the RMS difference is below 4 m/s. Except for the influence of rain, the largest errors occur at high wind speed (over 25 m/s), which is due to the saturation of the GMF. While wind speed estimates over 25 m/s are noisy, no obvious bias is found, suggesting that the wind retrieval algorithm can work under hurricane conditions. Using the "recalibrated" ScanSAR SWA measurements, collocated ground-based Doppler weather radar (NEXRAD) measurements and collocated H*wind wind fields, the complicated rain effects on the ScanSAR SWA measurements are studied. Rain effects on ScanSAR SWA measurements include atmospheric effects (attenuation and backscattering) and surface effects. Rain surface effects on C-band SAR measurements can dominate the surface backscatter in moderate to heavy rains. For C-band, the rain surface effect varies with incidence angle. Using a simple wind/rain backscatter model and the collocated data set, we quantitatively analyze different rain effects on the ScanSAR measurements for three different incidence angle ranges and estimate the model coefficients. Compared with scatterometer-derived model, the rain-induced backscatter observed by the ScanSAR measurements at incidence angles $44^\circ - 45.7^\circ$ is consistent with the scatterometer-derived model, considering the polarization difference between HH and VV polarizations. While only three typical rain cells are considered in this dissertation, more rain cells on the ScanSAR SWA images can be analyzed by the same approach, and a more accurate model can be developed. This work is soon to be submitted to the *IEEE Transactions on Geoscience and Remote Sensing*. High resolution SAR rain modeling is a brand-new idea which is important for accurate modeling the complicated C-band surface effects of rain. As mentioned above, rain surface effects on C-band signal include damping

and enhancing. The high resolution of SAR provides a good opportunity to model different rain effects on C-band signal separately. It is the first time to quantitatively model these different effects using collocated SAR measurements and weather radar data. The results is consistent with the scatterometer-derived model. The dissertation also proposes a new method for re-calibrating SAR measurements in hurricane, which significantly improves the SAR wind retrieval in hurricane.

1.3 Outline of the Dissertation

This dissertation provides a study of modeling the rain effect on C-band scatterometer and SAR measurements, developing simultaneous wind/rain retrieval methods for a C-band scatterometer, and wind retrieval using SAR data in hurricanes. A brief outline of each chapter is noted below.

Chapter 2 provides a general background into wind scatterometry and SAR wind retrieval. An overview of the sensors including, ESCAT on ERS satellite and RADAR-SAT ScanSAR, are presented. Data processing of NEXRAD measurements is briefly discussed.

Chapter 3 evaluates the rain effects on ESCAT measurements and develops a C-band wind/rain backscatter model. The accuracy of the model is validated with collocated data sets. Three distinct regimes are defined to represent the wind/rain retrieval performance.

Chapter 4 evaluates the rain-induced errors on ESCAT conventional wind retrieval. A simultaneous wind/rain retrieval method is developed using the wind/rain backscatter model in Chapter 3. The performance of the simultaneous wind/rain retrieval method is evaluated using simulation and collocated data sets.

Chapter 5 develops a recalibration method for ScanSAR SWA wind retrieval and models the rain effects on ScanSAR data at various incidence angles. Several rain cells are analyzed in detail.

Conclusions are reached in Chapter 6 and future research is discussed.

Chapter 2

Background

In order to help the readers to understand the contributions made by this dissertation, this chapter reviews some fundamentals of wind scatterometry and principles of weather radar. This is accomplished by first describing the scatterometer instrument and the Geophysical Model Function (GMF) relating a measurement of normalized radar cross section, σ° to wind speed and direction over the ocean. Then, a statistical model of the backscatter measurements and wind retrieval method is presented. Finally, Doppler weather radar, the TRMM PR radar and rain estimation are reviewed.

2.1 Wind Scatterometry and Scatterometer

Wind scatterometry is a technique used to estimate near surface wind over the ocean by radar. A scatterometer is an active instrument designed to measure the backscatter of the ocean surface, as shown in Fig. 2.1. The scatterometer transmits electromagnetic pulses to the ocean surface and measures the energy scattered off the target. The normalized radar cross section, σ°, is calculated from the return power using the radar equation [12]

$$\sigma^\circ = \frac{(4\pi)^3 R^4}{P_t G^2 \lambda^2 A} P_r \tag{2.1}$$

where R is the distance from the scatterometer to the ocean surface, P_t is the power transmitted, G is the gain of the transmitting antenna, λ is the wavelength of the electromagnetic wave, A is the effective illuminated area, and P_r is the returned power. Scatterometer measurements are acquired at moderate to high incidence an-

gles, between 20 and 60 degrees. At these incidence angles, the main backscattering mechanism of the ocean's surface is Bragg resonance from capillary and short gravity waves, known as Bragg waves. Bragg resonance occurs when the returned signals backscattered from the ocean waves are added in phase. The condition for Bragg resonance is written in the form [13]

$$\frac{2L}{\lambda}\sin\theta = n, \quad n = 0, 1, 2, ... \tag{2.2}$$

where L is the water wavelength, λ is the radar wavelength, and θ is the radar incidence angle. Although the resonant power received is insignificant for radars with a small footprint, the Bragg resonance effect dominates the returned signal for space-borne scatterometers with a footprint measured in thousands of square meters or more. The Bragg-induced backscatter is related to the amplitude and orientation of the small Bragg waves.

For fair weather conditions (average sea state and absence of rain), Bragg waves on the ocean surface are mainly induced by wind. The wind transfers momentum into the ocean by forming and sustaining these small Bragg waves. The transfer of momentum from the wind to the ocean is via the wind stress, which is drag force per unit area. Under neutral stability conditions, the near-surface wind speed is related to the wind stress and the wind stress is a function of the amplitude of capillary waves. The Bragg-induced backscatter can be modeled as a function of the vector neutral stability wind. Several studies have been made to develop the function relating scatterometer measurement to vector wind. These studies have revealed the difficulties in developing a theoretical function to relate σ° with wind speed and direction. Instead, an empirical Geophysical Model Function (GMF) is used to represent the relationship between wind and σ°. The GMF may be expressed as

$$\sigma^\circ = \mathcal{M}(U, \phi, \theta, f, p) \tag{2.3}$$

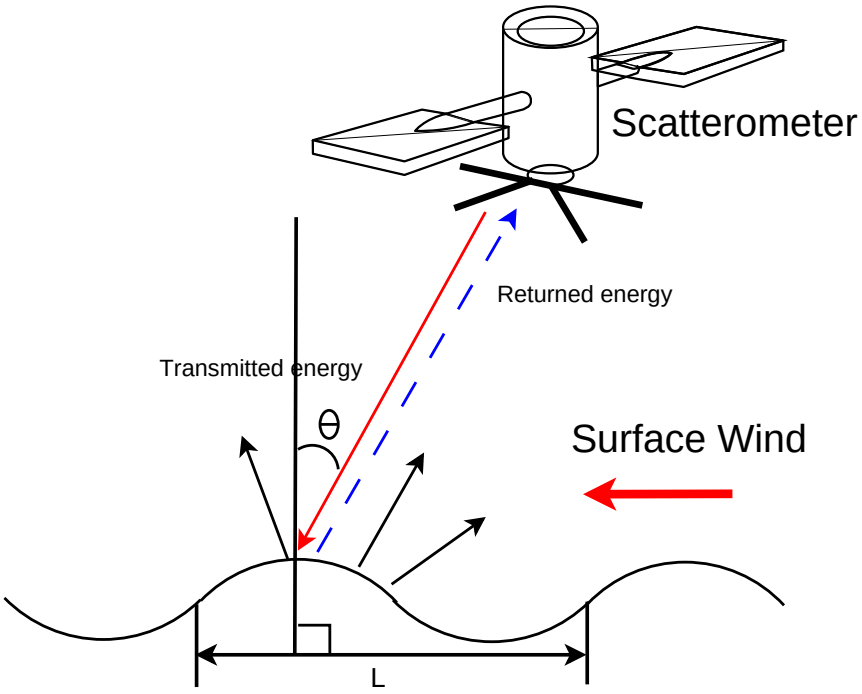

Figure 2.1: Demonstration of scatterometer operation over the ocean surface. Ocean waves are generated by surface wind.

where U is the wind speed, ϕ is the relative azimuth angle between the wind direction and the radar azimuth angle, θ is the radar incidence angle, f is the frequency of the radar, and p is the electromagnetic polarization of the transmitted signal. The frequency and polarization are usually fixed for a particular instrument. Therefore, the GMF is often expressed as

$$\sigma^\circ = \mathcal{M}(U, \phi, \theta). \tag{2.4}$$

Two approaches are often used to represent the GMF. One approach uses a multi-dimensional table to store the empirically-derived data points and interpolates intermediate values. This approach is implemented in deriving the GMF of the Ku-band scatterometer, SeaWinds on QuikSCAT and ADEOS II. The other approach uses a functional form to represent the GMF, such as CMOD5 for the C-band scatterometer ESCAT on the ERS 1/2 satellites. The second approach is used in

this dissertation. The GMF only considers the wind influence on the backscatter. However, other factors including sea temperature, salinity, long gravity waves, and especially rain also affect the relationship.

2.1.1 ESCAT Scatterometer and CMOD5

The scatterometer mode of the active microwave instrument (termed ESCAT) operated on the European Remote Sensing (ERS) satellites launched by the European Space Agency in 1991 (ERS-1) and 1995 (ERS-2). ESCAT is a fan-beam scatterometer operating at 5.3 GHz (C-band) VV-polarization. The geometry of ESCAT is shown in Fig. 2.2. ESCAT processing co-registers the backscatter measurements onto a rectangular grid of wind vector cells (WVCs). While ESCAT measurements are sampled at 25 km × 25 km, the effective resolution is 50 km × 50 km. With a 500 km swath, ESCAT has 19 WVCs along the cross-track direction. Ten of these WVCs correspond to center points of 50 km × 50 km cells spanning the swath. The other 9 WVCs are placed between these ten WVCS, generating 19 WVCs spaced on 25 km centers. At each WVC, σ° measurements of the fore, mid, and aft antenna beam are provided along with the geometric parameters and noise parameters. To

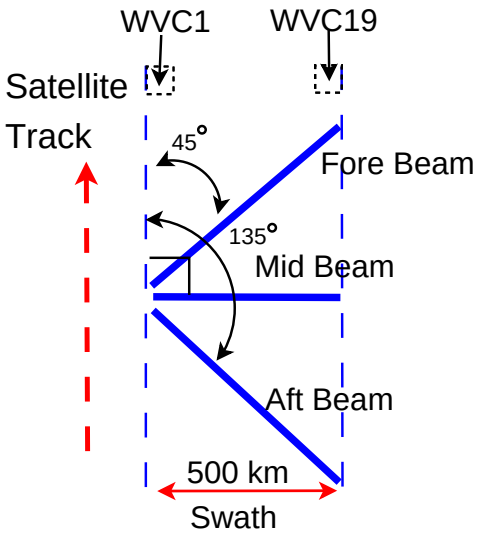

Figure 2.2: Measurement geometry for ESCAT on ERS-1/2

enable sufficient azimuthal diversity, ESCAT has three side-looking antennas with the beams pointed at angles of 45°, 90°, and 135° from the satellite ground track on the starboard side. The incidence angles of each antenna vary across the swath, between 22° and 56° for the fore and aft antenna, and between 18.2° and 42° for the mid antenna [14]. Figure 2.3 shows the typical incidence angles of the three beams. ESCAT transmits approximately 5 kW peak power, resulting a high signal-to-noise ratio.

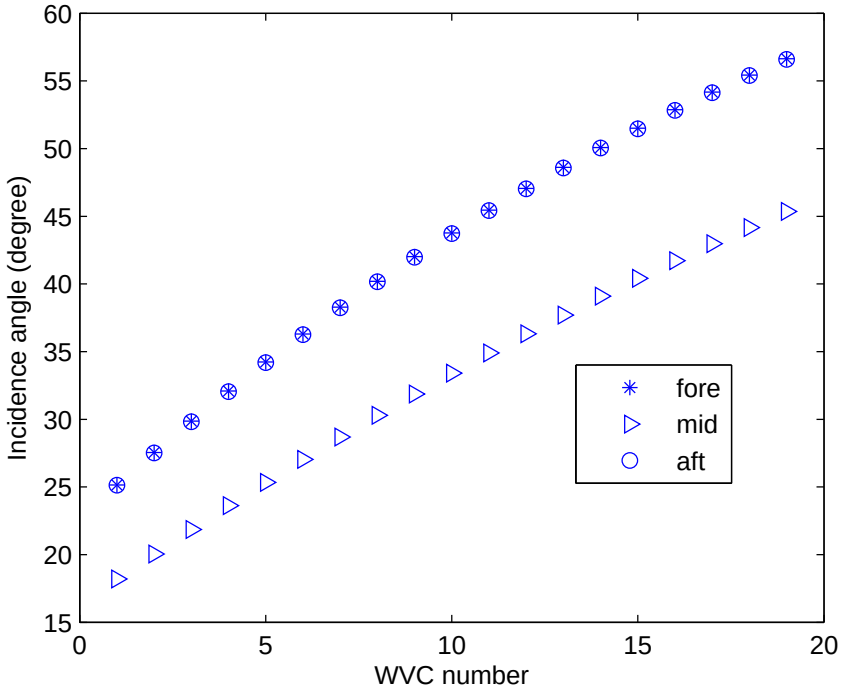

Figure 2.3: Typical incidence angles of the fore, mid, and aft beams of ESCAT on ERS-1/2. Note that the fore and aft antennas have the same incidence configuration.

As mentioned, the GMF developed for ESCAT is based on a functional form to represent the relationship between σ° and vector wind. The latest GMF for C-band is called CMOD5. The functional form of the CMOD5 model is [15]

$$\sigma^\circ = B0(1 + B1\cos\chi + B2\cos 2\chi)^{1.6} \tag{2.5}$$

where $B0$, $B1$ and $B2$ are functions of wind speed and incidence angle, or alternatively, $(\theta - 40)/25$. The coefficients of CMOD5 are estimated using ESCAT measurements and numerical predicted winds from the European Centre for Medium-Range Weather Forecasts (ECMWF).

Figure 2.4 shows plots of the CMOD5 σ° versus relative azimuth angle, χ, for several values of wind speed and incidence angle. The $cos(2\chi)$ dependence on χ can be found in all the plots. There is also a general trend of decreasing σ° for increasing incidence angle. Figure 2.5 shows plots of the CMOD5 σ° versus speed with $\chi = 45$ degrees and $\theta = 20$, 30, and 40 degrees. σ° increases as wind speed increases at low to moderate wind speeds. For wind speeds over 25 m/s, σ° saturates. The relationship between σ° and wind speed becomes flat. Therefore, wind retrieval of high winds is seriously degraded for a C-band scatterometer.

2.2 Wind Retrieval

Once suitable σ° measurements are collected, they are used to estimate or "retrieve" the near-surface wind. The wind retrieval procedure involves inversion of the GMF given the measurements. As shown in Fig. 2.4, multiple wind speeds and directions can be mapped to the same value of σ°; hence a unique wind vector cannot be estimated from a single σ°. In order to estimate wind vector from scatterometer measurements, multiple measurements of σ° from various azimuth angles must be acquired. To visualize the wind retrieval procedure of ESCAT, the locus of wind velocities that give rise to a single σ° for fixed radar incidence and azimuth angles is plotted in Fig. 2.6(a) for three sets of radar angles representative of simulated data from the ESCAT scatterometer for WVC 19. These plots are generated by choosing a wind speed and direction and calculating the σ° values using CMOD5. For each set of radar incidence and azimuth angles, all the wind speeds and directions that induce the specific σ° are plotted as a single curve. As shown in Fig. 2.6(a), the three measurements without noise from the fore, mid, and aft beams have an intersection corresponding to the true wind velocity. Due to the upwind/downwind similarity, there is a near intersection point about 180° from the true wind direction. In the

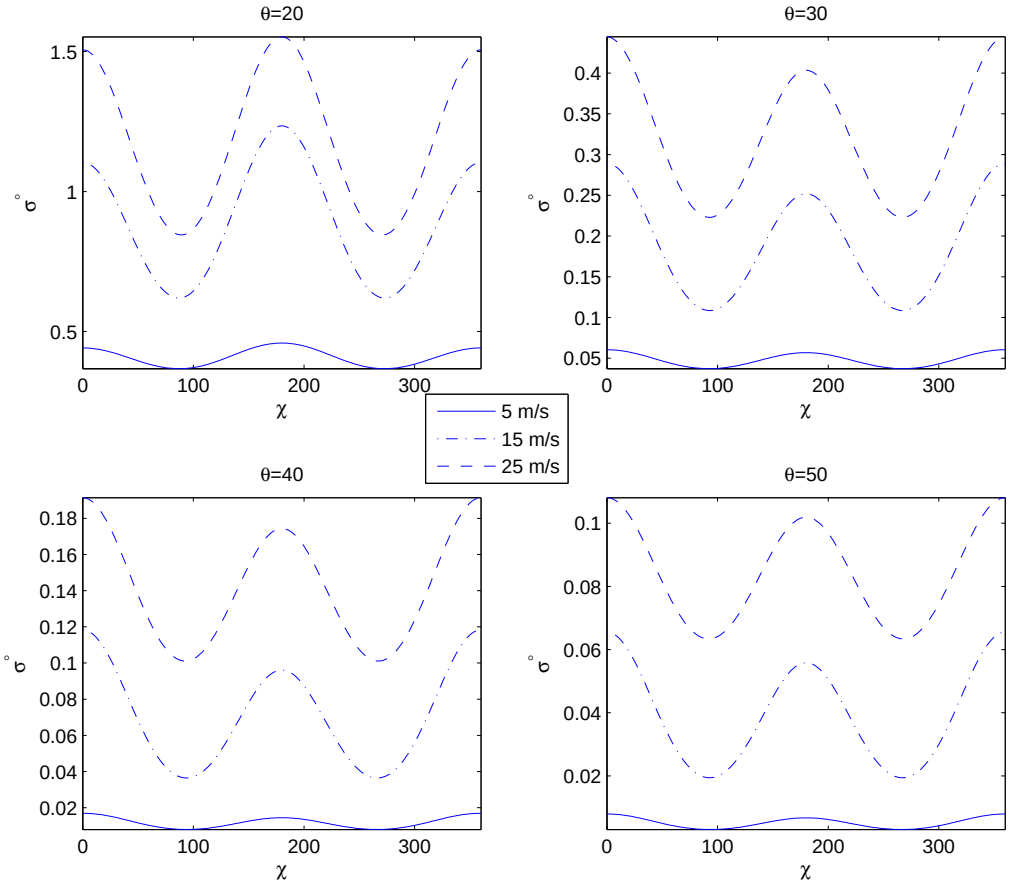

Figure 2.4: Plots of σ° versus relative azimuth angle, χ for various incidence angles and wind speeds. The incidence angles chosen are $\theta = 20^\circ$, 30°, 40°, and 50°. The wind speeds chosen are 5, 15, and 25 m/s.

presence of noise, as shown in Fig. 2.6(b), it is difficult to distinguish the 180° alias from the true wind velocity. Therefore, the wind retrieval process often results in several possible wind vector solutions, called ambiguities.

In general, the standard wind estimation procedure, known as point-wise wind retrieval, is based on minimization of an objective function derived from maximum likelihood estimation (MLE) techniques. The scatterometer measurement can be modeled as corrupted independent Gaussian noise. The variability of the scatterometer measurement is contributed by two sources. First, the GMF has uncertainties due to ignoring other factors affecting σ° beyond wind velocity. The true σ°, σ_t°, can

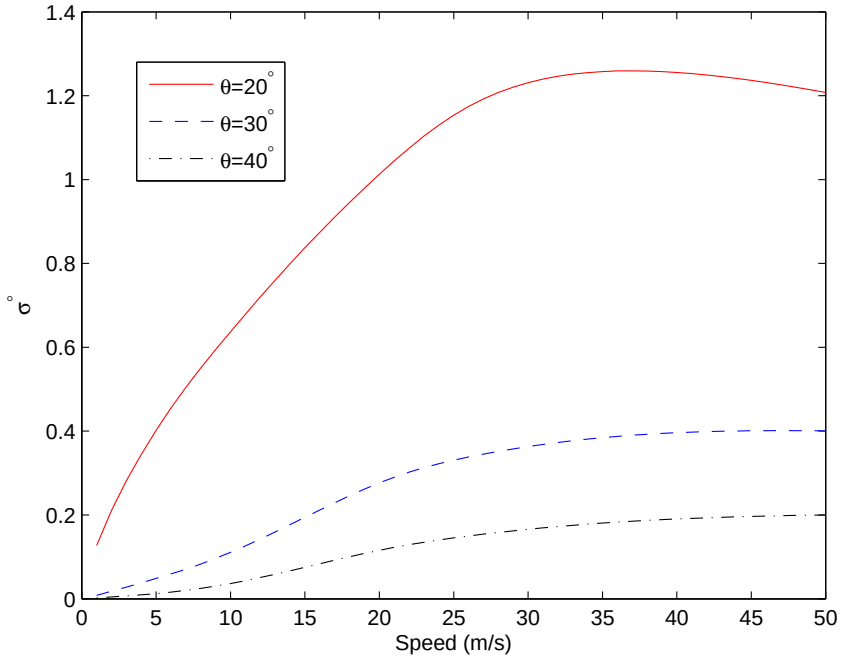

Figure 2.5: Plots of σ° versus wind speed for various incidence angles with $\chi = 40$ degrees. The incidence angles chosen are 20°, 30°, and 40°.

be modeled as a Gaussian random variable with mean equal to the GMF predicted σ°, σ_m°,

$$\sigma_t^\circ = \sigma_m^\circ(1 + K_{pm}v_1) \tag{2.6}$$

where v_1 is a standard Gaussian random variable and K_{pm} is the normalized standard deviation of the GMF. Second, σ_t° is corrupted by instrument noise and background noise. This source of uncertainty can be modeled by [16]

$$\sigma_{meas}^\circ = \sigma_t^\circ(1 + K_{pc}v_2) \tag{2.7}$$

where σ_{meas}° is the measured σ°, v_2 is a standard Gaussian random variable, and K_{pc} is the normalized standard deviation of the instrument and background noise.

With the above model, the scatterometer measurement, σ_{meas}°, is a Gaussian random variable with mean σ_m° and variance ς. The probability of the σ° measure-

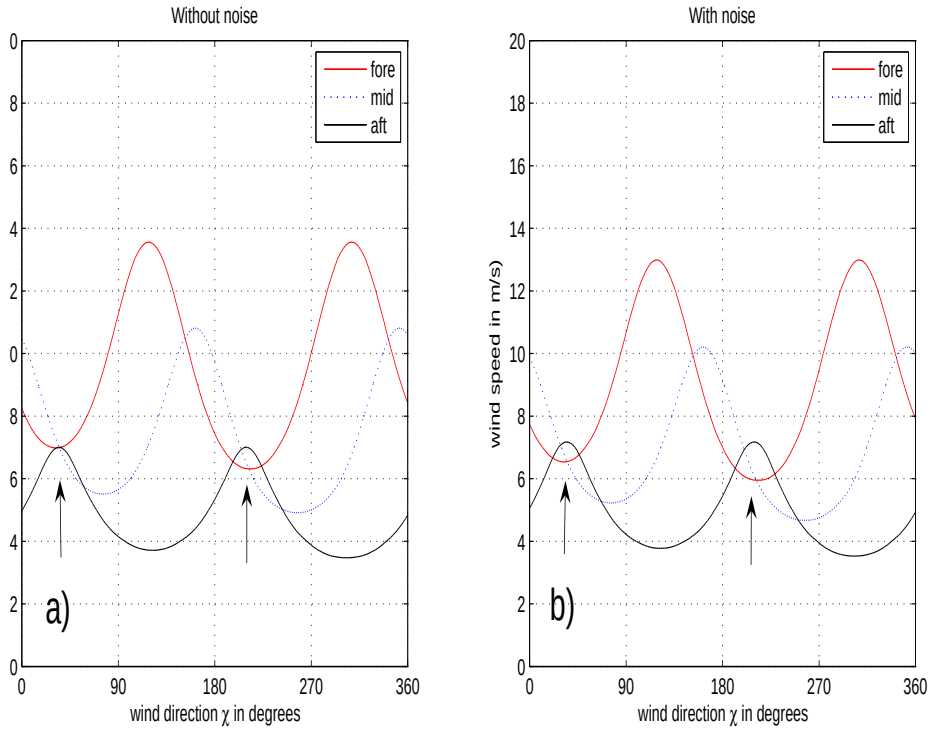

Figure 2.6: Visualization of the wind retrieval procedure for data in WVC 19 ($\theta_{fore/aft} \approx 56.6°$ and $\theta_{mid} \approx 45.4°$). The intersections of the three curves correspond to the true wind velocity and ambiguities called "aliases". The arrow in the plots point to the two major ambiguities. (a) The wind retrieval from measurements without noise. (b) Measurements with random noise. The true wind speed is 7 m/s and the true wind direction is 35°.

ments at a given point, $\hat{\sigma}^{\circ}_{meas}$, given the wind speed and direction, $p(\hat{\sigma}^{\circ}_{meas}|s,d)$, is

$$p(\hat{\sigma}^{\circ}_{meas}|s,d) = \prod_{i=1}^{K} \frac{1}{\sqrt{2\pi}\varsigma_i} \exp\left\{ -\frac{(\sigma^{\circ}_{meas(i)} - \mathcal{M}_i(s,d))^2}{2\varsigma_i^2} \right\} \tag{2.8}$$

where $K = 3$ for ESCAT and ς_i^2 is the measurement variance. Using the above noise model, the total variance of σ°_{meas} is given by

$$\varsigma^2(s,d) = (K_{pc}^2 + K_{pm}^2 + K_{pc}^2 K_{pm}^2)\mathcal{M}^2(s,d) \tag{2.9}$$

where K_{pc} has the form

$$K_{pc} = \sqrt{\alpha + \frac{\beta}{\sigma_t} + \frac{\gamma}{\sigma_t^2}}. \tag{2.10}$$

The α, β, and γ are coefficients depending on fading characteristics of the surface scatters and the signal to noise ratio (SNR) at the receiver [1] [17]. The K_{pc} of ESCAT measurement is calculated and stored with the σ° measurements in standard data products.

With the probability of the measurements given the wind, the objective function used in wind retrieval is formed by ignoring the $\frac{1}{\sqrt{2\pi}\varsigma_i}$ and taking the negative logarithm, yielding

$$\mathbf{MLE}(\hat{\sigma}^\circ_{meas}|s,d) = \sum_{i=1}^{3} \frac{\Big(\sigma^\circ_{meas(i)} - \mathcal{M}(s,d,\phi_i,\theta_i)\Big)^2}{\Big(\varsigma_i(s,d)\Big)^2}. \tag{2.11}$$

The wind retrieval procedure is to find the s and d that minimizes this objective function.

Due to the symmetry inherent in the GMF, minimization of the objective function results in 1 to 4 local minima (ambiguities), which represent possible wind vector solutions. The two primary ambiguities correspond to the two most likely solutions, typically differing by about 180° in direction. The occurrence and location of the other ambiguities often depend on the normalization [18]. A method proposed by Stoffelen and Anderson transforms the measurements to a z'-space of the form $z' = (\sigma^\circ)^{0.625}$ and results in a circular distribution that is ideal for inversion [18]. During wind retrieval procedure, the ambiguities are ordered by increasing objective function value and termed as the first or the second ambiguity and so forth. Although the first ambiguity is the most likely to be the correct solution, any of the ambiguities may be the closest estimate; hence an ambiguity removal algorithm is necessary to choose a unique wind vector field.

The ambiguity removal procedure uses median filtering and nudging techniques to choose the best solution. For ESCAT wind-only retrieval, a selection filter is implemented to iteratively select the ambiguity at each WVC, based on a weighted average of the differences from the surrounding WVCs. At each WVC, the selection filter is nudged by the ECMWF Model First Guess At Appropriate Time (FGAT) wind vectors.

2.3 NEXRAD Rain Estimation

NEXRAD is a ground-based weather radar that measures rainfall. NEXRAD measures radar reflectivity and Doppler shift by employing a rotating 8.5-m paraboloid antenna with a output power of 750 kW. NEXRAD radar operates at S-band (2.7-3.0 GHz). During storm events, NEXRAD uses an operational data collection mode known as Volume Coverage Pattern (VCP) 11. The VCP 11 is designed to sample severe and non-severe precipitation events. As shown in Fig. 2.7, the radar successively scans 360° in azimuth angle in 1° increments and from 0.5° to 6.2° in 0.95° increments in elevation angle. Additional circular scans at a 7.5°, 8.7°, 10.0°, 12.0°, 14.0°, 16.7°, and 19.5° elevation angle are performed. Since the beam-width of NEXRAD is about 0.95°, the first seven scans continuously cover the sampling space.

The raw data from NEXRAD is stored in Plan Position Indicator (PPI) mode as shown in Fig. 2.7. To compare NEXRAD measurements with other data, the raw data are converted to Constant Altitude Plan Position Indicator (CAPPI) model. Due to the refraction of atmosphere, the radar path or ray is not a straight line. The ray path is computed using "four-thirds earth radius model". The following equations relate the height h and distance s to radar range r and elevation angle θ_e [19]

$$h = \sqrt{r^2 + (k_e a)^2 + 2 r k_e a \sin\theta_e} - k_e a \tag{2.12}$$

and

$$s = k_e a \sin^{-1}\left(\frac{r\cos\theta_e}{k_e a + h}\right) \tag{2.13}$$

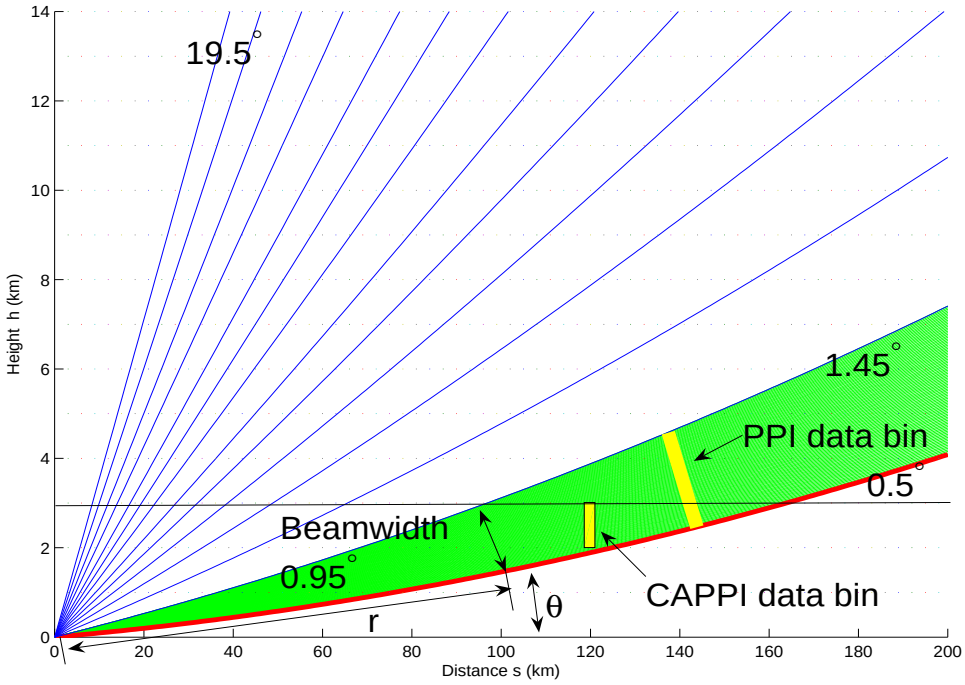

Figure 2.7: NEXRAD operation using VCP 11 and the "four-thirds earth radius model". The dark gray regions represent the cross-sectional are spanned by the radar's beam-width. The light gray area illustrate the difference between PPI bins and CAPPI bins.

where a is the radius of earth and $k_e = 4/3$. NEXRAD estimates reflectivity, Z, from reflected power measurements, P_r, using

$$Z = \frac{2^{10}(\ln 2)}{\pi^3 c} \frac{\lambda^2 r^2 P_r}{P_t \tau G^2 \theta^2 |K|^2} \tag{2.14}$$

where Z is the reflectivity, c is the speed of light, λ is the transmitted wavelength, P_t is the transmitted power, τ is the pulse duration in seconds, G is the antenna gain, θ is the 3dB antenna beam-width, r is the range to target, and K is the complex index of refraction for water or snow [12]. Using VCP 11, Z is estimated at 1 km intervals over the range of 1 to 460 km from the radar.

The reflectivity Z is related to rain rate R (mm/hr) with (Z-R) relationship,

$$Z = aR^b \quad \text{mm}^6/\text{m}^3 \tag{2.15}$$

where a and b are constants. The constants a and b depends on the drop-size distribution. For stratiform rain

$$Z = 200R^{1.6} \quad \text{mm}^6/\text{m}^3 \tag{2.16}$$

has proved to be quite accurate. For summer convective rain

$$Z = 300R^{1.4} \quad \text{mm}^6/\text{m}^3 \tag{2.17}$$

is optimum. Comparison between the two Z-R relationship is shown in Fig. 2.8. The difference between the two relationship is less than 25% for rain rate less than 30 mm/hr. Rain rate R can be estimated by inversion of Z-R relationship

$$R = (Z/a)^{-b} \quad \text{mm/hr.} \tag{2.18}$$

2.4 TRMM

The Tropical Rainfall Measuring Mission (TRMM) satellite was launched in 1997 and orbits at a low inclination angle of 35°, providing coverage of the tropics. The objectives of TRMM are to measure rainfall and energy exchange of tropical and subtropical regions of the earth. The TRMM Precipitation Radar (PR) instrument on the TRMM satellite is the first space-borne instrument designed to provide three-dimensional radar maps of storm structure. The TRMM PR has a horizontal resolution at the ground of about 4.5 km and a swath width of 220 km [20]. The TRMM PR antenna scans within 17° of the nadir. The latitudes of TRMM PR measurements are between ±36° [20].

TRMM PR radar data are archived as level 1 products. All geophysical products, including 3D rain rate maps, qualitative rain characteristics, and statistics of surface scattering cross sections are computed from the level 1 products. Level 2A25

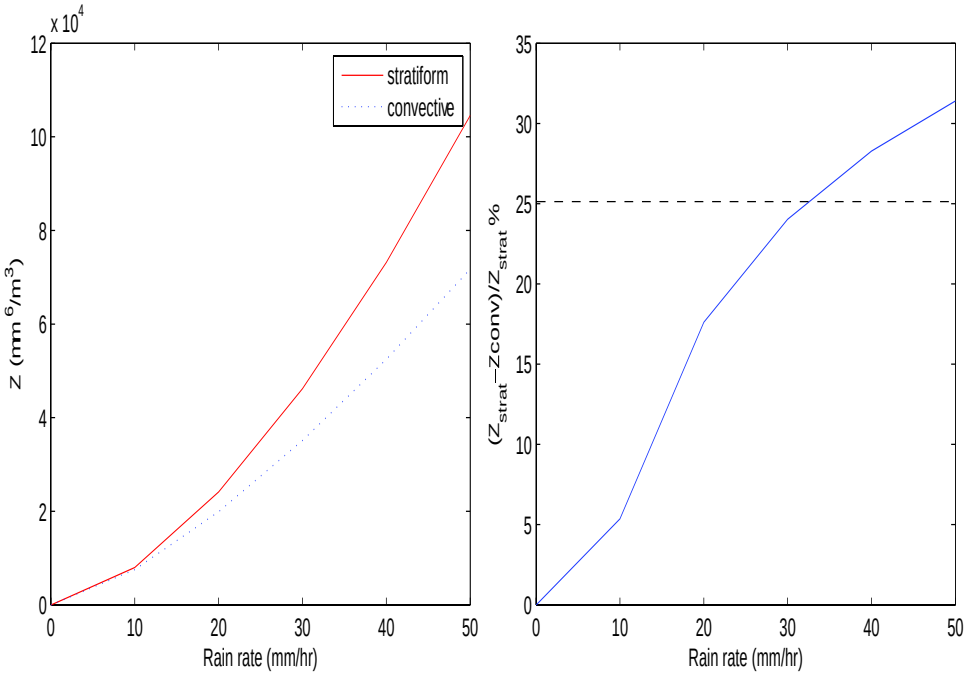

Figure 2.8: Comparison between Z-R relationship for stratiform rain and convective rain. (a) Z-R versus rain rate and (b) The normalized difference between Z-R versus rain rate for stratiform and convective case.

product providing 3D rain rate maps are used in the dissertation [21]. The geometry of the TRMM PR and ESCAT on ERS are shown in Figure 2.9.

As a summary, scatterometers provide high quality global-scale ocean surface winds for fair weather conditions. Unfortunately the wind estimates are degraded in raining areas. In the following chapters, I study the effect of rain on scatterometer and SAR wind retrieval using the rain measurements from space-borne or ground-based rain radars to develop a new method that improves the wind retrieval in raining areas.

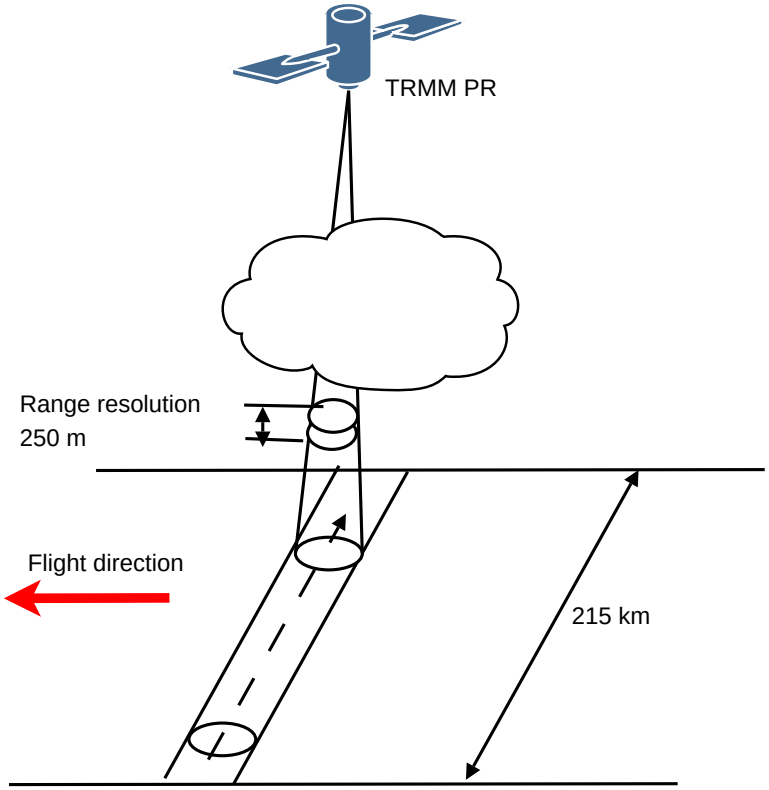

Figure 2.9: Schematic view of the measurement geometry of the TRMM PR.

Chapter 3

A C-band Wind/Rain Backscatter Model

The previous chapter shows that backscatter in non-raining and moderate wind speed areas is mainly from the wind-roughened ocean surface. In this chapter, rain effects on C-band scatterometer data is studied and a C-band wind/rain backscatter model is introduced. For a Ku-band scatterometer, rain is believed to a major factor in contaminating the wind retrieval process. Unlike Ku-band, the C-band scatterometer signal is traditionally considered rain transparent. It is reported that the radar backscattering by raindrops for the C-band signal is negligibly small and the attenuation exceeds 1 dB only when the rain rate is above 50 mm/hr [22] [23]. However, recent studies reveal that surface effects by rain may significantly modify the total backscatter of both Ku-band and C-band scatterometers [7] [24] [9], and hence influence the wind retrieval process. Therefore, evaluating the various surface effects of rain on ERS scatterometer measurements is necessary for improving the accuracy of ERS wind estimation in raining areas. Furthermore, under some conditions, it may be possible to retrieve rain rate information from the C-band scatterometer measurements.

In a raining area, the wind-induced scatterometer backscatter signature is altered by rain. Rain striking the water creates splash products including rings, stalks, and crowns from which the signal scatters [25]. The contribution of each of these splash products to the backscattering varies with incidence angle and polarization. At VV-polarization, rain-generated ring-waves are the dominant feature for radar backscattering at all incidence angles. At HH-polarization, with increasing incidence angles the radar backscatter from ring-waves decreases while the radar backscatter from non-propagating splash products increases [24]. Similar results are found in

experiments done with a VV-polarized Ku-band system [25]. Raindrops impinging on the sea surface also generate turbulence in the upper water layer which attenuate the short gravity wave spectrum [9] [26]. A study by Melsheimer et al. [9] shows that the modification of the sea surface roughness by impinging raindrops depends strongly on the wavelength of water waves: the net effect of the impinging raindrops on the sea surface is a decrease of the amplitude of those water waves which have wavelengths above 10 cm and an increase of the amplitude of those water waves which have wavelengths below 5 cm [9]. But the critical transition wavelength at which an increase of the amplitude of the water wave turns into decrease is not well defined. It depends on the rain rate, the drop size distribution, the wind speed and the temporal evolution of the rain event [9]. Thus, in the transition wavelength regime, raindrops impinging on sea surface may increase or decrease the amplitude of the Bragg waves. In addition to the modification of the sea surface roughness by the impact of raindrops, the sea surface roughness is also affected by the airflow associated with the rain event [9]. The scatterometer signal is additionally attenuated and scattered by the raindrops in the atmosphere.

To evaluate the effect of rain on C-band ESCAT σ° observations, we use a simple phenomenological backscatter model, similar to the one used in developing a Ku-band wind/rain backscatter model for SeaWinds [7]. To estimate the rain-induced parameters of the model, we use co-located Precipitation Radar (PR) data from the Tropical Rainfall Measuring Mission (TRMM) satellite. Each co-located region contains the overlapping swaths in which the time difference between the TRMM PR time tags and the ERS time tags is less than ± 15 minutes. Since co-located regions between ESCAT and TRMM PR are relatively rare, we processed 16 months of data from August 01, 1999 to December 31, 2000. About 82181 co-locations are found in this period. To improve the accuracy of the estimated model parameters, we use only the co-located regions where the overlapping PR swath contains more than 2.5% of the measurements flagged as rain-certain in the TRMM 2A25 files.

Before illustrating the derivation of the model, we describe the data in Section 3.1. In Section 3.2, we define the wind/rain model and estimate the the model

coefficients. In Section 3.3, we validate the wind/rain backscatter model and estimate the influence of rain using regimes. Conclusions are reached in the Section 3.4. We illustrate that the wind/rain backscatter model is accurate enough for describing the total backscatter in raining areas with relatively low variance. We also show that the rain surface perturbation is a dominating factor of the rain-induced backscatter. Using three distinct regimes, we show under what conditions wind, rain, and both wind and rain can be retrieved from the measurements. We find that the effect of rain has a more significant impact on the measurements at high incidence angles than at low incidence angles.

3.1 Data

To derive the wind/rain backscatter model, we use co-located ESCAT backscatter, rain data from TRMM PR, and predicted wind fields from European Center for Medium-Range Weather Forecasts (ECMWF) [27]. We describe these data in this section.

As mentioned in Chapter 1, ESCAT on the ERS-1 and ERS-2 satellites is designed to measure ocean winds. The C-band scatterometer collects σ° measurements at 5.3 GHz VV-polarization. After collecting backscatter measurements, wind retrieval is performed by inverting the GMF, based on multiple σ° measurements at different azimuth angles and incidence angles for each wind vector cell (WVC). To allow sufficient azimuthal diversity, ERS has three side-looking antenna with the beams pointed at angles of 45°, 90°, and 135° from the satellite ground track on the starboard side. The incidence angles of each antenna vary across the swath, between 22° and 56° for the fore and aft antenna, and between 18.2° and 42° for the mid antenna [14]. The swath width of ESCAT is 500 km. The effective resolution of ESCAT is 50×50 km [14]. The σ° measurements have a Hamming window spatial response function. Because measurements with different incidence angles may have different characteristics, it is necessary to analyze them separately.

The numerical weather prediction wind fields from ECMWF provides surface wind estimates without consideration of rain. We use the ECMWF predicted winds to

estimate the wind-induced σ°. The ECMWF winds are trilinearly interpolated (both in space and time) from a $1^\circ \times 1^\circ$ latitude-longitude grid with a temporal resolution of 6 hours to the ESCAT data times and locations. ECMWF predicted σ°, computed using the improved geophysical model function CMOD5, are on average 0.08 dB lower than ESCAT measured σ° [15]. This introduces a region-dependent bias ϵ, which is estimated in Section 3.2.

TRMM PR data is used to estimate rain. The TRMM satellite was launched in 1997 and orbits at a low inclination angle of 35°, providing coverage of the tropics. The TRMM PR instrument on the TRMM satellite has a horizontal resolution at the ground of about 4 km and a swath width of 220 km [20]. The TRMM PR antenna scans within 17° of the nadir. The latitudes of TRMM PR measurements are between $\pm 36^\circ$ [20]. Because both the viewing geometry and the operating frequency (13.8 GHz for TRMM PR versus 5.3 GHz for ESCAT) of TRMM PR and ESCAT are not the same, the effects of rain on the backscatter (atmospheric attenuation and backscattering) are different. We estimate the atmospheric effects of rain on the ESCAT signal by using the three dimensional rain rate estimation from TRMM PR level 2A25 product [21]. The co-location geometry of the TRMM PR and ESCAT on ERS are shown in Figure 3.1. Due to the different orbit geometry and the narrow swath of ESCAT and TRMM PR, the co-locations are relatively rare.

3.2 Model Measured σ° in Rain and Wind

Rain drops impinging on the sea surface, airflow associated with rain roughening the sea surface, and rain-generated turbulence affect the surface backscattering of the scatterometer signal. Since we only care about the bulk effect of rain on the Bragg wave field, we combine all these contributions together into a single rain surface perturbation backscatter term, σ_{surf}. Assuming that σ_{surf} is additive with the wind-induced surface backscatter, we use a simple additive model for the total backscatter, following the Ku-band wind/rain backscatter model of [7]. The rain-modified mea-

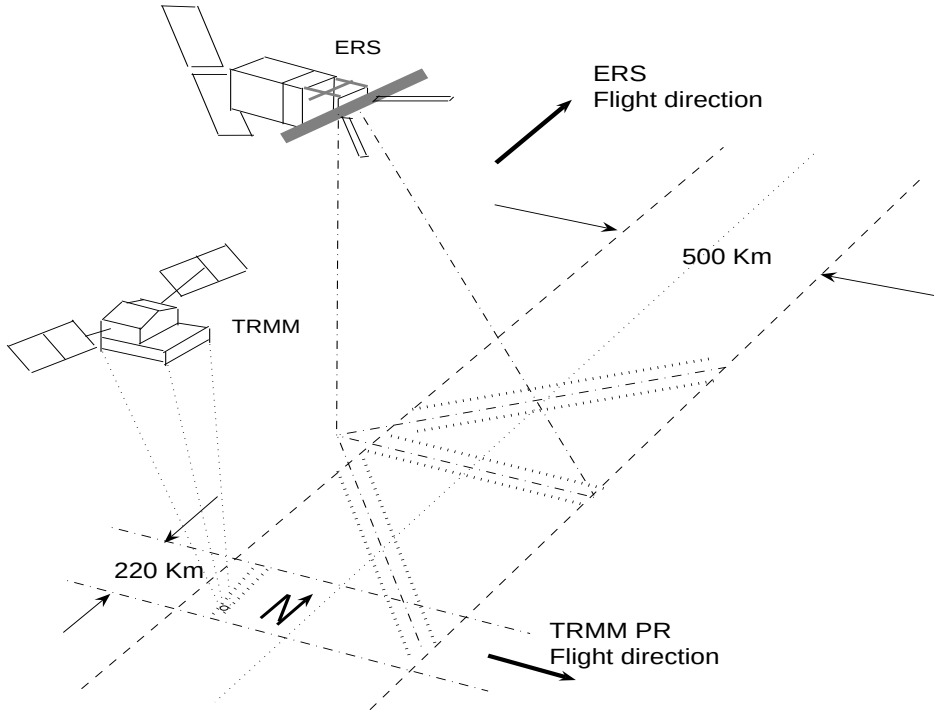

Figure 3.1: Swath geometry of the TRMM PR and ESCAT on ERS instruments in colocating regions.

sured backscatter, σ_m, is

$$\sigma_m = (\sigma_{wind} + \sigma_{surf})\alpha_{atm} + \sigma_{atm} \tag{3.1}$$

where σ_m is the ESCAT-measured σ°, σ_{wind} is the wind-induced surface backscatter predicted by the ECMWF, σ_{surf} is the rain-induced surface perturbation backscatter, α_{atm} is the two-way rain-induced atmospheric attenuation, and σ_{atm} is rain-induced atmospheric backscatter.

The wind/rain backscatter model can be further simplified by summing the attenuated surface perturbation and the atmospheric scattering terms, creating a single effective rain backscatter parameter, σ_{eff}. The combined rain effect model is [7]

$$\sigma_m = \sigma_{wind}\alpha_{atm} + \sigma_{eff} \tag{3.2}$$

where

$$\sigma_{eff} = \sigma_{surf}\alpha_{atm} + \sigma_{atm}. \tag{3.3}$$

The rain-induced backscatter and attenuation are related to the rain intensity, r, and incidence angle, θ. The wind-induced backscatter is function of wind speed, s, wind direction, d, azimuth angle, χ, and incidence angle. Thus, the total backscatter, σ_m, can be expressed as a function F of these parameters,

$$\sigma_m = F(r, s, d, \chi, \theta). \tag{3.4}$$

There are two metrics for rain intensity: integrated rain rate (km mm/hr) and surface rain rate (mm/hr). Because the rain is not uniformly distributed along the slant path, these two metrics are non-linearly related. In the Ku-band wind/rain backscatter model, integrated rain rate is used as the metric [7] since contributions of the rain-induced surface backscatter and the rain-induced atmospheric backscatter are comparable. For the C-band model, the rain-induced surface backscatter dominates the rain-generated backscatter, and thus surface rain rate (mm/hr) is selected as the rain intensity metric. Also, since the beam of TRMM PR and ESCAT only overlap on the ocean surface, using surface rain rate is expected to introduce smaller errors than using integrated rain rate.

Because the spatial response function gain is not uniform over the ESCAT footprint, the contribution of rainfall varies with the location in the footprint. Thus, the ESCAT observed surface rain is a weighted-average of the surface rain. We define the weighted-averaging function as

$$P_{ESCAT} = \frac{\sum_{i=1}^{N} G(i) P_{PR}(i)}{\sum_{i=1}^{N} G(i)} \tag{3.5}$$

where P_{ESCAT} is the ESCAT observed parameter after the weighted averaging (such as ESCAT observed surface rain rate $R_{surf(ant)}$), $G(i)$ is the ESCAT spatial response

function gain at the ith PR measurement, N is the number of PR data points within ESCAT 3-dB antenna pattern contour, and $P_{PR}(i)$ is the parameter to be averaged, corresponding to the ith PR measurements (such as PR measured surface rain rate $R_{surf(PR)}(i)$). To estimate ESCAT observed surface rain rate $R_{surf(ant)}$, TRMM PR level 2A25 surface rain rate $R_{surf(PR)}$ is averaged over the ESCAT footprint using Equation (3.5). Due to non-uniform beam filling (NUBF) and the ESCAT non-uniform spatial response gain pattern, there is a difference between the ESCAT gain-weighted average surface rain rate and the uniform-weighted average rain rate. This beam-filling variability is also noted in the Ku-band scatterometer rain/wind backscatter model [7]. We estimate the NUBF effect on surface rain rate by computing the normalized error $\epsilon = (R_{surf(ant)} - R_{surf(uni)})/R_{surf(uni)}$ between the antenna-weighted average rain rate $R_{surf(ant)}$ and the uniform-weighted average rain rate $R_{surf(uni)}$ for each ESCAT measurement. Although the PR-measured rain also contains beam-filling error, we ignore its effect for simplicity. The uniform-weighed average surface rain rate $R_{surf(uni)}$ is computed by averaging the PR measured surface rain rates $R_{surf(PR)}$ within the 3-dB ESCAT footprint with uniform weights $G(i) = \frac{1}{N}$. We calculate the statistics of ϵ with significant rain rates (≥ 0.8 mm/hr) for the entire co-located data set. The mean of ϵ is 0.002, which is negligible, while the standard deviation is 0.152. This suggests that the NUBF does not introduce bias to the rain rate estimates, but it increases variability of the estimates. A histogram of the antenna-weighted average surface rain rates $R_{surf(ant)}$ of the co-located data set is shown in Figure 3.2. It is noted that the maximum of $R_{surf(ant)}$ is about 40 mm/hr, while the mean is about 0.4 mm/hr.

3.2.1 Estimating Model Parameters

To estimate the surface perturbation backscatter σ_{surf}, we need to know the rain-induced atmospheric backscatter σ_{atm}, the attenuation α_{atm}, and the wind-induced surface backscatter σ_{wind}. We estimate σ_{atm} and α_{atm} by using co-located TRMM PR level 2A25 three dimensional rain rate.

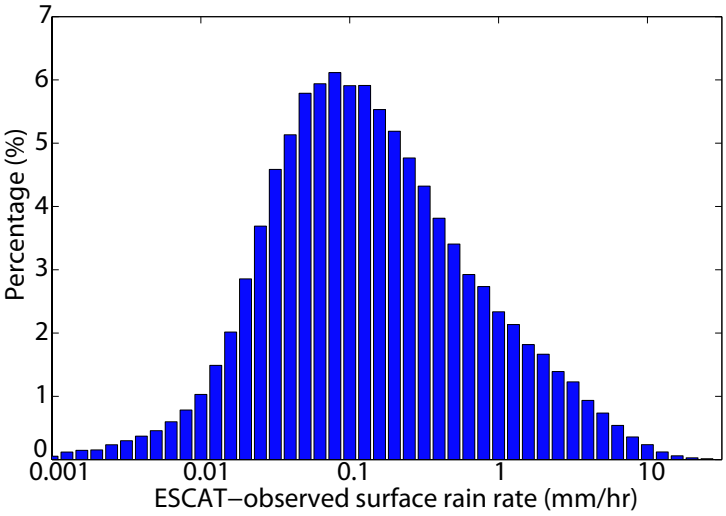

Figure 3.2: Histogram of ESCAT response-function-weighted surface rain rate $R_{surf(ant)}$ derived from TRMM PR observations of the co-located data set, consisting of 82181 collocations with rain-certainty exceeding 2.5% over August 01, 1999 to December 31, 2000.

To calculate the two-way atmospheric attenuation α_{atm}, we first estimate the atmospheric attenuation factor k_a at the ESCAT wavelength (5.7 cm) using the $k_a - R$ relation, which relates k_a and the rain rate (mm/hr) [28],

$$k_a = 2KR \quad \text{dB km}^{-1}/\text{mm hr}^{-1} \tag{3.6}$$

where $K = 0.0033$ for 5.7 cm wavelength and R is TRMM PR level 2A25 three dimensional rain rate in mm/hr. Following the method in [7], the path integrated attenuation (PIA) in dB at the ESCAT wavelength for each TRMM PR measurement $PIA_{PR}(i)$ is computed by integrating k_a through the PR antenna beam to the lowest no-surface-clutter range. The two-way atmospheric attenuation factor seen by ESCAT at the ith TRMM PR measurement $\alpha_{PR}(i)$ is estimated by adjusting PR slant range to ESCAT slant range and converting $PIA_{PR}(i)$ to normal space,

$$\alpha_{PR}(i) = 10^{-\sec\theta_{(ESCAT)}\cos\theta_{(PR)}PIA}PR^{(i)/10} \tag{3.7}$$

where $\theta_{(ESCAT)}$ is the incidence angle of the ESCAT measurement, $\theta_{(PR)}$ is the incidence angle of ith TRMM PR measurement. The attenuation observed by ESCAT α_{atm} is calculated by averaging $\alpha_{PR}(i)$ over the ESCAT footprint using Equation (3.5). The ESCAT observed PIA PIA_{atm} is

$$PIA_{atm} = -10 \log_{10} \alpha_{atm}. \tag{3.8}$$

ESCAT atmospheric backscatter (σ_{atm}) is estimated by the following procedure. First, the effective reflectivity of the atmospheric rain (Z_e) is calculated by the $Z - R$ relation [28],

$$Z_e = AR^b \ \ \mathrm{mm}^6/\mathrm{m}^3 \tag{3.9}$$

where R is the TRMM PR level 2A25 three-dimensional rain rate (mm/hr). The value of A and b depend on the type of rain. We assume typical stratiform rain value $A = 210$ and $b = 1.6$ [28] in this paper. The volume backscattering coefficient without atmospheric attenuation $\sigma_{vc}(i)$ can be computed from [13]

$$\sigma_{vc}(i) = 10^{-10} \frac{\pi^5}{\lambda_\circ^4} |K_w|^2 Z_e \ \ \mathrm{m}^{-1} \tag{3.10}$$

where $\lambda_\circ = 5.7$ cm is the wavelength of ESCAT, and $|K_w|^2$ is a function of the wavelength $\lambda_\circ$ and the physical temperature of the material. K_w is assumed to be 0.93 in this paper. The quantity σ_{vc} represents physically the backscattering cross-section (m^2) per unit volume (m^3).

By following the method in [7], the volume backscatter cross-section observed by the ESCAT is adjusted by the ESCAT-observed two-way atmospheric attenuation factor. The total atmospheric rain backscatter observed by the ESCAT at each TRMM PR measurement $\sigma_{PR}(i)$, is then calculated by integrating adjusted volume backscatter cross-section through the PR antenna beam to the lowest no-surface-

clutter range. The ESCAT observed atmospheric backscatter σ_{atm} is calculated by averaging $\sigma_{PR}(i)$ using equation (3.5).

The wind-induced surface backscatter σ_{wind} is estimated from co-located winds from ECMWF winds. As mentioned in Section 3.1, the ECMWF wind fields are interpolated in time and space to the center of each ESCAT measurement using cubic spline interpolation of the zonal and meridional components of the wind. We compute the speed and direction of the wind in meteorological convention and calculate the σ° for three antennas of each ESCAT WVC through ERS GMF (CMOD5),

$$\sigma_{wind(ECMWF)} = \text{CMOD5}(s, d, \chi, \theta) \tag{3.11}$$

where the definition of the inputs of CMOD5 is the same as in equation (3.4). The wind-induced backscatter $\sigma_{wind(ECMWF)}$ predicted by ECMWF has a bias ϵ introduced by prediction errors. Since the ECMWF wind fields are interpolated from low resolution to ESCAT resolution, the bias of ECMWF wind fields are spatially correlated in a ESCAT swath. To reduce the effect of the spatial correlation and contamination of rain on the measurements, we use a large data set (from Jan 01, 2000 to Dec 31, 2000) to estimate the ECMWF/ESCAT bias. The bias varies with incidence angle and antenna look direction, and it may change with wind speed and geophysical locations. Thus, we estimate ϵ for a specific look direction and incidence angle for each wind speed bin by making a nonparametric estimate of $\epsilon = \sigma_{m(ESCAT)} - \sigma_{wind(ECMWF)}$ as a function of wind speed at evenly spaced wind speed bins (from 0 m/s to 20 m/s with a bin-width of 1 m/s) by using an Epanechnikov kernel with a bandwidth of 3 m/s in wind speed. Only the co-located ECMWF and ESCAT data between latitude -40° and 40° are used to estimate the bias. Figure 3.3 shows the mean of ϵ for fore, mid, and aft antennae at different cross-swath WVC positions and different wind speed bins. Note that the bias is positive at low wind speed and is negative at high wind speed. The standard deviations of the bias ϵ for three antennae are less than 0.0074 for incidence angles greater than 40°. The estimate of wind-induced backscatter σ_{wind} is then represented by ECMWF-predicted wind-induced backscat-

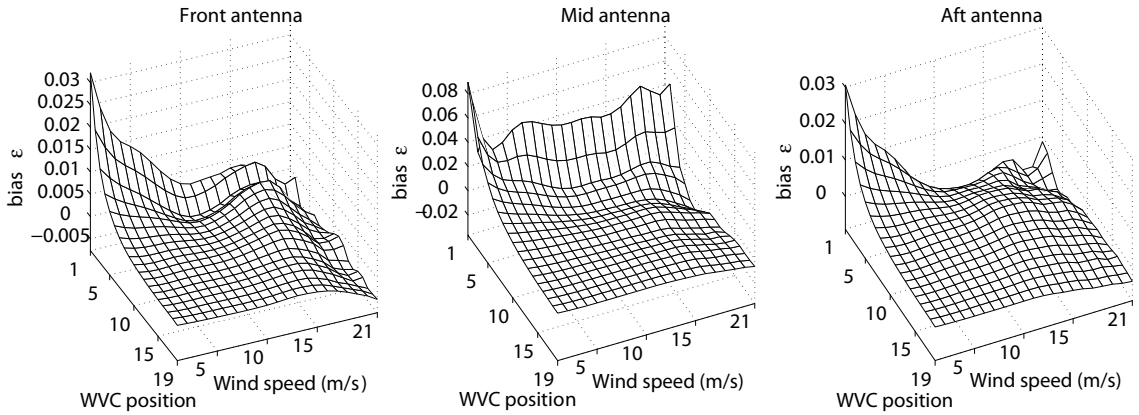

Figure 3.3: Mean biases between ECMWF predicted σ° and ERS scatterometer measured σ° for fore, mid, and aft antenna at different cross-swath WVC positions and different wind speed bins.

ter $\sigma_{wind(ECMWF)}$ and bias ϵ,

$$\sigma_{wind} = \sigma_{wind(ECMWF)} + \epsilon. \tag{3.12}$$

Based on the above parameters, we estimate the surface perturbation backscatter σ_{surf} by

$$\sigma_{surf} = \alpha_{atm}^{-1}(\sigma m - \sigma_{atm}) - (\sigma_{wind(ECMWF)} + \epsilon). \tag{3.13}$$

3.2.2 Selecting Model Function and Estimating Model Coefficients

We seek an empirical model function for equation (3.4). Power law (linear or quadratic log-log) models are sufficient to relate the three parameters with rain rate in Ku-band wind/rain backscatter model [7]. Similar functional forms work well at C-band. Thus, α_{atm}, σ_{atm}, and σ_{surf} for a specific incidence angle θ can be expressed

as polynomial functions of rain rate,

$$\begin{aligned} 10\log_{10}(PIA_{atm}(\theta)) &= 10\log_{10}(-10\log_{10}\alpha_{atm}(\theta)) \\ &\approx f_a(R_{dB}) = \sum_{n=0}^{N} x_a(n) R_{dB}^n, \end{aligned} \tag{3.14}$$

$$10\log_{10}(\sigma_{atm}(\theta)) \approx f_r(R_{dB}) = \sum_{n=0}^{N} x_r(n) R_{dB}^n, \tag{3.15}$$

and

$$10\log_{10}(\sigma_{surf}(\theta)) \approx f_{sr}(R_{dB}) = \sum_{n=0}^{N} x_{sr}(n) R_{dB}^n \tag{3.16}$$

where $R_{dB} = 10\log_{10}(R_{surf(ant)})$, $x_a(n)$, $x_r(n)$, and $x_{sr}(n)$ are the corresponding model coefficients. $N = 1$ for the linear model, and $N = 2$ for the quadratic model. Because the estimate of σ_{surf} is relatively noisy and may be negative, we first make a nonparametric estimate of σ_{surf} as a function of R_{dB} at regular logarithmically-spaced rain rate bins using an Epanechnikov kernel [29] with a 3 dB bandwidth in R_{dB}. Then, we estimate the model coefficients $x_{sr}(n)$ for the linear/quadratic model using a robust linear least-squares fit. We use a similar method in estimating $x_a(n)$ and $x_r(n)$. Since the atmospheric parameters and surface perturbation backscatter are uncorrelated with the azimuth look-direction of the antenna, we combine the data from all antennae during the coefficient estimation. To ensure sufficient data for each model fit, we use an incidence angle bin size approximately equal to 4°. Because the incidence angles of the ESCAT measurements are not uniformly distributed, the bin size is slightly increased where measurements at the incidence angle range are more rare.

In the analysis, we observe that for incidence angles less than 30°, the surface rain perturbation is not a monotonic function of surface rain rate. It cannot adequately be modeled by a linear or quadratic model. A hypothesis for the reason

Table 3.1: C-band model coefficients (linear and quadratic) of $PIA_{atm}(\theta)$.

θ (°)		$x_a(0)$	$x_a(1)$	$x_a(2)$
40-44	Linear	-18.23	1.25	
	Quadratic	-18.18	1.25	-0.00060
44-49	Linear	-17.89	1.25	
	Quadratic	-17.79	1.24	-0.0016
49-53	Linear	-17.44	1.26	
	Quadratic	-17.39	1.25	-0.00081
43-57	Linear	-17.12	1.25	
	Quadratic	-17.05	1.24	-0.0012

is that the contributions of ring waves and upper surface turbulence are comparable under such conditions. For incidence angles greater than 30°, the surface rain perturbation is monotonically increasing with surface rain rate, suggesting the contribution of ring waves dominate the surface effects of rain. We note that the Bragg wavelength of ESCAT at incidence angles higher than 30° is shorter than 5.8 cm, which is close to the wavelength condition mentioned previously. For incidence angles between 30° and 40°, the variance of the estimation of σ_{surf} is relatively large, which makes the model coefficients unreliable. Thus, in this paper we only describe the model coefficients for incidence angles greater than 40°. It is noted that due to the inhomogeneity of rain events in a ESCAT footprint, only total surface effect of rain in the backscatter measurements can be described by the model.

Graphics showing the non-parametric fits to the estimated $PIA_{atm}(\theta)$ and $\sigma_{atm}(\theta)$ with respect to R_{dB} for incidence angles between 40° and 57° are shown in Figures 3.4 and 3.5. The dashed line is the non-parametric fit. The corresponding estimated coefficients for $x_a(n)$ and $x_r(n)$ for both robust fit and quadratic fit are given in Tables 3.1 and 3.2. From these two tables, we note that all the second order coefficients of the quadratic model are negligibly small, suggesting that $PIA_{atm}(\theta)$ and $\sigma_{atm}(\theta)$ is almost a linear function of surface rain rate in log-log space.

In the derivation of $\sigma_{surf}(\theta)$, error is introduced by several sources. One of them is the prediction error of the ECMWF predicted wind-induced backscatter σ_{wind}. The procedure for estimating α_{atm} and σ_{atm} from TRMM PR level 2A25

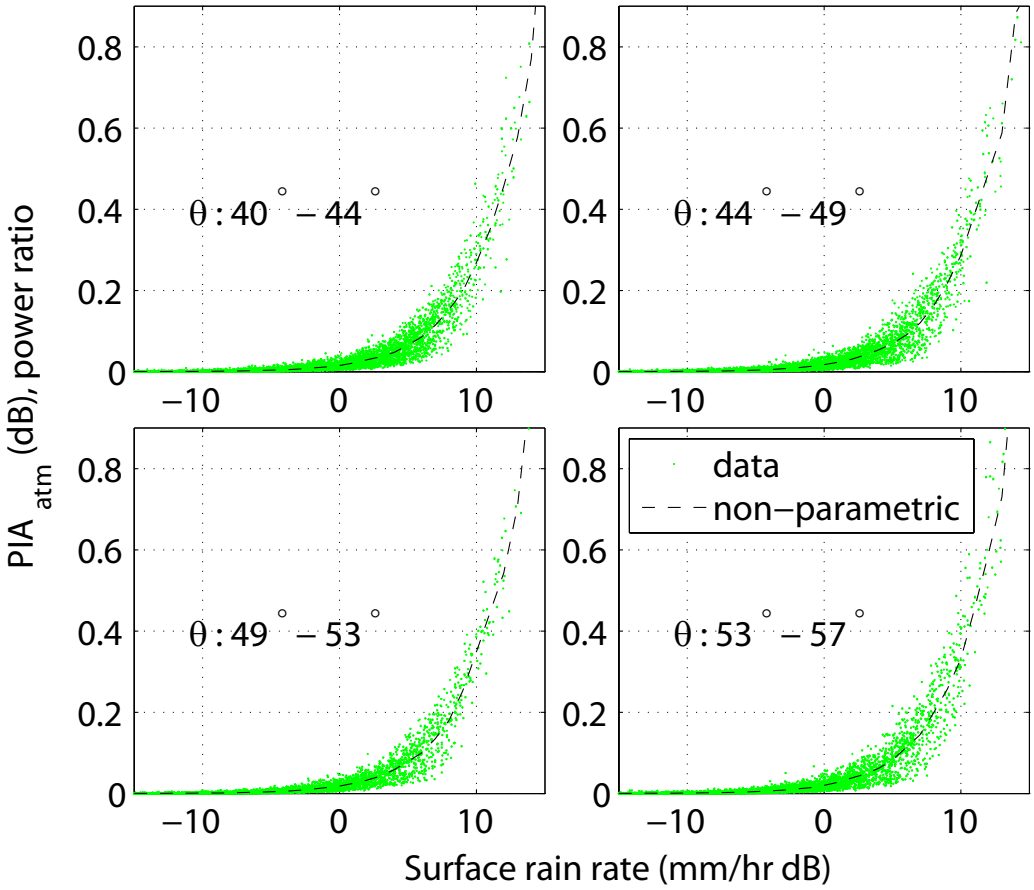

Figure 3.4: Non-parameric fit to estimated $PIA_{atm}(\theta)$ with respect to R_{dB} for different incidence angle bins. Estimated PIA is displayed in scatter plot. R_{dB} is between -15 dB and 15 dB.

Table 3.2: C-band model coefficients (linear and quadratic) of $\sigma_{atm}(\theta)$.

θ (°)		$x_r(0)$	$x_r(1)$	$x_r(2)$
40-44	Linear	-41.79	1.33	
	Quadratic	-41.76	1.33	-0.00030
44-49	Linear	-41.46	1.32	
	Quadratic	-41.44	1.32	-0.00020
49-53	Linear	-41.03	1.33	
	Quadratic	-41.07	1.33	0.00090
53-57	Linear	-40.69	1.32	
	Quadratic	-40.66	1.32	-0.00060

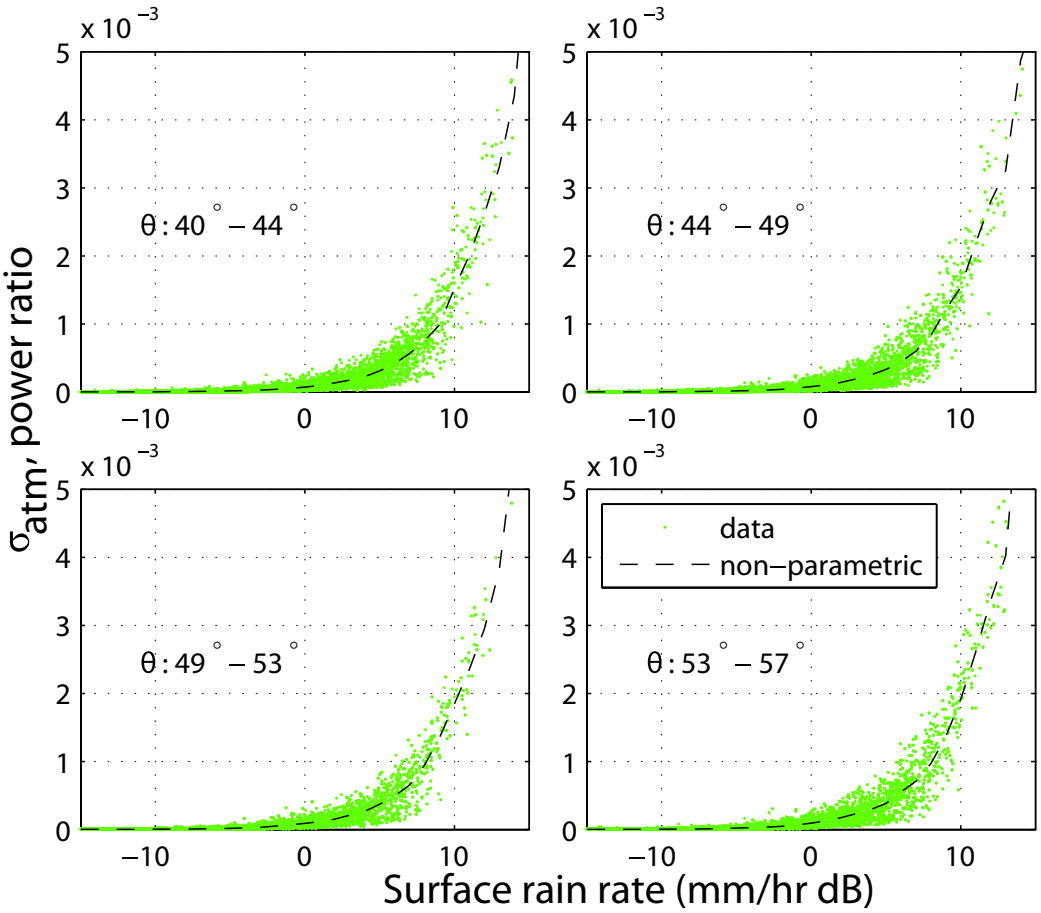

Figure 3.5: Non-parameric fit to estimated $\sigma_{atm}(\theta)$ with respect to R_{dB} for different incidence angle bins. Estimated σ_{atm} is in normal space, which is displayed in scatter plot. R_{dB} is between -15 dB and 15 dB.

three dimensional rain rate introduces additional errors due to the error of the empirical model functions, NUBF, and the temporal and spatial mismatch of ESCAT and TRMM PR measurements. We do not analyze all these errors in detail here. Instead, we evaluate the sensitivity of $\sigma_{surf}(\theta)$ to the error introduced by σ_{atm}. We adopt the combined rain model of equation (3.2) to reduce the influence of the error.

To evaluate sensitivity of $\sigma_{surf}(\theta)$ to σ_{atm}, following [7] we introduce a variable calibration parameter γ to equation (3.13)

$$\sigma_{surf} = \alpha_{atm}^{-1}(\sigma m - \gamma\sigma_{atm}) - (\sigma_{wind(ECMWF)} + \epsilon). \tag{3.17}$$

Using the method described above, we calculate the linear/quadratic model coefficients of $\sigma_{surf}(\theta)$ for each γ between 0 and 3.2 with a step of 0.1. When γ is greater than 3.2, $\sigma_{surf}(\theta)$ may become negative. We pick the optimum γ by defining a least squares objective function $f(\gamma)$ with respect to γ

$$f(\gamma) = \sum_i (\sigma_m^i - \sigma_{m(model)}^i(\gamma))^2 \tag{3.18}$$

where i is the ith data in the data set, and $\sigma_{m(model)}(\gamma)$ is the σ° calculated with the quadratic model coefficients with respect to the corresponding γ. The value of γ that minimizes $f(\gamma)$ is the optimum value γ_{opt}. For all the measurements with incidence angles between 40° and 57°, $\gamma_{opt} = 1.2$, suggesting that the estimates of σ_{atm} are slightly underestimated. The estimated coefficients of $\sigma_{surf}(\theta)$ are plotted as a function of the calibration parameter γ for different incidence angle bins in Figure 3.6. We note that none of the three terms are particularly sensitive to the value of γ, suggesting that the influence of the σ_{atm}-induced error is insignificant as expected. We list the values of $x_{sr}(n)$ corresponding to γ_{opt} in Table 3.3. Compared with the counterparts in Table 3.2, it is noted that the constant term of $\sigma_{surf}(\theta)$ is significantly higher than the constant term of $\sigma_{atm}(\theta)$, while the linear and quadratic terms of $\sigma_{surf}(\theta)$ are on the same order of magnitude as the linear and quadratic terms of $\sigma_{atm}(\theta)$.

To further compare the contribution of the surface perturbation and the atmospheric backscatter, we compute the ratio of the attenuated surface perturbation $\alpha_{atm}\sigma_{surf}(\theta)$ to the calibrated atmospheric rain backscatter $\gamma\sigma_{atm}$ with respect to R_{dB} for different incidence angle bins, which is shown in Figure 3.7. For γ_{opt}, the ratio $\alpha_{atm}\sigma_{surf}/\gamma\sigma_{atm}(\theta)$ for different θ is always greater than 3, suggesting that the surface rain backscatter always dominates the total rain-induced backscatter (but not necessarily the total backscatter).

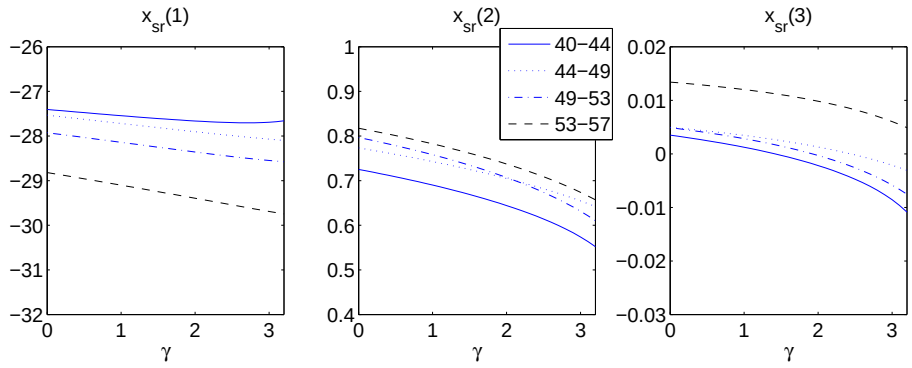

Figure 3.6: $x_{sr}(n)$ for the quadratic model as a function of the rain backscatter calibration parameter γ for different incidence angle ranges.

Table 3.3: Model coefficients of surface perturbation backscatter $\sigma_{surf}(\theta)$.

θ		$x_{sr}(0)$	$x_{sr}(1)$	$x_{sr}(2)$
40-44	Linear	-27.45	0.68	
	Quadratic	-27.78	0.7	0.0004
44-49	Linear	-27.59	0.74	
	Quadratic	-27.85	0.74	0.0031
49-53	Linear	-28.13	0.769	
	Quadratic	-28.24	0.74	0.0031
53-57	Linear	-28.582	0.846	
	Quadratic	-29.14	0.773	0.0116

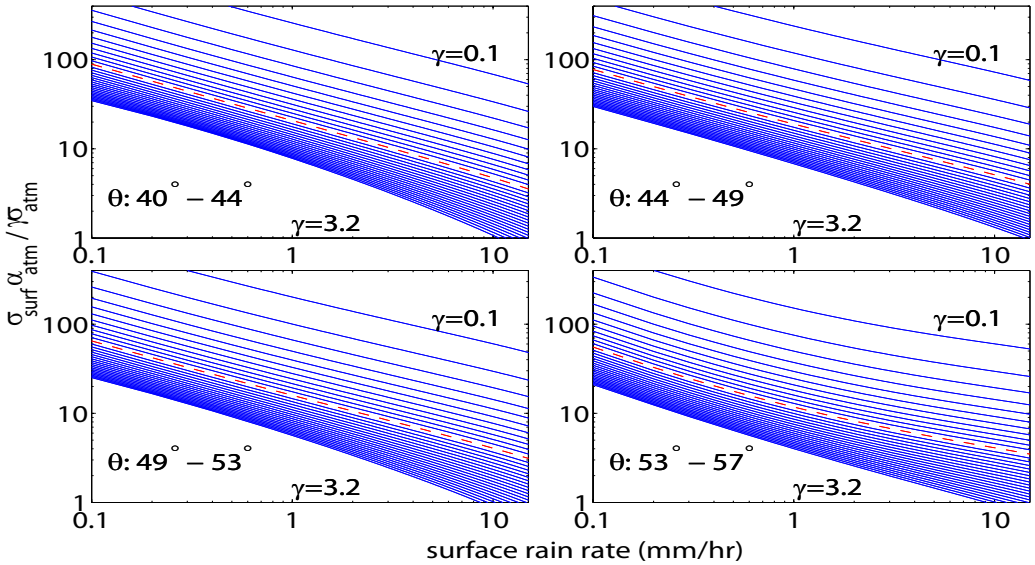

Figure 3.7: Ratio of the attenuated surface perturbation $\alpha_{atm}\sigma_{surf}(\theta)$ to the calibrated atmospheric rain backscatter $\gamma\sigma_{atm}$ for different γ in the range 0.1 to 3.2 with a step of 0.1 separately plotted as a function of rain rate for several incidence angle ranges. Dashed line corresponds to γ_{opt}.

Table 3.4: Model coefficients of effective rain backscatter $\sigma_{eff}(\theta)$.

θ		$x_{eff}(0)$	$x_e(1)$	$x_e(2)$
40-44	Linear	-27.21	0.703	
	Quadratic	-27.60	0.728	0.0016
44-49	Linear	-27.37	0.759	
	Quadratic	-27.61	0.76	0.0030
49-53	Linear	-27.87	0.797	
	Quadratic	-27.96	0.768	0.0034
53-57	Linear	-28.19	0.851	
	Quadratic	-28.78	0.791	0.0109

It is noted that we only care about the total effect of rain in wind retrieval. The corresponding power law model of σ_{eff} is

$$10\log_{10}(\sigma_{eff}(\theta)) \approx f_e(R_{dB}) = \sum_{n=0}^{N} x_e(n) R_{dB}^n. \tag{3.19}$$

The coefficients of $x_e(n)$ are calculated using the same method mentioned before, shown in Table 3.4, and plotted in Figure 3.8. The estimated $\sigma_{eff}(\theta)$ is shown in the density plot. The dashed line is the non-parametric fit. Figure 3.9 shows the non-parametric fit and linear/quadratic fits in log-log space.

We further investigate the relationship between $\sigma_{eff}(\theta)$ and incidence angle θ by plotting the $\sigma_{eff}(\theta)$ with respect to θ for a specific surface rain rate in Figure 3.10. We use the quadratic model coefficients to estimate $\sigma_{eff}(\theta)$ for θ between 40° and 57°. At a low rain rate, the magnitude of σ_{eff} generally decreases with incidence angle. At a moderate rain rate, the σ_{eff} almost remains constant for all incidence angles. At a heavy rain rate, σ_{eff} increases with incidence angle. It is also noted that wind-induced backscatter $\sigma_{wind}(\theta)$ decreases with incidence angle. Thus, rain-induced backscatter has more impact on the C-band scatterometer measurements at high incidence angle than at low incidence angle.

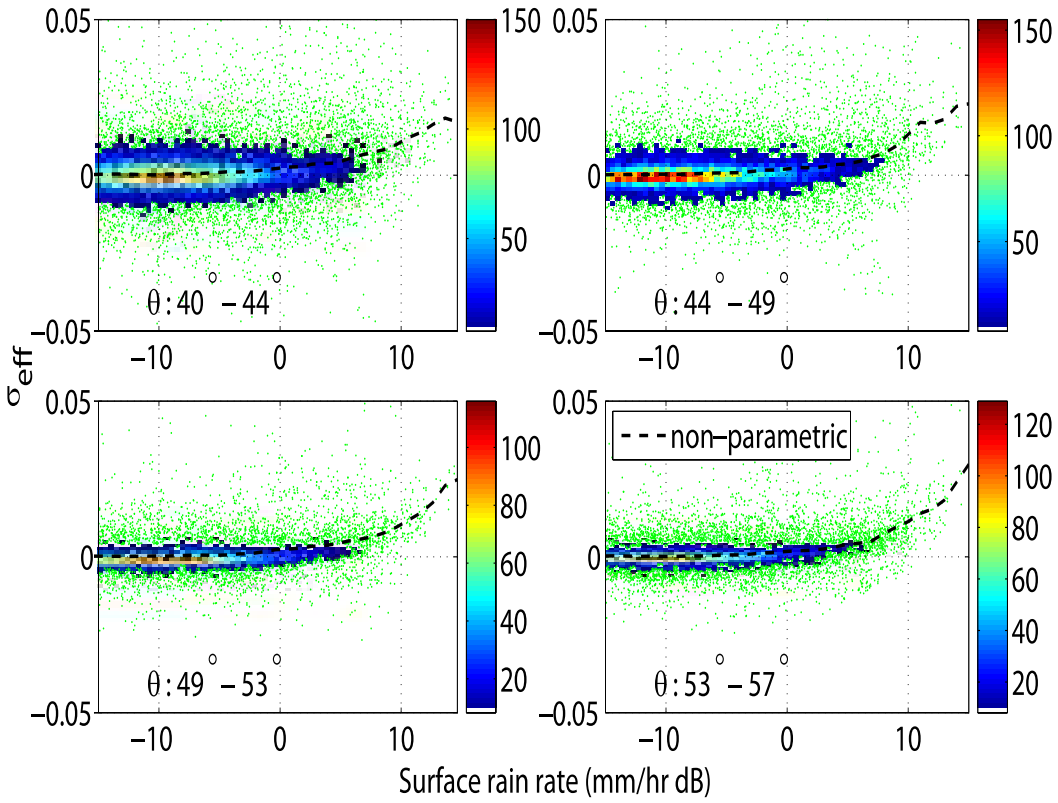

Figure 3.8: Non-parametric fits to the effective rain backscatter σ_{eff} in log-normal space for different incidence angle bins. The dashed line is the non-parametric fit. Data is shown in a density plot.

3.3 Model Validation and Data Regimes

In this section, we validate the rain/wind model by comparing the model estimated backscatter $\sigma_{m(model)}(\theta)$ to actual ESCAT backscatter measurements $\sigma_{m(ESCAT)}(\theta)$ for different surface rain rate bins in Figures 3.12 and 3.14. $\sigma_{m(model)}(\theta)$ is estimated using the quadratic model. To illustrate the difference in using the wind/rain model, we also show a scatter-plot of $\sigma_{m(ESCAT)}(\theta)$ with respect to ECMWF predicted wind-only backscatter $\sigma_{wind(ECMWF)}(\theta) + \epsilon$ for the same rain rate bin and incidence angle bin in Figures 3.11 and 3.13. It is noted that rain introduces a bias to the backscatter, with the bias increasing with rain rate and incidence angle. After applying the wind/rain model, the rain-induced bias is eliminated. For θ ranging from 40° to 49°, 95% of the model predicted backscatter is within 3 dB of the ESCAT measured backscatter, while the standard deviation of log

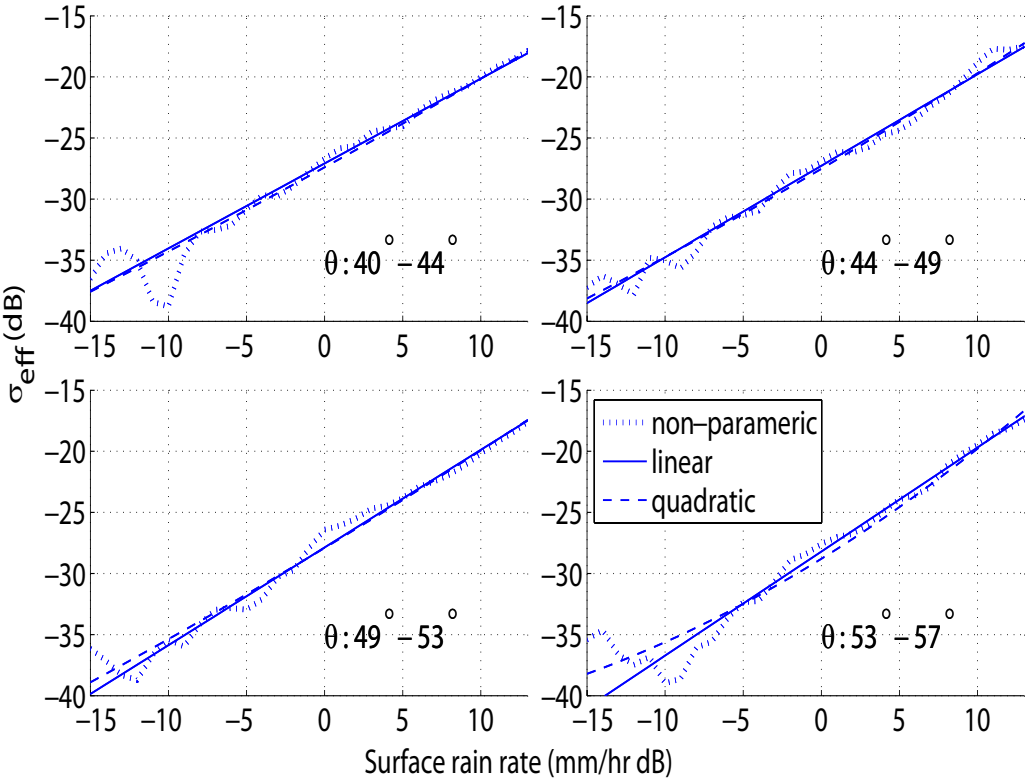

Figure 3.9: Linear and quadratic fits to the non-parametric fits of effective rain backscatter σ_{eff} in log-normal space for different incidence angle bins. Non-parametric fits are also plotted.

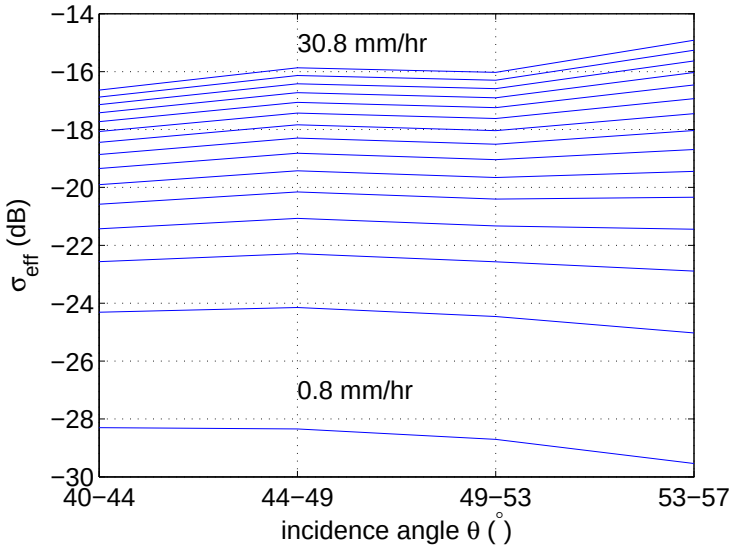

Figure 3.10: Relationship between $\sigma_{eff}(\theta)$ and incidence angle for several surface rain rates (mm/hr). Rain rates range from 0.8 mm/hr to 30.8 mm/hr with a step of 1 mm/hr.

error, $\sigma_{m(model)}(\theta) - \sigma_{m(ESCAT)}(\theta)$, is 1.4 dB. For θ ranging from 49° to 57°, the percentage is 91% and the standard deviation is 1.6 dB.

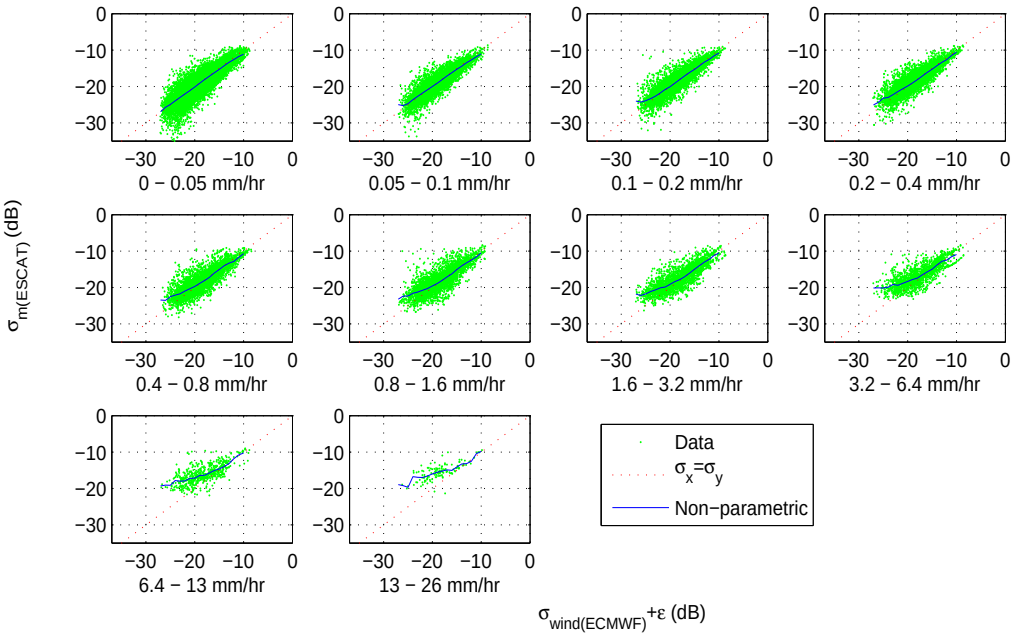

Figure 3.11: ESCAT measured backscatter $\sigma_{m(ESCAT)}$ plotted as a function of wind-only backscatter $\sigma_{wind(ECMWF)} + \epsilon$ for incidence angles $40° - 49°$ for different rain rate bins. A nonparametric fit is also plotted.

To further validate the model, we compute a non-parametric estimate of both $\sigma_{m(ESCAT)}(\theta)$ and $\sigma_{m(model)}(\theta)$ on a regular grid with axes of $\sigma_{wind(ECMWF)}+\epsilon$ and R_{dB} using a two-dimensional Epanechnikov kernel with a bandwidth of 3 dB for different incidence angle bins. $\sigma_{m(model)}(\theta)$ is calculated using the quadratic combined rain model. The log error is computed as $\sigma_{m(model)}(\theta) - \sigma_{m(ESCAT)}(\theta)$ in dB. Figure 3.15 shows nonparametric estimates of $\sigma_{m(ESCAT)}(\theta)$, $\sigma_{m(model)}(\theta)$, and the log error with respect to $\sigma_{wind(ECMWF)}+\epsilon$ and the surface rain rate (mm/hr dB) for different incidence angle bins. For the two incidence angle bins shown, the model estimated backscatter is very close to the ESCAT measured backscatter, with a log error within ±2dB. It is noted that the largest error occurs at high rain rates due to less data.

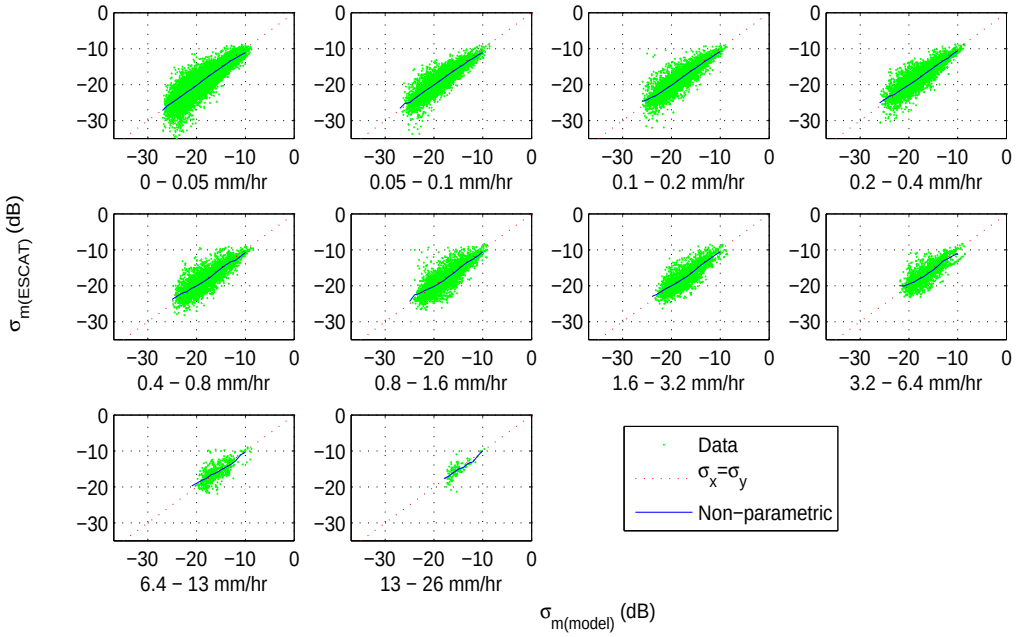

Figure 3.12: ESCAT measured backscatter $\sigma_{m(ESCAT)}$ plotted as a function of of model estimated backscatter $\sigma_{m(model)}$ with the quadratic model for incidence angles $40° - 49°$ for different rain rate bins. A nonparametric fit is also plotted.

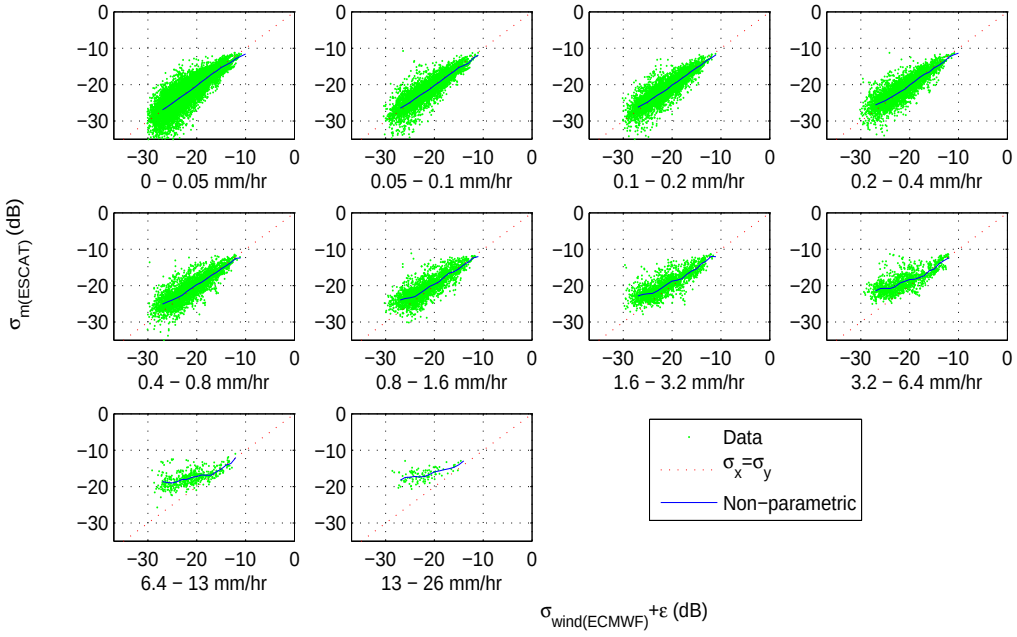

Figure 3.13: ESCAT measured backscatter $\sigma_{m(ESCAT)}$ plotted as a function of wind-only backscatter $\sigma_{wind(ECMWF)} + \epsilon$ for incidence angles $49° - 57°$ for different rain rate bins. A nonparametric fit is also plotted.

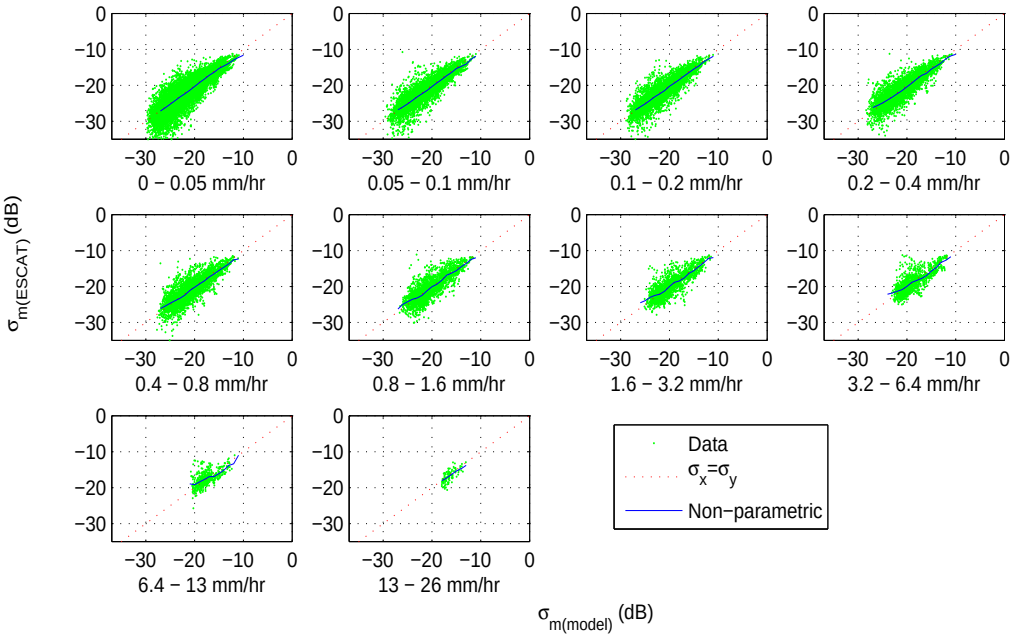

Figure 3.14: ESCAT measured backscatter $\sigma_{m(ESCAT)}$ plotted as a function of model estimated backscatter $\sigma_{m(model)}$ with the quadratic model for incidence angles $49^\circ - 57^\circ$ for different rain rate bins. A nonparametric fit is also plotted.

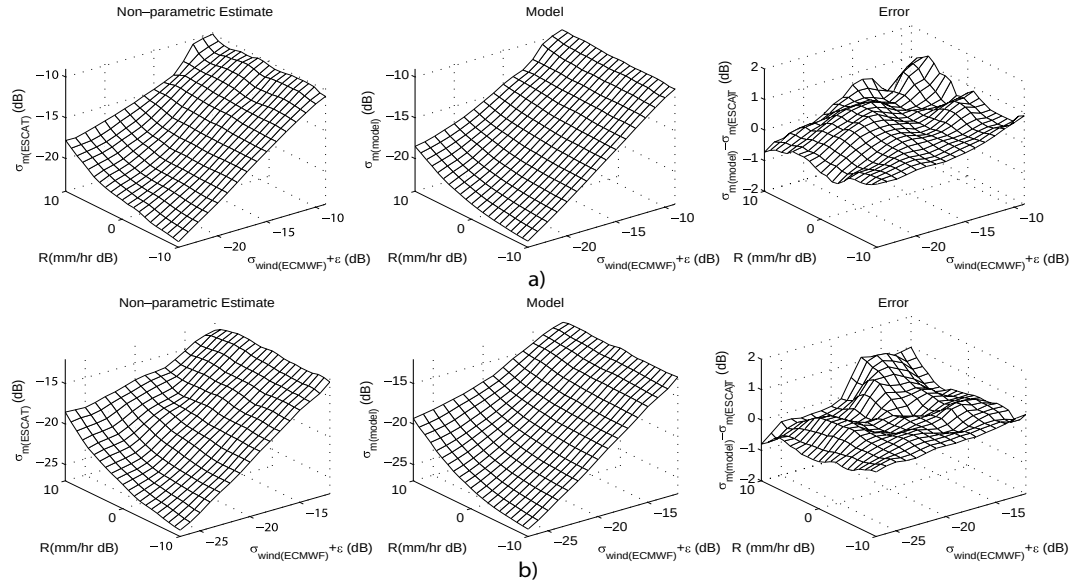

Figure 3.15: Nonparametric estimates of $\sigma_{m(ESCAT)}(\theta)$, $\sigma_{m(model)}(\theta)$, and the difference are plotted with respect to $\sigma_{wind(ECMWF)}+\epsilon$ and surface rain rate R(mm/hr dB) for incidence angles in range of a) $40^\circ - 49^\circ$ and b) $49^\circ - 57^\circ$.

To understand the effect of rain on the scatterometer measurements for different incidence angles, following [7] we define three distinct backscatter regimes. In regime 1, rain-induced backscatter dominates the total backscatter. Regime 2 is where the rain-induced backscatter and the wind-induced backscatter are on the same order of magnitude. In regime 3, wind-induced backscatter dominates the total backscatter. It is noted that wind and rain information may be simultaneously retrieved from regime 2, while in regime 1 or regime 3, only the dominating parameter (wind or rain) can be retrieved. We identify these regimes by thresholding the ratio $\tau = \sigma_{\mathit{eff}}/\sigma_m$. We define regime 1 by $\tau > 0.75$, regime 3 as $\tau < 0.25$, and regime 2 as $0.75 \geq \tau \geq 0.25$. In Figure 3.16, we plot the τ computed using the combined wind/rain model with respect to surface rain rate R_{dB} and wind-only backscatter σ_{wind}, with the three regimes shown in different colors. We also plot contours of predicted total backscatter σ_m. We choose the range of σ_{wind} for different incidence angles using three standard deviations from the mean, accounting for roughly 95% of the co-located data set. It is noted that with the increasing of surface rain rate, the curve of σ_m deviates from the curve of σ_{wind}. As the incidence angle increases, the area of regime 1 reduces while the area of regime 3 increases, suggesting that rain has more significant impact on the ESCAT measurements at higher incidence angles.

We further investigate this by computing the percentage of co-located measurements falling in each regime with significant rain ($\geq$ 0.8 mm/hr) and ECMWF wind speed greater than 2 m/s, listed in Table 3.5. It is noted that about 3% of all the co-located ESCAT measurements observe significant rain ($\geq$ 0.8 mm/hr). To investigate the relationship between the data regimes, wind speed, and rain rate, we plot mean τ with respect to ECMWF predicted wind speed and average surface rain rate (mm/hr) for all the co-located measurements with significant rain ($\geq$ 0.8 mm/hr) and ECMWF wind speed grater than 2 m/s in Figure 3.17, with a bin width of 4 m/s for wind speed and a bin width of 4 mm/hr for surface rain rate. It is noted that regime 1 ($\tau > 0.75$) mostly happens at low wind speed and high rain conditions, suggesting rain has a significant impact on the total backscatter in such conditions.

Table 3.5: Percentage falling in each regime of co-located measurements with significant rain (≥ 0.8 mm/hr) and ECMWF wind speed greater than 2 m/s.

$\theta(^\circ)$	Regime 1	Regime 2	Regime 3
40-44	0.64%	27.38%	71.98%
44-49	2.27%	41.38%	56.35%
49-53	5.17%	52.87%	41.96%
53-57	5.75%	49.74%	44.51%

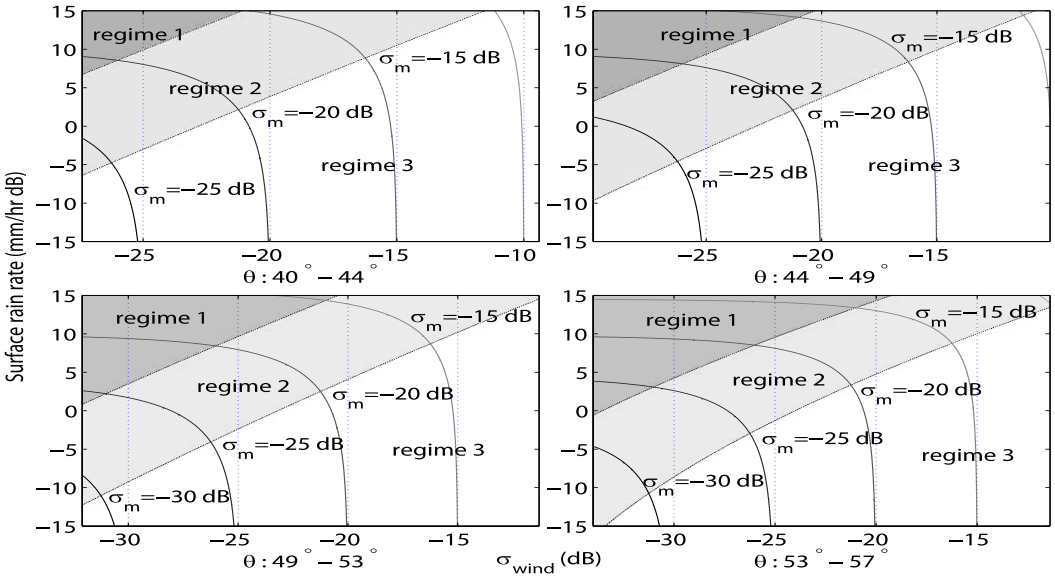

Figure 3.16: Backscatter regimes for ESCAT as a function of rain rate and effective wind backscatter for several incidence angles. Also plotted is a contour plot of the combined rain effect model for σ_m (solid lines) and σ_{wind} (dotted lines).

3.4 Conclusions

With the confirmed existence of rain surface perturbation by recent studies, the rain effect on C-band scatterometer measurements needs to be reevaluated. By using co-located TRMM PR, ESCAT on ERS, and ECMWF data, we develop and evaluate a simple low-order wind/rain backscatter model which inputs surface rain rate, incidence angle, wind speed, wind direction, and azimuth angle. By applying the model to the co-located data set, we demonstrate that the wind/rain backscatter model is accurate enough for describing the total backscatter in raining areas with rel-

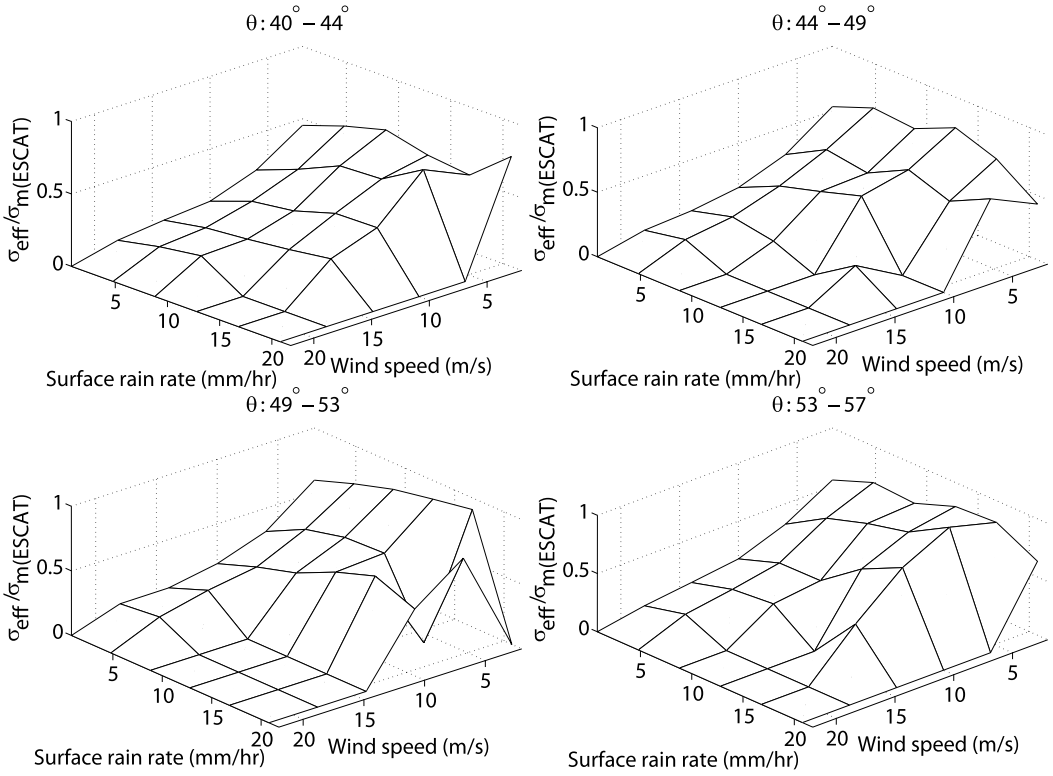

Figure 3.17: Mean σ_{eff}/σ_m with respect to ECMWF predicted wind speed and TRMM PR measured surface rain rate for different incidence angle bins. The wind speed ranges from 2 m/s to 22 m/s with a bin width of 4 m/s. The surface rain rate ranges from 0.8 mm/hr to 20.8 mm/hr with a bin width of 4 mm/hr.

atively low variance. We also show that the rain surface perturbation is a dominating factor of the rain-induced backscatter.

Using three distinct regimes, we identify under what conditions wind and rain can be retrieved from the measurements. In regime 1 where rain dominates, only rain information may be retrieved from the measurements. In regime 3 where wind dominates, only wind information can be retrieved. In regime 2 where rain and wind are comparable, wind and rain information may be simultaneously retrieved from the measurements. In regime 1 and regime 2, the current wind retrieval methods are inadequate to retrieve the correct wind information. Therefore, the rain model should be incorporated into the retrieval algorithm. For incidence angle bins 40° to

44°, 44° to 49°, 49° to 53°, and 53° to 57°, about 0.9%, 1.3%, 1.74%, and 1.67% of all the co-located ESCAT measurements are affected by rain (falling in regime 1 or 2).

We also show that rain has more impact on the C-band measurements at higher incidence angles. Since the successor of ESCAT on ERS, the advanced scatterometer instrument (ASCAT) on MetOp, has incidence angles ranging from 25° to 65°, the measurements of ASCAT are expected to be more sensitive to rain than ESCAT on ERS.

Due to the beam-filling effect and variance of the ECMWF predicted σ°, relative large variance is shown in the model for low rain data. But the majority of the data (95% for 40° to 49° and 91% for 49° to 57°) lies within 3dB of the model. This illustrates how well the model performs. In fact, ESCAT retrieved wind vector are mainly affected by mid to heavy rain at high incidence angles. The model is expected to retrieve rain rate and improve retrieved wind vector in such situations. Chapter 4 introduces a C-band simultaneous wind/rain retrieval method using this wind/rain backscatter model. This new method improves the rain-corrupted wind estimates and retrieves the surface rain with relatively high accuracy in moderate to heavy rains. The new method will also benefit wind retrieval for ASCAT.

Chapter 4

A C-band Simultaneous Wind/Rain Retrieval Method

The previous chapter demonstrates that ESCAT measurements can be adversely affected by moderate to heavy rains at high incidence angles due to the surface effects of rain [11] [9] [30]. Because conventional wind-only retrieval does not explicitly account for the sensitivity of backscatter measurements to rain, rain contamination introduces errors to retrieved wind velocities, particularly at high incidence angles. In order to prevent adverse rain impact on retrieved winds, Quality Control (QC) methods [31] [32] [33] are used to discard rain contaminated measurements which causes loss of coverage. Since the successor of ESCAT, the advanced scatterometer instrument (ASCAT) on the MetOp-A satellite, has higher incidence angle coverage than ESCAT, wind retrieval from ASCAT measurements is expected to be more sensitive to rain. Hence evaluating the influence of rain on ESCAT wind retrieval and developing improved wind retrieval methods are necessary for improving the accuracy and coverage of C-band scatterometer wind estimations in raining areas. Furthermore, rain rate information can be estimated simultaneously [7], which is a side benefit of the new wind retrieval method. Based on the simultaneous wind/rain retrieval method (SWRR) retrieved rain rate, an improved rain flagging method can be developed for ESCAT.

Wind retrieval from scatterometer measurements over the ocean is generally an inversion of the geophysical model function (GMF) which describes σ°, the normalized scatterometer backscattering cross-section, as a function of wind velocity, incidence angle, and polarization. The inversion is generally based on maximum likelihood estimation (MLE). Due to symmetry in the GMF and noise, multiple solutions (defined as "ambiguities") are found when minimizing the MLE cost function. After

applying an ambiguity removal algorithm, a unique wind estimate is selected for a specific wind vector cell (WVC).

To evaluate the effects of rain on C-band wind-only retrieval, we use collocated wind velocities from ESCAT wind-only retrieval, surface rain rates from the Tropical Rainfall Measuring Mission (TRMM) Precipitation Radar (PR), and numerical predicted wind velocities from European Medium-Range Weather Forecasts (ECMWF). The ESCAT data and TRMM PR measurements are collocated within ± 15 minutes. About 82181 collocations are collected from a period of sixteen months between August 01, 1999 and December 31, 2000. To ensure the quality of the analysis, only the collocations where the overlapping PR swath contains more than 2.5% of the measurements flagged as rain-certain in the TRMM level 2A25 data are used in the study. The ECMWF-predicted wind fields are trilinearly interpolated in space and time to the ESCAT data times and locations. The spatial resolution of the ECMWF winds is $1^\circ \times 1^\circ$ latitude-longitude with a temporal resolution of 6 hours.

To compensate for rain-induced backscatter, the C-band wind/rain backscatter model proposed in Chapter 2 is applied in the wind retrieval process to develop a simultaneous wind/rain retrieval method for ESCAT. The method retrieves surface rain rates and wind vectors simultaneously using an adjusted MLE. Because the backscatter model is only usable at incidence angle $> 40^\circ$, we implement SWRR for data at WVC $13 - 19$. Conventional wind-only retrieval is used at low incidence angles.

In Section 4.1, degradation of the rain on the wind-only wind retrieval results is evaluated and analyzed. Following that, we describe the methodology of simultaneous wind/rain retrieval (SWRR) in Section 4.2. The normalized standard deviation of rain-induced backscatter is estimated in Section 4.3. In Sections 4.4 and 4.5, we evaluate the performance of SWRR by simulation and using the collocated data set. In Section 4.6, a case study is presented. Conclusions are reached in Section 4.7.

4.1 Rain Effects on ESCAT Wind-Only Wind Retrieval

In this section, we briefly describe the background of conventional wind-only retrieval and analyze the impact of the rain on the wind retrieval procedure by simulation. We then evaluate the real rain effect on wind-only retrieval using the collocated data set.

4.1.1 Conventional Wind-only Retrieval

For ESCAT, the wind-only retrieval process involves inversion of the GMF given σ° triplet measurements. Here, the wind-only GMF inversion method is based on minimization of a simplified maximum likelihood estimator (MLE), assuming Gaussian noise and independent samples,

$$\mathbf{MLE}(z|s,d) = \sum_{i=1}^{3} \frac{\Big(\sigma_i^\circ - \mathbf{M}(s,d,\phi_i,\theta_i)\Big)^2}{\Big(\varsigma_i(s,d)\Big)^2} \tag{4.1}$$

where σ_i° is the measured σ° value, $\mathbf{M}$ is the GMF, s is the wind speed, d is the wind direction, ϕ_i is the azimuth angle of the radar beam, and θ_i the incidence angle of the radar beam. The index i indicates antenna beam position. ς_i is the variance of measurements, which is a measure of the noise in the σ° measurements. The variance ς_i is affected by many factors, including uncertainty in GMF, signal noise due to fading, thermal noise, and beam-filling effects. It can be expressed as $\varsigma_i(s,d) = K_p\mathbf{M}(s,d,\phi_i,\theta_i)$ where K_p is the normalized standard deviation of the measurements. K_p can be expressed as a combination of K_{pm}, the normalized standard deviation of GMF, and K_{pc}, the normalized standard deviation of the communication or signal noise [1]

$$K_p = \sqrt{K_{pc}^2 + K_{pm}^2 + K_{pc}^2 K_{pm}^2}. \tag{4.2}$$

In general, the term K_{pc} has the form

$$K_{pc} = \sqrt{\alpha + \frac{\beta}{\sigma_t} + \frac{\gamma}{\sigma_t^2}} \tag{4.3}$$

where α, β, and γ are coefficients depending on fading characteristics of the surface scatters and the signal to noise ratio (SNR) at the receiver [1] [17], and σ_t is the true σ° of the ocean surface without communication noise. Since the measurement SNR for ESCAT is very high, K_{pc} is small compared with the geophysical-modeling error K_{pm} [16]. Lacking an accurate model for K_{pc}, K_{pc} is assumed to be constant for ESCAT, typically 0.05. The geophysical-modeling error K_{pm} is caused by many factors. One of them is the uncertainty of GMF, since the empirical GMF is not an exact relationship. Many parameters not included in the GMF, such as local salinity, temperature, and long waves, can change the observed σ° for a fixed wind velocity. Beam filling, which is due to the wind variability within the resolution cell and the non-uniform spatial averaging inherent in the radar measurements is another factor for K_{pm} [7] [18].

Minimization of the MLE results in 1 to 4 local minima (ambiguities), which represent possible wind vector solutions. The two primary ambiguities correspond to the two most likely solutions, differing by about 180° in direction. The occurrence and location of the other ambiguities often depend on the normalization [18]. A method proposed by Stoffelen and Anderson transforms the measurements to a z space by the form $z = (\sigma^\circ)^{0.625}$ and results in a circular distribution that is ideal for inversion [18].

Due to multiple ambiguities, an ambiguity removal procedure must be implemented to choose one unique solution. The ambiguity removal procedure uses median filtering and nudging techniques to choose the best solution. For ESCAT wind-only retrieval, a selection filter is implemented to iteratively select the ambiguity at each WVC, based on a weighted average of the differences from the surrounding WVCs. At each WVC, the selection filter is nudged by the ECMWF Model First Guess at Appropriate Time (FGAT) wind vectors [18].

4.1.2 Analysis of Rain on Wind Retrieval

As mentioned in Chapter 4.2, rain surface backscatter can dominate the total backscatter under conditions of low to medium wind speed and heavy rain at high incidence angles. Using the C-band wind/rain backscatter model described in Equation (3.2) and (3.3), we show how rain affects the conventional wind-only wind retrieval process by simulation under typical low wind and heavy rain cases for WVCs with high incidence angles. To visualize the wind retrieval procedure, we use the locus of wind velocities that give rise to a single σ° for fixed radar incidence and azimuth angles. Figure 4.1 shows a plot of σ° for three sets of radar angles representative of simulated data with rain (in (a)-(d)) and without rain (in (e)-(f)) from the ESCAT scatterometer for WVC 13 and 19. These plots are generated by choosing a wind speed and direction and calculating σ° values using the wind/rain backscatter model. For each set of radar incidence and azimuth angle, all the wind speeds and directions that induce the specific σ° are plotted as a single curve.

As shown in Fig. 4.1(a)-(d), the three measurements without noise from the fore, middle, and aft beams have an intersection corresponding to the true wind velocity. Due to upwind/downwind similarity, there is a near intersection point about 180° from the true wind direction. In the presence of rain, the magnitude of backscatter increases and tends toward isotropic. Because of the viewing geometry of ESCAT measurements, under the condition of heavy rain the two primary minima tend to be at approximately $180^\circ \pm 14^\circ$ direction and $360^\circ \pm 14^\circ$ regardless of the true wind speed. These directions correspond to the along swath direction, as shown in Fig. 4.1(e)-(h). Figure 4.1(b) also shows that the wind speeds corresponding to the intersections are biased high. Comparing the plots for WVC 13 (with incidence angle 48.5° for fore and aft beam, and 37.7° for mid beam) and WVC 19 (with incidence angle 57° for fore and aft beam, and 45° for mid beam), the speed bias becomes more serious for higher incidence angles. To demonstrate this phenomenon, noise-free σ° at WVC 19 for three antenna beams under rain-free and rain-dominant conditions are compared in Fig. 4.2. In Fig. 4.2(a), the triplet σ° are plotted at the true relative wind direction. The GMF corresponding to true wind speed (7 m/s) is plotted as a

function of relative wind direction χ. The triplet measurements show azimuth and incidence angle dependence, which is important for wind retrieval. In Fig. 4.2(b), the three rain-altered σ° are plotted at the relative wind directions corresponding to along-cross directions. The GMF corresponding to a wind speed of 17.5 m/s for three beams are plotted. When rain dominates the backscatter, the σ° from the three beams is close to isotropic. As shown in Fig. 4.2(b), the markers representing σ° agree with the corresponding GMF lines. Hence the selected direction ambiguity is always at along-track directions. Similar results are found for rain-corrupted wind estimates from Ku-band scatterometers [2] [34], though the direction estimate aligns cross-track in this case. The different wind direction features of the rain-corrupted estimates from the two scatterometers are mainly due to the different antenna viewing geometries of the two instruments.

4.1.3 Rain Effects on Wind-Only Vectors

After a brief theoretical analysis, we evaluate the effect of rain on the wind-only retrieved wind estimates using the collocated data set. To illustrate the influence of rain, we investigate the statistics of the wind speed and the wind direction retrieved from rain-free and rain-corrupted σ° measurements for different WVC positions and rain rate ranges. Fig. 4.3 shows the mean of the difference between the selected wind speed ambiguity and the collocated ECMWF wind speed ($s_{ERS} - s_{ECMWF}$) for rain-free and rain corrupted (rain rate > 3 mm/hr) cases at WVCs of $1-5$, $6-11$, $12-15$, and $16-19$. As a reminder, the incidence angles of triplet measurements increase with WVC number. The selected wind speeds have no obvious bias under rain-free condition. Under moderate to heavy rains, the selected wind speeds are biased high and the bias in the wind speed increases from low WVC to high WVC, revealing that the rain impact on wind speed estimation becomes more significant with incidence angle.

We compare the normalized histograms of selected wind speed and wind direction for rain-free and rain-corrupted conditions and ECMWF wind speed for rain-free data in Figs. 4.4 and 4.5(a) for the same WVCs. The normalized histograms of se-

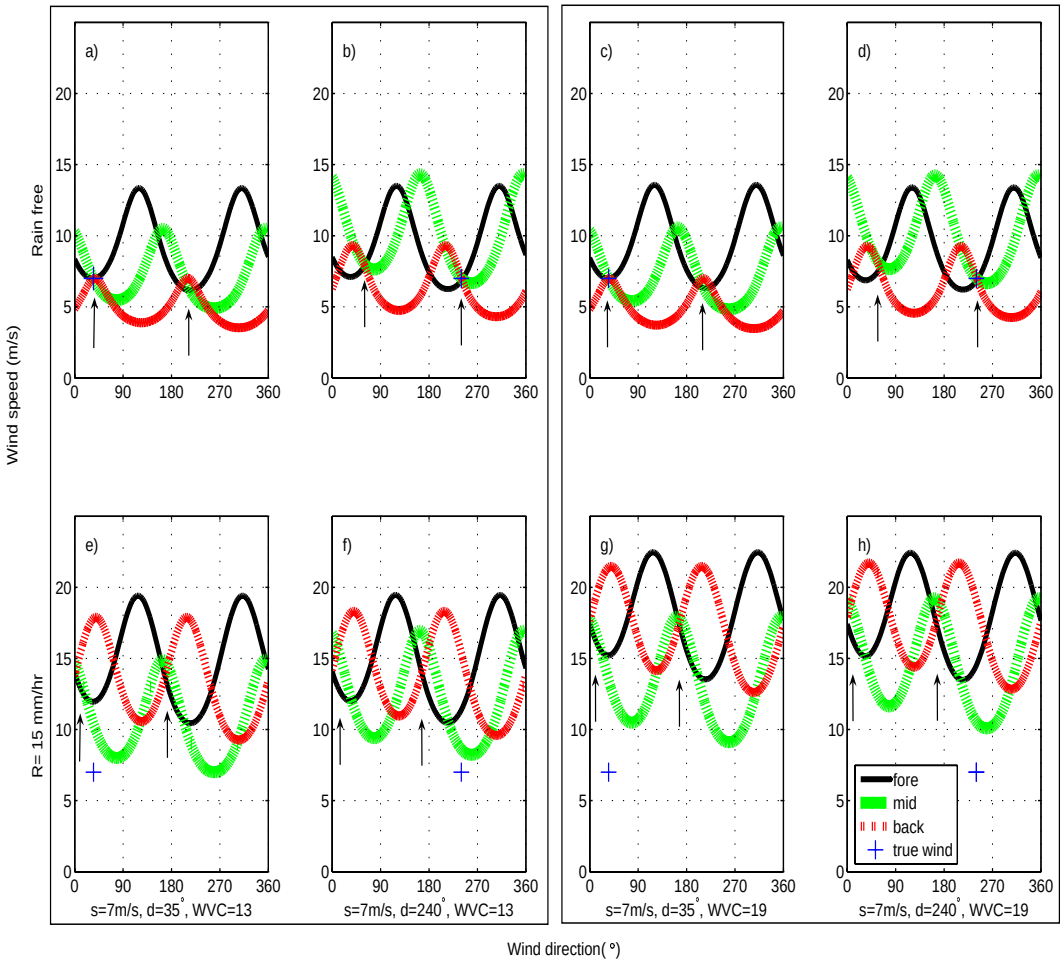

Figure 4.1: Visualization of the wind retrieval procedure for data in WVC 13 (left panel, $\theta_{fore/aft} \approx 48.6°$ and $\theta_{mid} \approx 37.7°$) and 19 (right panel, $\theta_{fore/aft} \approx 56.6°$ and $\theta_{mid} \approx 45.4°$). The intersections of the three curves correspond to the true wind velocity and aliases. The arrows in the plots point to the two major ambiguities. (a)-(d) shows the wind retrieval procedure for rain-free data, while (e)-(h) shows the procedure for rain-corrupted data. The true wind speed is 7 m/s. The true wind directions are 35° and 240°. The true wind vector is shown as "+" in the plots. The true rain rate is 31.6 mm/hr. When the backscatter is dominated by rain, intersections tend to be associated with along track directions.

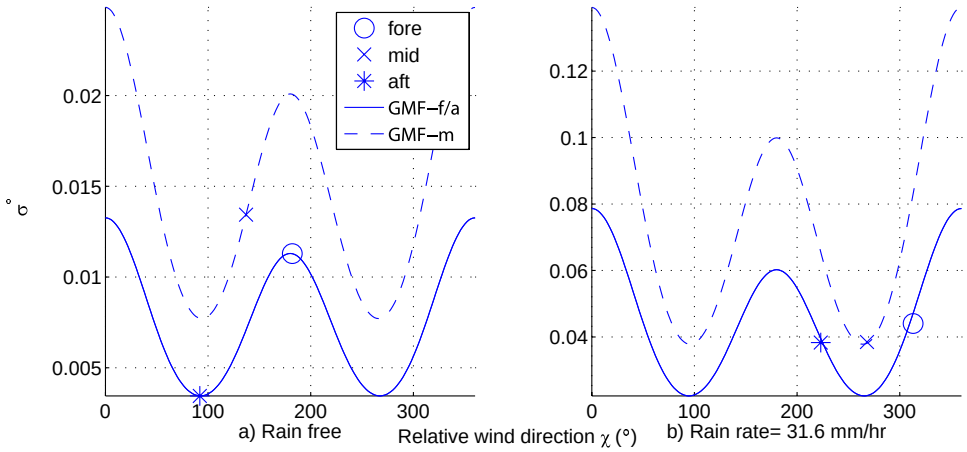

Figure 4.2: Illustration of the rain effect on ESCAT backscatter during a rain dominant case at WVC 19. The true wind speed is 7 m/s. The true wind direction is 35°. (a) Shows the noise-free backscatters (simulated using CMOD5) for fore, mid, and aft beams, plotted with GMF as a function of relative wind direction. The dashed line is the GMF for mid beam, while the solid line is the GMF for fore/aft antennas, assuming the fore/aft antennas have the same azimuth angle. (b) Plots the rain-corrupted backscatter (simulated using the C-band wind/rain backscatter model) at the azimuth angles corresponding to the along-track directions. The GMF corresponding to $s = 17.5$ m/s for mid and fore/aft beams are plotted in dashed and solid lines, respectively. Note that rain-domination makes the backscatter almost isotropic, which agree with the corresponding σ° at $d = 180^\circ - 14^\circ$. Hence the retrieved wind direction is at along-track.

lected wind speed and ECMWF wind speed are consistent for rain-free conditions. The speed densities of the rain-corrupted data gradually shift to the right from WVC with low to high incidence angles, which is consistent with the results in Fig. 4.3. For wind directions, the histogram of the rain-free selected wind directions agrees well with the collocated ECMWF wind direction. With the presence of rain, peaks develop, revealing that the rain-corrupted wind directions are gradually biased toward the along-track direction. The along-track direction bias becomes more serious with increasing incidence angles.

To evaluate the performance of wind-only MLE, we show the normalized histogram of the wind ambiguity closest to the collocated ECMWF wind for the same rain conditions and WVC. We plot the normalized histogram of the wind direction ambiguity closest to the collocated ECMWF wind for rain-free and rain-corrupted cases at WVCs of $1-5$, $6-11$, $12-15$, and $16-19$ in Fig. 4.5(b). For rain-corrupted

measurements at WVCs with high incidence angles, most of the closest wind direction ambiguities align with the along-track or cross-track directions. For these cases wind-only MLE cannot retrieve the correct wind direction.

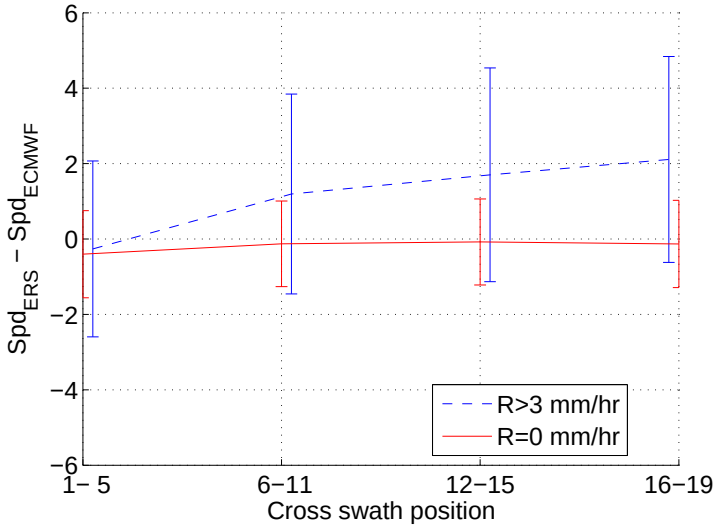

Figure 4.3: The mean of the difference between the wind-only retrieval method selected wind speed ambiguity and collocated ECMWF wind speed under conditions of rain-free, and over 3 mm/hr rain rate for different WVC bins. Error bar in the figure represents the standard deviation.

4.2 Simultaneous Wind/Rain Retrieval

As we have shown, conventional wind-only retrieval can be adversely affected by moderate to heavy rains at high incidence angles. To compensate for rain-induced backscatter, a simultaneous wind/rain retrieval (SWRR) method for ESCAT is developed in this section.

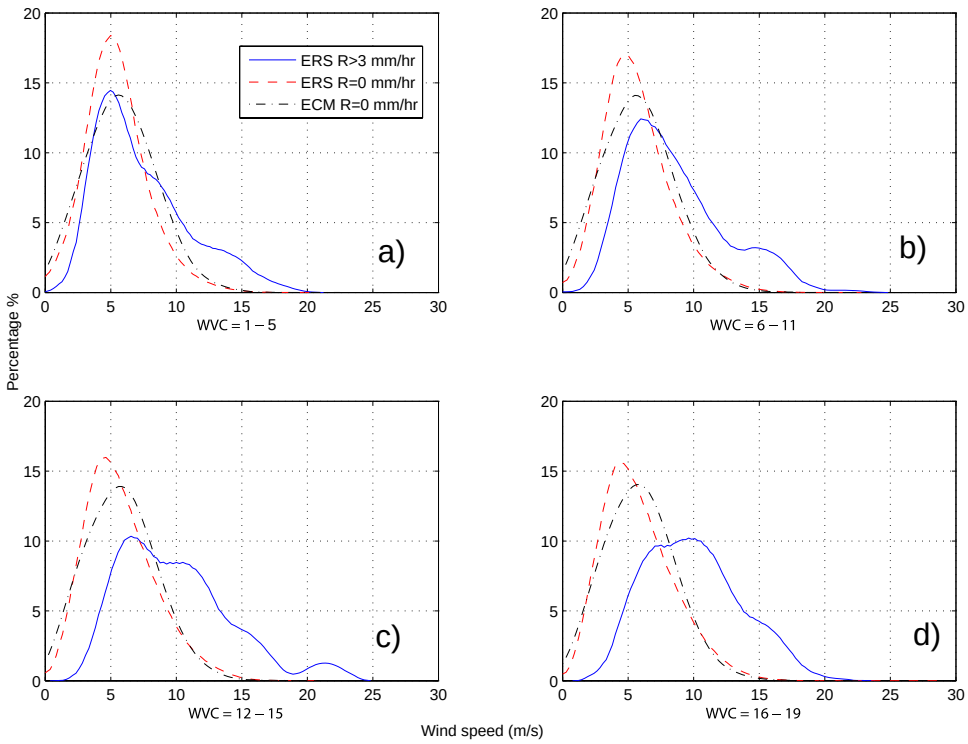

Figure 4.4: Normalized histogram of the wind-only-retrieval selected wind speed ambiguities for rain-free (ERS R=0 mm/hr) and over 3 mm/hr rain rate (ERS $R > 3$ mm/hr) and collocated ECMWF wind directions (ECM R=0 mm/hr) for different WVC bins 1-5 (a), 6-11 (b), 12-15 (c), and 16-19 (d).

4.2.1 Methodology

The SWRR method is based on a simple additive wind/rain backscatter model proposed in [7] [11], which represents the rain-modified measured backscatter σ_m as

$$\sigma_m = \sigma_{wind}\alpha_{atm} + \sigma_{eff} \tag{4.4}$$

where σ_m is the ESCAT-measured σ°, σ_{wind} is the wind-induced surface backscatter, α_{atm} is the two-way rain-induced atmospheric attenuation, and σ_{eff} is the effective rain backscatter due to the attenuated surface perturbation and the rain-induced atmospheric scattering [4] [7] [11] [35]. α_{atm} and σ_{eff} are related to the surface rain rate R in mm/hr by empirically derived linear or quadratic log-log models [11] as shown in Equations (3.15) and (3.19). The coefficients of the power law models are given in Table (3.1) and (3.4). Applying the rain model with the conventional wind

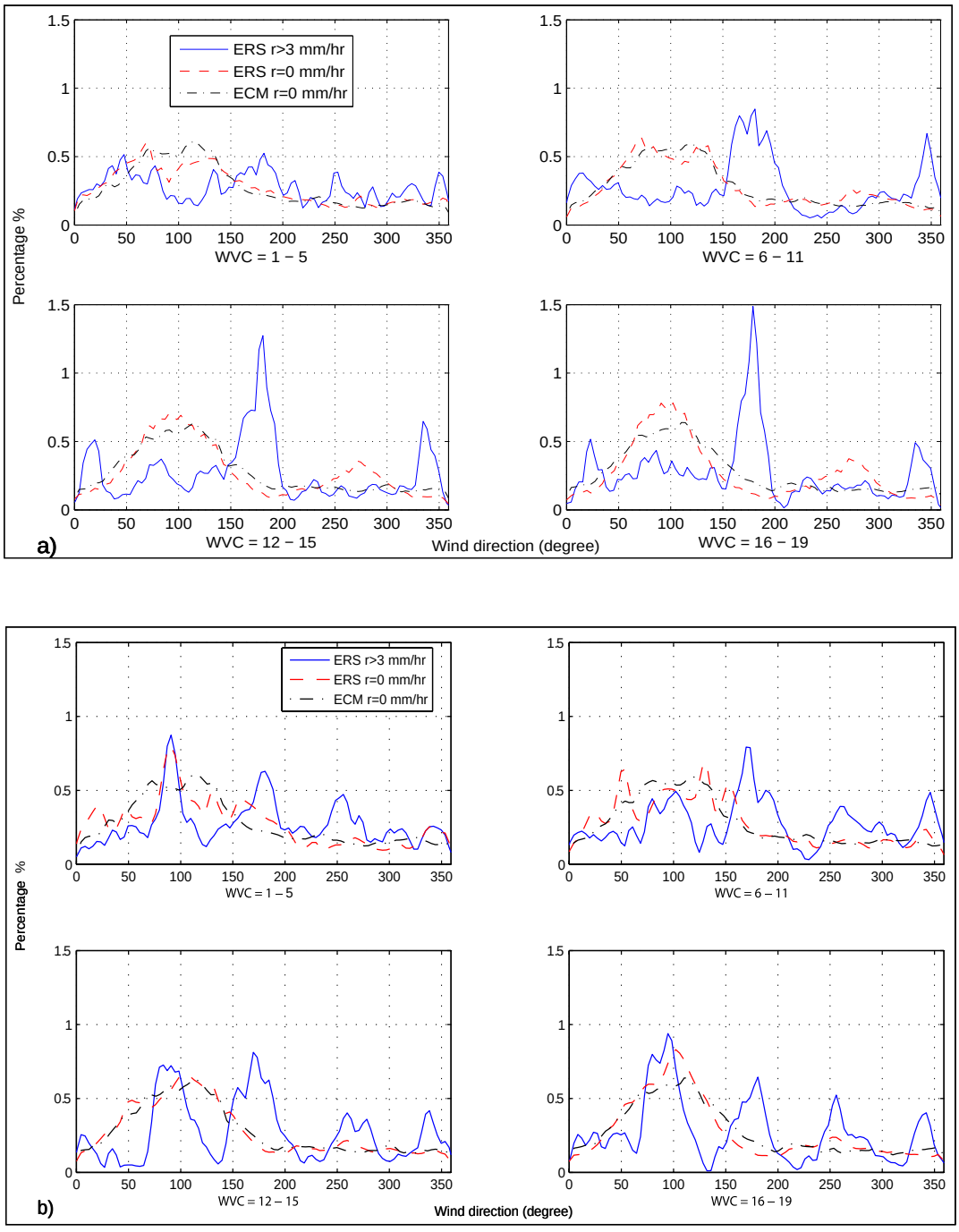

Figure 4.5: Normalized histogram of the wind-only-retrieval selected wind directions (in (a)) and the direction ambiguities closest to the collocated ECMWF wind directions (in (b)) for rain-free (ERS R=0 mm/hr) and over 3 mm/hr rain rate (ERS $R > 3$ mm/hr) and collocated ECMWF wind directions (ECM R=0 mm/hr) for different WVC bins.

GMF function CMOD5, the wind/rain GMF is

$$\sigma^{\circ} = \text{CMOD5}(s, d, \theta, \phi)\alpha_{atm}(R, \theta) + \sigma_{eff}(R, \theta). \tag{4.5}$$

Then, the MLE likelihood function of equation (4.1) is written as

$$\mathbf{MLE}'(z|s, d, R) = \sum_{i=1}^{3} \frac{(\sigma_i^{\circ} - \mathbf{M}'(s, d, \phi_i, \theta_i, R))^2}{(\varsigma_i'(s, d))^2} \tag{4.6}$$

where $\mathbf{M}'$ is the wind/rain GMF in equations. ς' is the variance of the rain-contaminated measurement, which is estimated in the next subsection. Wind velocity and rain rate estimates are retrieved simultaneously by minimizing the new MLE for s, d, and R given the triplet σ° measurements. For simplicity, the normalization method proposed in [18] is not applied in this paper, though the normalization method may further improve the accuracy of SWRR. Similar to the wind-only retrieval method, minimization of the SWRR MLE results in multiple ambiguities with corresponding wind speed, wind direction, and surface rain rates. Here, we use an adjusted median-filter-based method based on the method proposed in [36] to select a final estimate. The adjusted median filter weights each ambiguity by the exponential of its likelihood value. Collocated ECMWF wind fields are used for nudging.

4.2.2 Variance of the Rain-contaminated Measurements

Before deriving the variance model of the rain-contaminated measurements, some assumptions are required. The noise in the measurement is assumed to be white Gaussian noise. The communication noise K_{pc} and wind-only GMF uncertainty K_{pm} are assumed unchanged under raining conditions. K_{pm}, K_{pa} (the uncertainty of α_{atm}), and K_{pe} (the uncertainty of σ_{eff}) are assumed independent. Under these assumptions, the noisy wind/rain backscatter measured by the scatterometer instrument can be

modeled as

$$\begin{aligned}\sigma_{meas}=&[\sigma_{wind}(1+v_1K_{pm})\alpha_{atm}(1+v_2K_{pa})\\&+\sigma_{eff}(1+v_3K_{pe})](1+K_{pc}v_4)\end{aligned}\tag{4.7}$$

where σ_{wind} can be approximately represented by the wind only GMF, $\mathbf{M}$. v_1, v_2, v_3, and v_4 are zero-mean Gaussian random variables. Because K_{pa} is negligible compared with K_{pe} [8], K_{pa} is ignored in the derivation of $Var(\sigma_{meas})$. The variance of the measured σ°, $Var(\sigma_{meas})$, is

$$\begin{aligned}Var(\sigma_{meas})\approx&(1+K_{pc}^2)(\mathbf{M}^2\alpha_{atm}^2K_{pm}^2+\sigma_{eff}^2K_{pe}^2)\\&+K_{pc}^2(\sigma_{eff}+\mathbf{M}\alpha_{atm})^2.\end{aligned}\tag{4.8}$$

K_{pc} is available for each WVC in the ESCAT product, and is about 0.05. K_{pm} is considered insignificant except for low wind speeds [18][37]. The K_{pe} term for ESCAT has never been studied, but is analyzed and estimated in the following section.

4.3 Estimation of K_{pe}

Many factors contribute to K_{pe}, including uncertainty in the rain backscatter model and variability caused by the non-uniform beamfilling (NUBF) effect. The value of K_{pe} can be roughly estimated in the range of $0.38-0.45$ from validation of the wind/rain backscatter model, where the normalized standard deviations due to uncertainty in the model is 1.4 dB and 1.6 dB for $\theta=40^\circ-49^\circ$ and $\theta=49^\circ-57^\circ$ [11], respectively. However, this value of K_{pe} may be overestimated due to the variability of the temporal collocation, the inherent uncertainty of the ECMWF predicted winds, and the errors in the TRMM PR estimated surface rain rates. In this section, we first evaluate the contribution to K_{pe} by the NUBF effect. Then we adopt a practical method to seek an optimal K_{pe} for the wind/rain retrieval process. Finally, the impact of the value of K_{pe} on the wind/rain retrieval process is investigated.

4.3.1 K_{pe} Due to the Beam-filling Effect

The size of a typical rain cell is on the order of 5 km [38], which is relatively small compared with the 50 km 3 dB spatial response function of ESCAT. Hence, the variability due to NUBF is a considerable factor for K_{pe}. To estimate the NUBF-induced variability, we estimate the standard deviation of the normalized error between the model-predicted rain effective backscatter σ_e^m calculated from the antenna-weighted-average TRMM-PR rain rate and the ESCAT-observed effective backscatter σ_e^e. σ_e^e can be approximately estimated by averaging the ESCAT-observed effective backscatter σ_e' at each TRMM PR cell in the ESCAT footprint, σ_e', over the 3 dB spatial response function of ESCAT, i.e.,

$$\sigma_e^e = \frac{\sum_{i=1}^{N} G(i)\sigma_e'(i)}{\sum_{i=1}^{N} G(i)} \tag{4.9}$$

where $G(i)$ is the ESCAT spatial response function gain at the ith PR measurement, and N is the number of PR data points within the ESCAT 3-dB antenna pattern contour.

σ_e' is estimated by projecting the TRMM PR surface rain rate through a rain backscatter model unweighted by the spatial response function of ESCAT. The model has the same form as Equation (4.4) but different coefficients from the weighted rain backscatter model in [11]. To estimate the coefficients of the unweighted model, we estimate σ_e^e for varying values of model coefficients of the unweighted model. Comparing σ_e^e with the corresponding σ_e^m, we choose the model coefficients that yield the lowest root mean-square (RMS) error overall. An estimate of K_{pe} is obtained by taking the standard deviation (**STD**) of the normalized error between σ_e^m and σ_e^e,

$$K_{pe} \cong \mathbf{STD}\left(\frac{\sigma_e^e - \sigma_e^m}{\sigma_e^m}\right) \tag{4.10}$$

for all surface rain rate observations above a rain rate threshold.

The resulting value is $K_{pe} \approx 0.07$ for rain rate ≥ 0.8 mm/hr and $K_{pe} \approx 0.19$ for rain rate < 0.8 mm/hr, showing that the model uncertainty due to the beam filling

effect is more significant for low rain rates than for moderate-to-high rain rates. We note that for relatively large footprints and moderate-to-high rain rates, rain fields often appear relatively uniform. Also, the shape of rain backscatter model function is relatively flat. For these reasons, the model variability due to the beam-filling effect is relatively small for moderate-to-high rain rates.

4.3.2 Seeking Optimal K_{pe} for the Wind Retrieval Process

As mentioned above, many factors contribute to the model uncertainty. Analyzing all of them is beyond the scope of this paper. Here, we adopt a method proposed in [34] to seek the optimal value of K_{pe} for the wind retrieval process. From Equation (4.3), we know that the value of K_{pe} can affect the MLE. Hence, the wind/rain estimation is affected by the value of K_{pe}. The optimal-K_{pe}-seeking method is to find the value of K_{pe} for SWRR that yields the best wind speed estimates using the collocated data set. To find the optimal value of K_{pe}, we perform SWRR for varying values of K_{pe}. RMS wind speed error between SWRR-retrieved wind and ECMWF predicted wind for each K_{pe} are evaluated over the collocated data set.

The wind speed bias between wind-only-retrieved winds with CMOD5 and ECMWF winds is about -0.2 m/s [15], which is compensated for in the computation of the RMS wind speed error. When $K_{pe} = 0.21$, the RMS error is at a minimum for measurements with rain rate > 0 mm/hr; hence, we choose this value for K_{pe}.

To understand the impact of K_{pe} on simultaneous wind/rain retrieval, we illustrate the RMS error of the wind speed retrieval in Fig 4.6. The standard deviation of the RMS wind speed error for various K_{pe} is 0.0191 m/s, showing that the impact of K_{pe} on simultaneous wind/rain retrieval is insignificant.

With an estimated K_{pe}, we have all the parameters for SWRR. To validate and evaluate the performance of SWRR, we use both simulation and real collocated data sets, which are illustrated in the following sections.

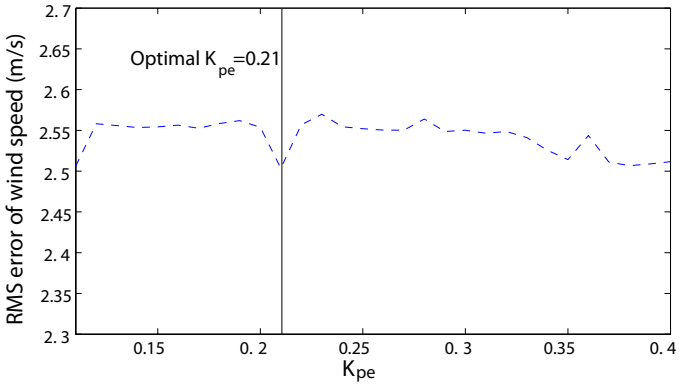

Figure 4.6: RMS error between SWRR-retrieved and ECMWF wind speeds as a function of K_{pe} for rain rate > 0 mm/hr. The optimum value of K_{pe} is indicated.

Table 4.1: Wind speeds, wind directions, and rain rates for simulations.

Wind Speeds (m/s)	4	8	12	16	20	24
Wind Directions (degree)	0	20	40	...	340	
Rain rates (mm/hr)	0	1	3	10	30	

4.4 Simulations

In this section, we evaluate the performance of SWRR under various wind/rain conditions by simulation. To achieve this goal, SWRR and wind-only retrieval are performed using synthetic σ° measurements created by Monte-Carlo simulation under specific wind/rain conditions for WVCs 13, 15, 17, and 19.

4.4.1 Simulation Method

To create simulated σ° measurements, we project the various wind speeds, wind directions, and rain rates through the wind/rain backscatter model in Equation (4) with typical measurement geometries at each ESCAT WVC. Zero-mean Gaussian random noise with the variance given in Equation (10) is added to σ°. The wind speeds, wind directions, and rain rates used for simulations are listed in Table 4.1. For each condition, 500 noise realizations are created for each case. After performing SWRR and wind-only retrieval over the realizations, ambiguities closest to the true wind vectors are selected.

4.4.2 Results and Analysis

To aid in analyzing the results from the simulations, we introduce a parameter, the rain ratio τ [7] [11], to indicate how severely the rain alters the backscatter. The rain ratio shows the average percentage of the rain-induced backscatter relative to the total effective backscatter σ_t,

$$\tau = \frac{1}{k} \sum_{l=1}^{k} \frac{\sigma_e^l}{\sigma_t^l} \tag{4.11}$$

where k is the number of measurements and σ_e is the rain-induced effective backscatter. As in [11], we define three distinct regimes using τ. In regime 1 ($\tau < 0.25$), wind-induced backscatter dominates and rain information cannot be accurately estimated from the measurements. Wind and rain-induced backscatter are on the same order of magnitude in regime 2 ($0.25 \leq \tau \leq 0.75$), and wind and rain information can be simultaneously estimated. In regime 3, rain-induced backscatter dominates the total backscatter ($\tau > 0.75$); hence only rain rate can be accurately retrieved.

To compare the performance of SWRR and wind-only retrieval under varying regimes, we show the mean and standard deviation of the difference between SWRR and wind-only retrieved and true wind speed, $\mathrm{Err}_s = \mathrm{s}_{retrieved} - \mathrm{s}_{true}$, for a typical wind and rain case in each regime for WVCs 13, 15, 17, and 19 in Fig. 4.7. Due to the varying incidence angles at different WVC, the value of τ varies at different WVCs under the same wind and rain conditions. The corresponding true wind speed is 8 m/s, close to the mean wind speed over the ocean, while the true rain rates are 0, 10, and 30 mm/hr, respectively. In regime 1 (left most column), Err_s of both SWRR and wind-only retrieval are close to zero mean, showing that wind speed estimation is almost unbiased for both methods. Err_s of SWRR is slightly noisier than wind-only retrieval and is biased slightly low, especially at cross/along swath directions. This is likely due to the introduction of rain rate to MLE. In regime 2 and 3, the mean of Err_s for SWRR-retrieved wind speeds is close to zero, while Err_s for wind-only retrieval is biased high, especially in regime 3. When rain-induced backscatter highly dominates the backscatter ($\tau > 0.9$), the Err_s for SWRR is slightly biased high, as

shown in regime 3 at WVCs 17 and 19 (right most column). Under the conditions of high rain domination, the standard deviation of Err_s is relatively high, confirming that it is difficult to accurately estimate wind speed in this case.

Furthermore, we compare the mean and standard deviation of SWRR and wind-only error, $\mathrm{Err}_d = \mathrm{d}_{retrieved} - \mathrm{d}_{true}$, for the same conditions in Fig. 4.8. Similar to the wind speed performance, the Err_d for wind-only retrieval and SWRR are close to zero-mean in regime 1, while Err_d for SWRR is somewhat noisier than for wind-only retrieval. In regime 2, the zigzag shape bias in Err_d for wind-only retrieval shows that wind directions are biased toward along-track directions, while the Err_d for SWRR is still close to zero-mean except for along-track directions. In regime 3 where rain dominates, wind-only retrieval is biased significantly toward the along-track direction, while SWRR performs relatively well at WVCs 13 and 15. At WVCs 17 and 19, high domination by rain degrades the wind direction estimates, especially at the along-track direction close to 180°. We examine the performance of SWRR-retrieved rain rate by plotting the mean and standard deviation of the difference of the SWRR-retrieved and the true rain rate, $\mathrm{Err}_r = \mathrm{r}_{retrieved} - \mathrm{r}_{true}$, as a function of wind direction for a typical case in the three regimes for WVCs 13, 15, 17, and 19 in Fig. 4.9. The true rain rate is 10 mm/hr. In regime 1 where wind dominates, SWRR rain estimation performs poorly. Rain rate cannot be accurately retrieved, especially for low incidence angle WVCs 13 and 15 where the backscatter measurements are less sensitive to rain. In regime 2, the retrieved rain rate is close to zero-mean at WVCs 13 and 15 with a slight bias at along-track directions, while Err_r is biased low at WVCs 17 and 19. In regime 3, Err_r is close to zero-mean, and is slightly biased low at WVCs 15, 17, and 19.

Next, we demonstrate the speed performance for SWRR and wind-only retrieval by plotting the mean and standard deviation of Err_s as a function of wind speed under varying rain rate conditions for WVCs 13, 15, 17, and 19 in Fig. 4.11. Significant biases exist for low-to-moderate wind speed retrieved by the wind-only method, while the SWRR retrieved wind speed is close to zero-mean at low incidence angle WVCs 13 and 15. Under heavy rain rate conditions, SWRR slightly overesti-

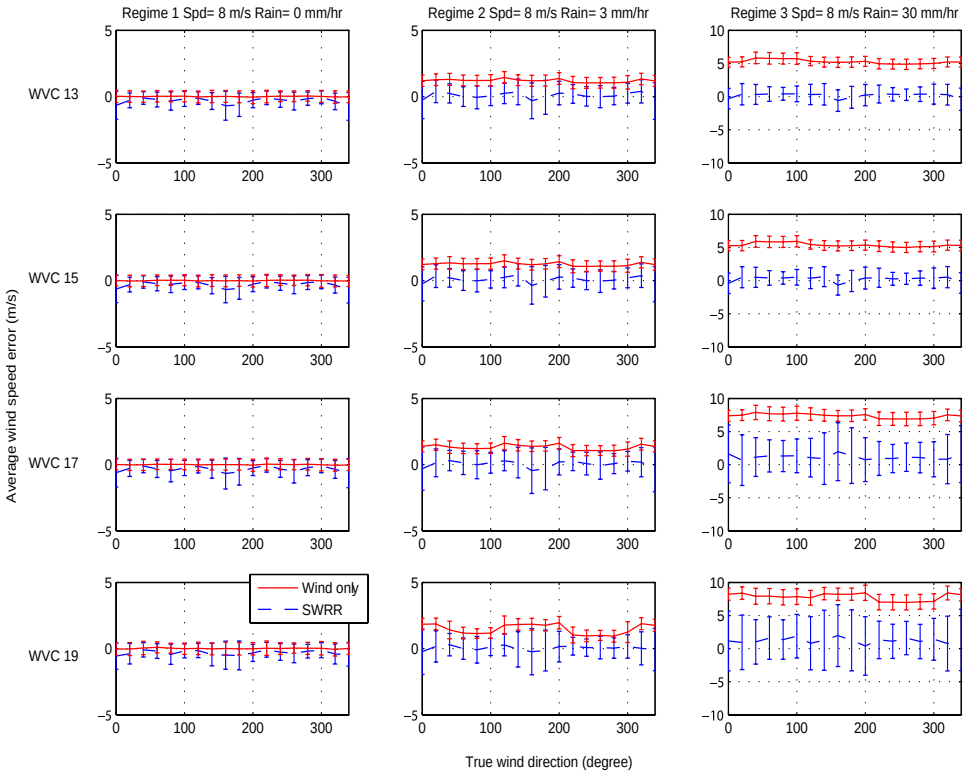

Figure 4.7: Statistics of wind speed error between retrieved and true wind speeds from simulations as a function of true wind direction for three regime cases with true wind speed of 8 m/s for WVCs 13, 15, 17, and 19. In each plot, the results of SWRR is plotted as a dashed line, while the results of wind-only method is plotted as a solid line. Notice the scale differences of the plots. Error bars in the figure represent the standard deviation.

mates the wind speed at high incidence angle WVCs 17 and 19. The small bias in the wind speed estimate causes the rain estimate to be biased low in regime 1 and regime 2, which is shown in Fig. 10 by plotting the normalized mean rain rate error as a function of rain ratio τ. The bias in the rain estimate can be corrected by adjusting the wind/rain backscatter model coefficients in the wind retrieval.

4.5 Validation

We next compare SWRR and wind-only retrieval using actual ESCAT measurements. Wind vectors retrieved from the two methods are validated using collocated ECMWF wind fields. Figures 4.12(a) and 4.12(b) show scatter density plots of

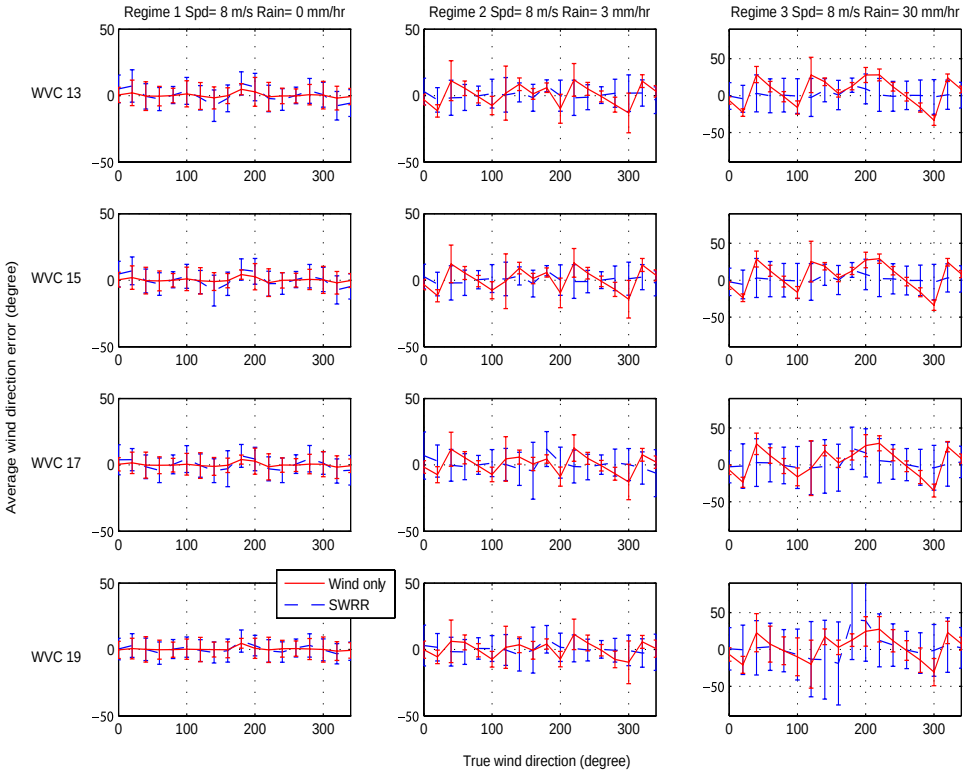

Figure 4.8: Statistics of wind direction error between retrieved and true wind directions from simulations as a function of true wind direction for three regime cases with true wind speed of 8 m/s for WVCs 13, 15, 17, and 19. In each plot, the results of SWRR is plotted in blue, while the results of wind-only method is plotted as a red dashed line. Notice the scale differences of the plots. Error bars in the figure represent the standard deviation.

retrieved wind speed (wind-only and SWRR) and ECMWF wind speed for different rain rate (R) bins. In each plot, non-parametric fit between the retrieved and the ECMWF wind speeds is plotted. When $R < 0.8$ mm/hr, the performance of the two methods is similar. The RMS of the SWRR retrieved wind speed is slightly larger than the wind-only retrieval, showing that the wind speed estimates of SWRR are somewhat noisier than wind-only retrieval. When $R \geq 0.8$ mm/hr, the wind-only retrieved wind speed is biased high, while the SWRR-retrieved wind speed is close to unbiased. When $R \geq 10$ mm/hr, wind speed of wind-only retrieval is significantly biased high and has larger RMS than SWRR. Thus SWRR provides more accurate wind estimates than wind-only retrieval when significant rain is present.

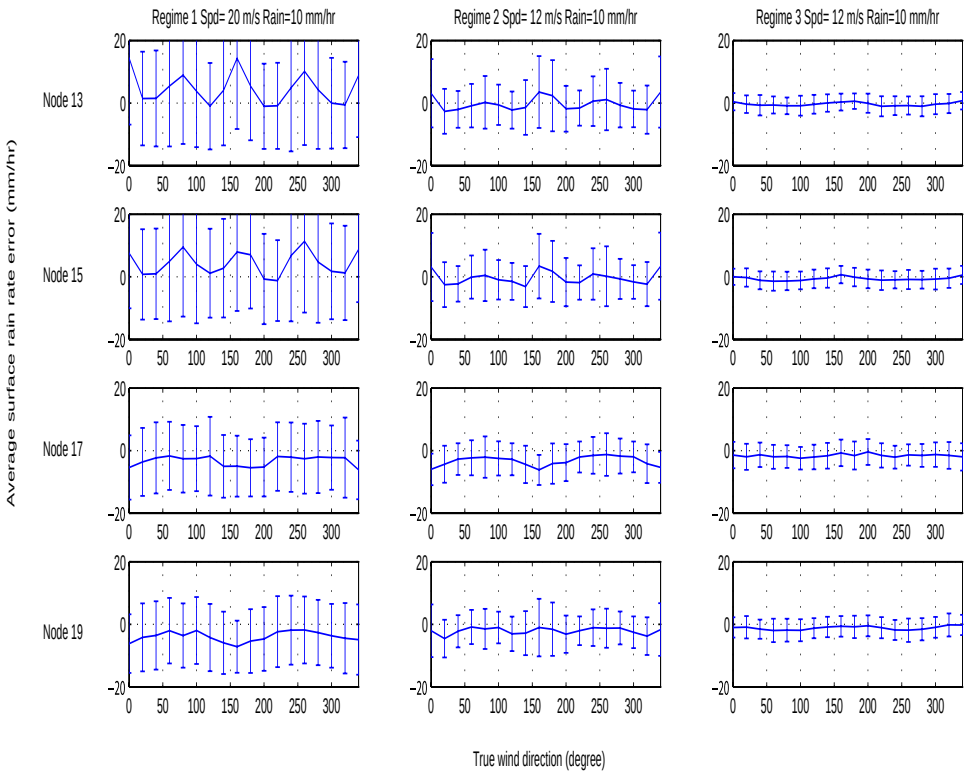

Figure 4.9: Statistics of rain rate error between retrieved and true rain rates from simulations as a function of true wind direction for three regime cases with true surface rain rate of 10 mm/hr for WVCs 13, 15, 17, and 19. The line represents the mean error while the error bar represents the standard deviation.

To demonstrate a compact comparison of the wind direction retrieval performance of wind-only retrieval and SWRR, scatter density plots of the retrieved wind direction (wind-only retrieval and SWRR) and ECMWF predicted wind direction for varying R bins (the same as in Figs. 4.12(a) and 4.12(b)) are presented in Figs. 4.13(a) and 4.13(b). Similar to the wind speed performance, the performance of wind-only retrieval and SWRR is close for $R < 0.8$ mm/hr, while the SWRR retrieved wind direction is somewhat noisier. When $R \geq 0.8$ mm/hr, the selected wind direction in wind-only retrieval is biased to along-track directions. When $R \geq 10$ mm/hr, the wind direction of the wind-only retrieval is significantly biased to along-track directions and has larger RMS than SWRR. For $R \geq 10$, SWRR retrieved wind direction is close to unbiased but is noisy.

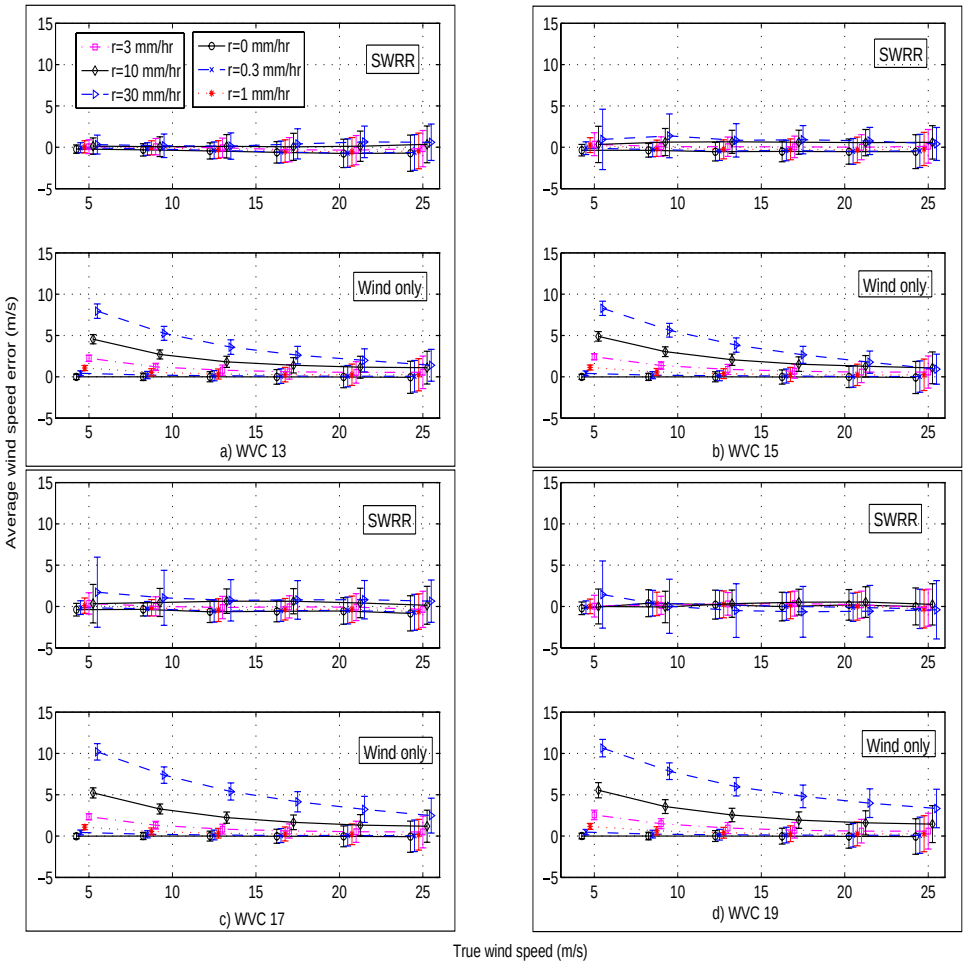

Figure 4.10: Mean (lines) and standard deviation (error bars) of wind speed error between retrieved (SWRR and wind-only) and true wind speed from simulations as a function of true wind speed for various rain cases at WVCs 13 (a), 15 (b), 17 (c), and 19 (d). The upper panel shows the results of SWRR while the lower panel shows the wind-only results.

To validate the surface rain rates retrieved from SWRR, we show a scatter density plot of SWRR retrieved and TRMM PR surface rain rates collocated within ± 15 minutes in Fig. 4.14(a). Because the plot is in log-log space, zero rain rates in either of the SWRR or TRMM PR datasets are not displayed. Of the rain rates that are zero in either of the two datasets, over 95% have relatively small rain rates ($\leq$ 3 mm/hr) in the other dataset. The SWRR and TRMM PR estimated rain rates have a relatively high correlation, although SWRR rain rates have considerable scatter compared with TRMM PR rain rates. SWRR rain rate is biased high for low

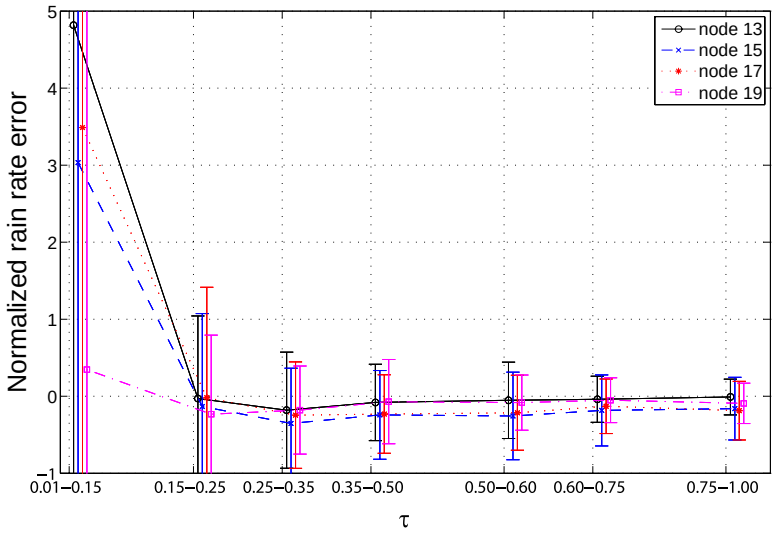

Figure 4.11: Mean (lines) and standard deviation (error bars) of normalized rain error between retrieved and true wind speed from simulations as a function of value of τ at WVCs 13, 15, 17, and 19.

rain rates (approximately $\leq$ 0.8 mm/hr) and biased low for moderate to high rain rates, which is consistent with results of the above simulation. Since the temporal variability of rain events can significantly contribute to the variability between SWRR and TRMM PR derived rain rates, we examine the relationship between the two rain rates within $\pm$2 minutes in Fig. 4.14(b). Here, the SWRR retrieved rain rate is highly correlated with TRMM PR rain rates with a correlation coefficient of 0.89 and $RMS = 2.024$, demonstrating the relatively high accuracy of SWRR retrieved rain. In addition to a scatter-plot between the two rain rates, a histogram of rain rates can be used as a statistical comparison method to validate SWRR-retrieved rain. Fig. 4.14(c) shows histograms of the collocated rain rates estimated by both SWRR (solid line) and TRMM PR (dashed line), where the histograms of the two rain rates match relatively well for moderate to high rain rates, and the curve is biased low for low rain rates.

Through validation, SWRR is shown to significantly improve wind estimates in regimes where the wind and rain induced backscatter is on the same order. When rain induced backscatter dominates the total backscatter, SWRR wind estimates are noisy but almost unbiased. SWRR-retrieved rain rates have relatively high accuracy

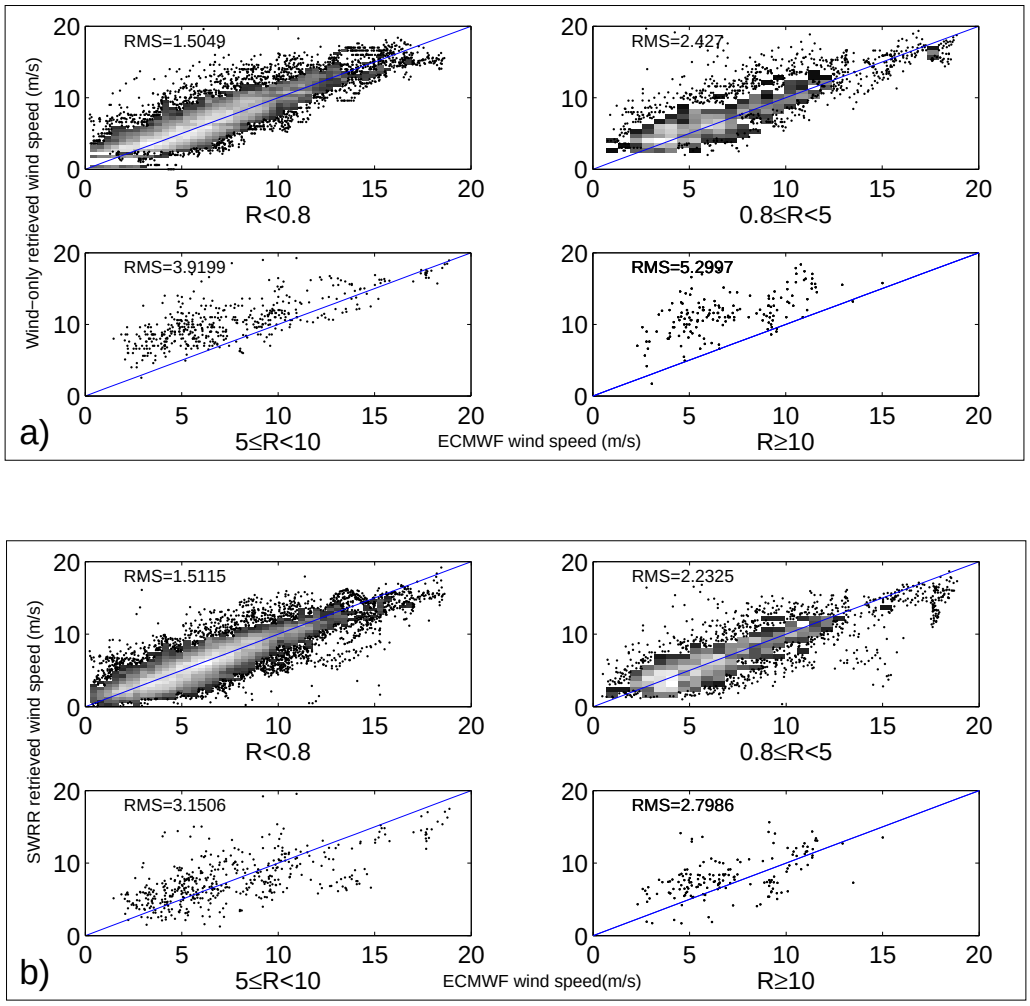

Figure 4.12: Scatter density plot of wind-only and SWRR-retrieved wind speeds and collocated ECMWF wind speeds for various rain rate (R in mm/hr) bins. Non-parametric fits are plotted as a dashed line. (a) Wind-only-retrieved wind speeds versus collocated ECMWF wind speeds for several rain ranges. Bias develops when R is over 5 mm/hr. (b) SWRR-retrieved wind speeds versus collocated ECMWF wind speeds for the same rain ranges. No obvious bias for all R ranges.

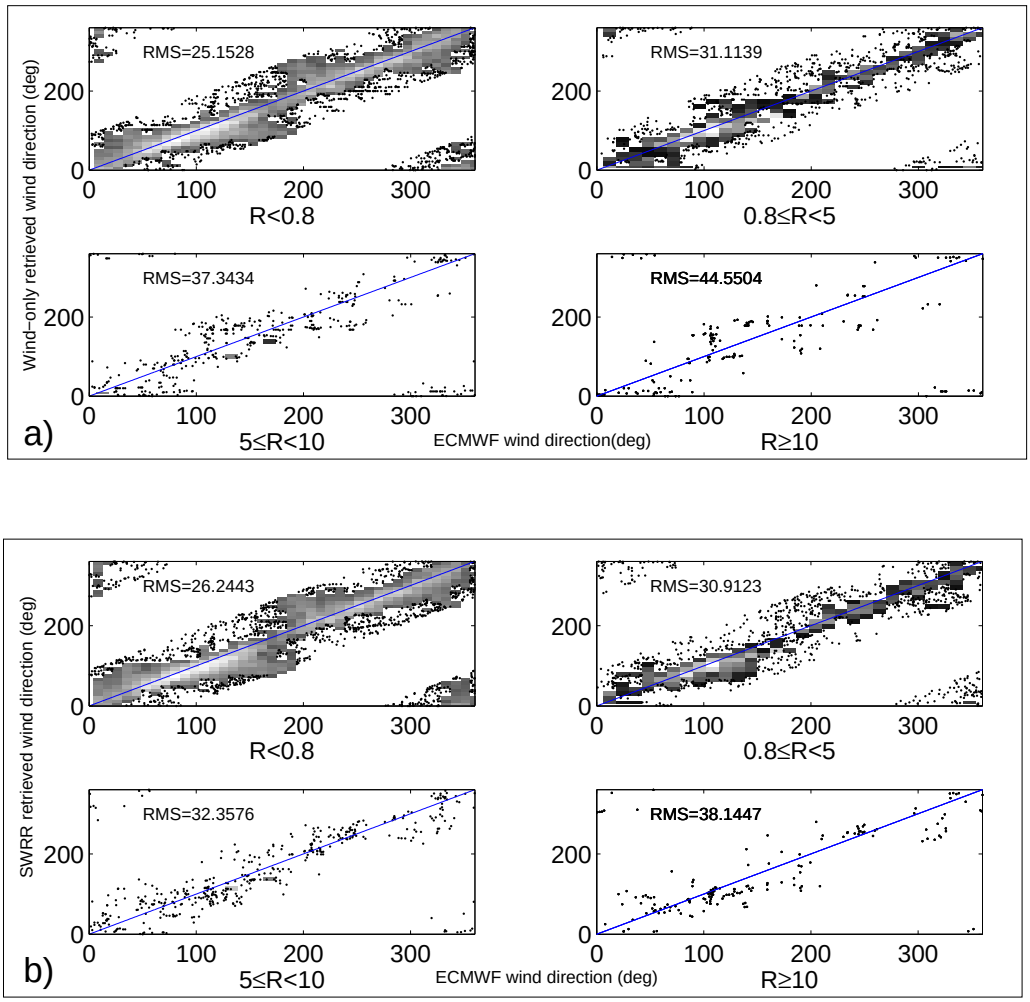

Figure 4.13: Scatter density plot of wind-only and SWRR retrieved wind directions and collocated ECMWF wind directions for various rain rate (R in mm/hr) bins. (a) Wind-only-retrieved wind direction versus collocated ECMWF wind direction. Bias along the along-track direction develops when R is over 5 mm/hr. (b) SWRR-retrieved wind direction versus collocated ECMWF wind direction. No obvious bias exists for all R ranges.

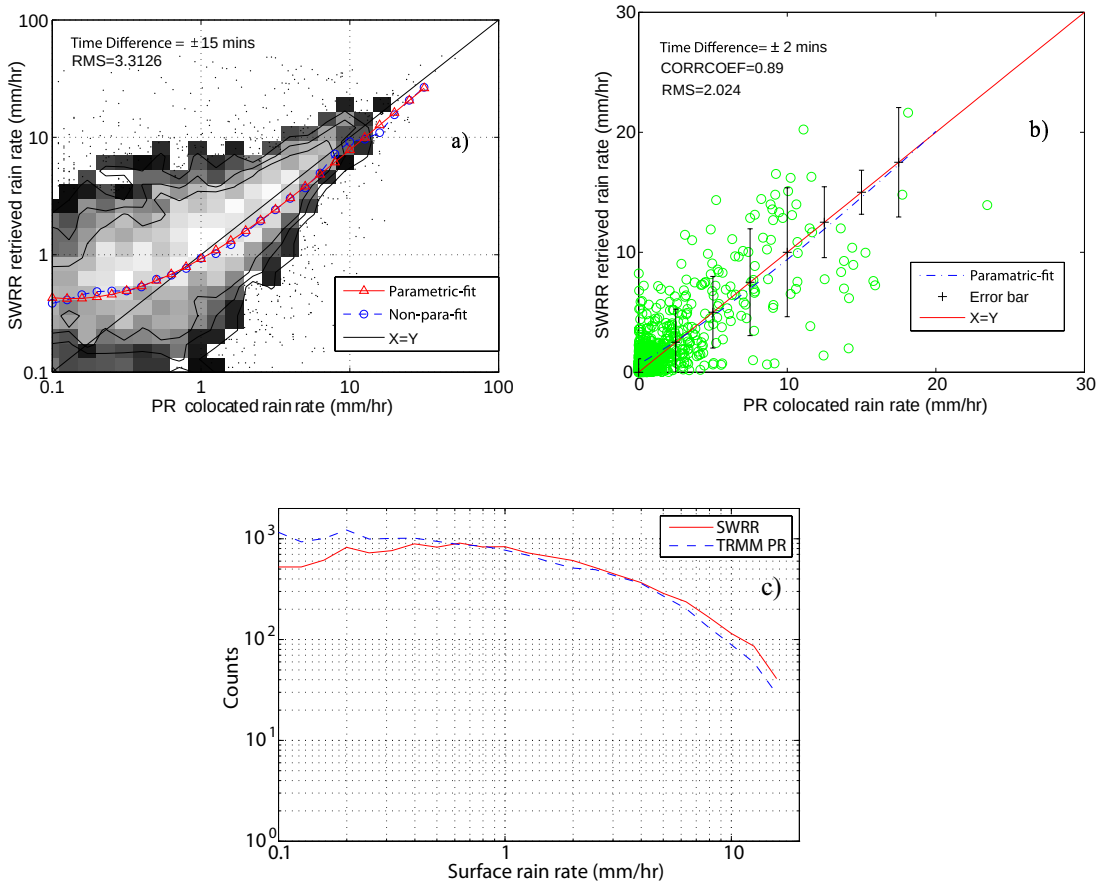

Figure 4.14: Scatter density plot of SWRR rain rates versus TRMM PR antenna weighted rain rates within ±15 minutes in log-log space in (a) and within ±2 minutes in normal space in (b). Nonparametric fit and best quadratic fit to TRMM PR rain rate in log-log space in (a) and best quadratic fit in normal space in (b) are also shown. Error bars represent the standard deviation. Histograms of SWRR and TRMM PR rain rates are shown in (c).

for moderate to high rain rates. SWRR retrieved rain rates are somewhat biased but can be corrected. Unfortunately, since ESCAT is not specially designed for rain detection, introduction of rain rate into wind retrieval makes SWRR wind estimates noisier than wind-only retrieval and rain rate estimates are inaccurate in regime where wind-induced backscatter dominates the total backscatter. Since the wind-only retrieval method performs well in regime 1, SWRR is less useful here. Furthermore, due to the geometry of ESCAT and limitations of MLE, SWRR does not perform

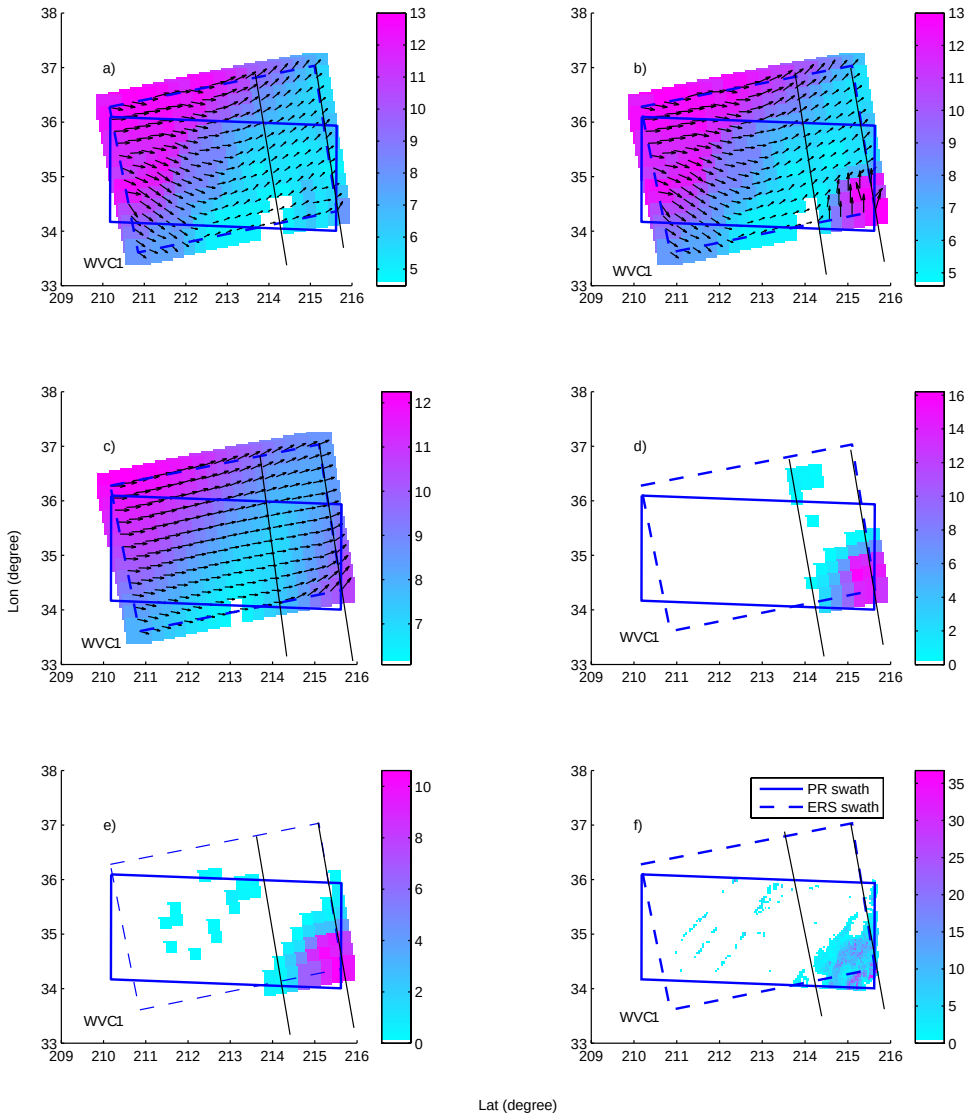

Figure 4.15: An example of a SWRR retrieved wind/rain field. (a)-(c) show SWRR-retrieved, wind-only-retrieved, and ECMWF wind vectors with corresponding wind speeds plotted as background. (d)-(f) show SWRR-retrieved rain, TRMM PR antenna-weighted rain, and TRMM PR retrieved rain. The TRMM PR swath is outlined by a blue solid line, while the ESCAT swath is outlined by a dashed line. WVCs (13-19) where SWRR is performed is outlined by two black solid lines.

well at along-track wind directions, where SWRR often misidentifies wind and rain. Thus, it is most useful to implement SWRR only in raining areas and use wind-only retrieval in rain-free areas. SWRR-retrieved wind/rain can be used when rain ratio τ is greater than a specific threshold. MLE-based QC methods [18] can be used for rain thresholding to improve the accuracy of wind/rain estimates.

4.6 Case Study of SWRR Retrieved Wind/Rain Fields

To demonstrate the performance of SWRR under different circumstances, we examine two typical cases of SWRR-retrieved wind/rain fields. The first case shows a storm over the Pacific ocean at about latitude 35° and longitude 215° at UTC 08:13:47 on 12/25/2000. We compare the SWRR-retrieved wind/rain, wind-only retrieved wind, ECMWF winds, and collocated TRMM PR rain rates in Fig. 4.15.

In (b), the wind-only wind fields exhibit many rain-contaminated features. In the heavy rain area at the right bottom, dramatic wind speed inconsistency and along-track wind directions are present, which is an indicator of severe rain contamination. In (a), SWRR-retrieved wind vectors in the raining area are more consistent with nearby rain-free WVCs. SWRR-retrieved wind vectors also agree with ECMWF wind fields in (c) much better than the wind-only-retrieved wind vectors, showing that SWRR significantly improve the wind estimates in this case. Comparing the rain fields in (d) and (e), we find similar spatial rain patterns in the SWRR-retrieved and TRMM PR antenna-weighted rain. While SWRR somewhat overestimates rain rates in this case, SWRR-retrieved rain rate is highly correlated with the TRMM PR antenna-weighted rain rates.

4.7 Conclusion

Using collocated TRMM PR, ESCAT on ERS 1/2, and ECMWF data, rain effects on ESCAT wind-only retrieval are evaluated and analyzed. Wind speed retrieved by wind-only retrieval is biased high due to the rain-induced backscatter. Rain contamination causes the wind direction estimates to be biased toward the along-track directions under heavy rain conditions, no matter what the true wind

direction. Rain effects on the wind-only retrieval varies with incidence angles. The higher the incidence angle, the more significant the rain impact is on the wind-only retrieval.

To compensate for rain-induced backscatter, we develop a simultaneous wind/rain retrieval method for a C-band scatterometer for incidence angle $> 40^\circ$ based on a wind/rain backscatter model. Through simulation and validation with collocated ESCAT, TRMM PR, and ECMWF data, we find that SWRR can significantly improve wind speed and wind direction estimates in regimes 2 and 3 where rain and wind-induced backscatter are on the same order or rain dominates the total backscatter. In addition, SWRR can retrieve rain rate from ESCAT measurements. The rain estimates have relatively high accuracy in regimes 2 and 3. In regime 1 where wind-induced backscatter dominates the total backscatter, the accuracy of SWRR-retrieved rain rates is degraded and spurious rain rates may be derived. Due to limitation's in the MLE, SWRR does not perform well when the wind direction aligns along-track directions. In regime 1 (which includes most high wind cases), the performance of SWRR is close to that of wind-only retrieval, though it is somewhat noisier due to introduction of a new parameter (the rain) to the retrieval. Therefore, SWRR wind/rain should be used only when the rain ratio τ is over a specific threshold.

Although for ESCAT only about 1.5% of all the collocated measurements are affected by significant rain [11], SWRR can enable accurate wind retrieval of a high percentage of rain-contaminated measurements that would otherwise not be usable. Since ASCAT on MetOP is expected to be more sensitive to rain due to its higher incidence angle, SWRR can also benefit ASCAT wind retrieval.

Chapter 5

RADARSAT ScanSAR Wind Retrieval and Rain Effects on ScanSAR Measurements Under Hurricane Conditions

5.1 Introduction

Synthetic aperture radar (SAR) measurements have been conventionally used to study coastal processes, currents, and sea ice with its high spatial resolution and large spatial coverage. Recent studies confirm that SAR measurements can be used in the retrieval of the near-ocean surface winds at ultra high resolution [39]. Similar to scatterometry, the normalized radar cross section (σ°) measured by SAR over the ocean is mainly from wind-driven gravity-capillary waves (Bragg waves). Since SAR has only one measurement for each geographic location, wind speed and direction can not be simultaneously retrieved by direct inversion of the GMF, which is the general method of the scatterometry. The wind direction can be estimated by measuring the orientation of the wind-induced streaks visible in most SAR images [40] [39] [41], or obtained from additional information such as numerical wind prediction. For SAR wind speed retrieval, there are two main methods. One of them estimates wind speed from the spectral width of the image spectrum in azimuth direction. The other one estimates wind speed by inversion of the GMF from the measured σ°, which is a function of the incidence angle, azimuth angle, and wind direction.

Compared with other space-borne instruments, SAR can provide wind estimates at finer resolution, as fine as several hundred meters, which is useful to study the micro-scale weather events. Most of current SAR instruments used for wind retrieval, such as ENVISAT and RADARSAT, operate at C-band. The Canadian satellite RADARSAT-1 works at 5.3 GHz in HH polarization. The scanning SAR (ScanSAR) wide A (SWA) mode of RADARSAT-1 provides coverage of a 500km

nominal ground swath at incidence angles between 20 and 49 degrees, with a spatial resolution of 100 m [42].

Because ScanSAR SWA's resolution is insufficient to implement the spectrum method, the wind speed must be estimated by inversion of GMF. Unfortunately there is no well-validated GMF model for HH polarization at C-band. Our general approach to obtain a HH polarization GMF is to adjust the C-band VV polarization GMF (CMOD) using a polarization ratio p. While several C-band polarization ratio models have been proposed, none has been well verified in hurricane conditions.

Although C-band backscatter has been believed to be little affected by rain, rain cells are often observed on C-band SAR images over the ocean [9] [43]. Rain-induced backscatter is from two processes. One is from atmospheric attenuation and scattering by falling rain drops, which are insignificant for C-band signal. The other one is from rain -induced surface scattering on the ocean surface. Raindrops striking the water and downdraft created by rain cells modify the roughness of the ocean surface; and hence the surface backscatter. In the past, several investigations have been performed to analyze SAR signatures of rain cells over the ocean. Melshimer et al. analyzed SAR signatures of rain cells over the ocean using C- and X-band SAR data, showing that rain generally damp the surface backscatter at low incidence angles and enhance the backscatter at high incidence angles [9]. Nie and Long [11] found that rain surface backscatter can dominate the total backscatter from the ocean surface acquired by C-band radar in moderate to heavy rains by studying the rain effects on ESCAT scatterometer measurements. However, quantitative study of rain effects on SAR measurements has rarely been studied; hence it is necessary to analyze it.

In this study, we analyze several important topics on SAR wind retrieval and rain effects in a hurricane. First, we develop a "recalibration" model for RADARSAT-1 ScanSAR SWA data and demonstrate that relatively reliable estimates of wind speed can be obtained in hurricanes using SAR measurements. Second, complicated rain effects on ScanSAR SWA data are quantitatively evaluated using collocated shore-

based NEXRAD weather radar data. To achieve the above goals, we selected the hurricane Katrina (August 2005 in the Atlantic ocean) as a test case.

In the next section, details of the data set used in the study are described. In Section 5.3, the principles of SAR wind retrieval are illustrated and a recalibration model is proposed for RADARSCAT-1 ScanSAR SWA data. The wind retrieval results are analyzed and validated in Section 5.4. In the following section, rain effects on C-band SAR measurements over the ocean are explained and a backscatter model is proposed to model the rain effects. In Section 5.6, the rain effects are evaluated using the collocated data sets. Conclusions are presented in the final section.

5.2 Data

Hurricane Katrina formed as Tropical Depression Twelve over the southeastern Bahamas on August 23, 2005. Katrina attained Category 5 status on the morning of August 28 and reached its peak strength at 1:00 p.m. that day. Approximately mid-night of August 28, both RADARSAT-1 and SeaWinds on QuikSCAT flew over Katrina with a time difference of several minutes, providing a good collocation of C- and Ku-band measurements over ocean in a hurricane. During the same period, shore-based NEXRAD and air-borne NOAA WP-3D radar also covered the Katrina from different locations, acquiring 3 dimensional rain rates for the study. In this section, these data sets are described. In Fig. 5.1, we show the path of the hurricane Katrina, the outlines of the RADARSAT-1 ScanSAR SWA data and SeaWinds measurements, the locations of NEXRAD weather radar stations and the moving path of NOAA WP-3D airplane.

5.2.1 RADARSAT-1 ScanSAR SWA Data

Two 510 km $\times$ 510 km calibrated RADARSAT-1 ScanSAR SWA images were acquired over the ocean around New Orleans at 23:49:05 and 23:50:50, on 28 August, 2005, during the period of Hurricane Katrina. These are the sources of the SAR measurements used in this study to retrieve the near-surface vector winds over the

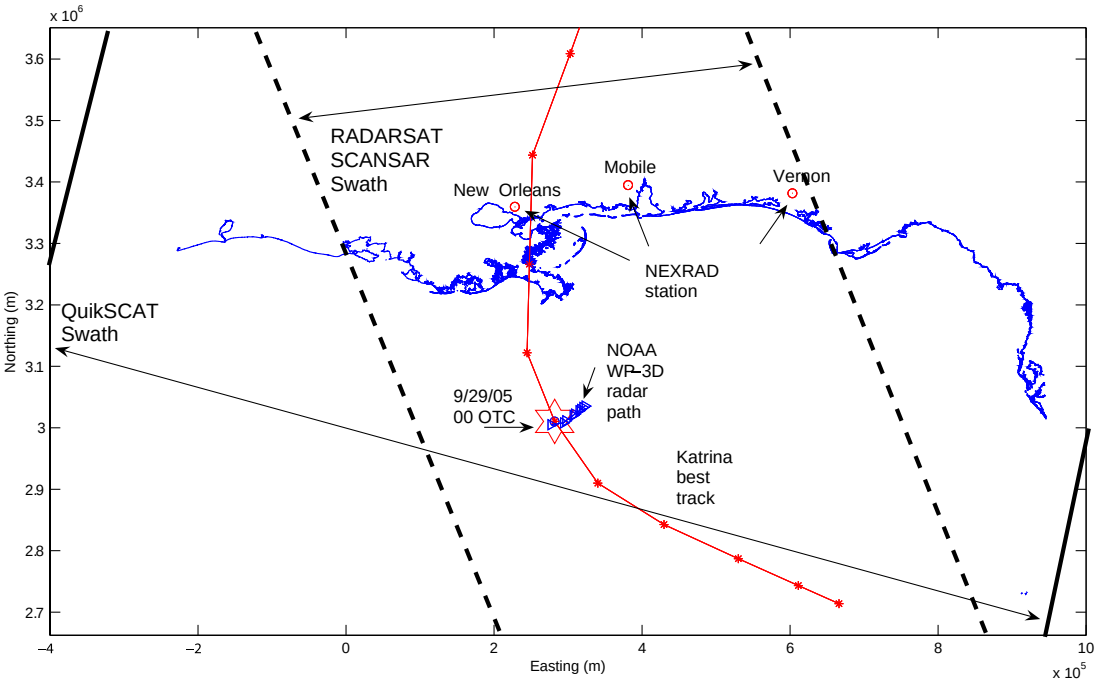

Figure 5.1: Hurricane Katrina best track as determined by the Hurricane Research Division, RADARSAT-1 ScanSAR SWA orbit, Seawinds on QuickSCAT orbit, and the path of the NOAA WP-3D airplane. Three NEXRAD weather radar stations are plotted as red circles. The stars and numbers indicate Katrina locations.

ocean. At the time of observation, the hurricane was a category 5 hurricane with a fully developed eye.

RADARSAT-1 was launched in 1994 for environmental monitoring. The satellite operates on a sun synchronous dawn-dusk orbit at an nominal altitude of 793 to 821 km [42]. Among the different working modes of RADARSAT-1, the ScanSAR wide mode A (SWA) allows imaging of the widest swath of about 500 km, which is ideal for monitoring hurricanes. SWA has a range of incidence angles between 20 to 49 degrees. To create an SWA product, RADARSAT combines four beams (W1, W2, W3, and S7) during data collection, with each beam scanned sequentially. The image processed by the Alaska Satellite Facility (ASF) is 510 km $\times$ 510 km with a pixel spacing of 50 m. The range resolution of the four beams varies from 73.3 m to 162.7 m, while the azimuth resolution varies from 93.1 m to 117.5 m. The raw ScanSAR SWA data was processed by the ASF into calibrated images. However, the radiometric calibration of ScanSAR SWA images is very difficult due to many limitations.

Because of incorrect radiometric compensation for the azimuth antenna pattern, non-zero yaw steering, and inaccurate center Doppler frequency, scalloping between the bands may occur in some areas. Furthermore, saturation of the analog to digital converter (ADC) leads to an underestimation of σ° [10]. Beam overlap regions can occur due to incorrect radiometric compensation for the range antenna pattern and roll angle ambiguity. It is also noted that the calibration at ASF is mainly "tuned" to high latitude areas, which may result in degraded calibration for low latitude areas. The accuracy of the ASF-calibrated SWA images has not been well studied. In [44], the relative radiometric accuracy for SWA is estimated to be about 0.47dB. The geographic location accuracy of the ScanSAR SWA images is still not available, though the overall relative location error for a similar product, ScanSAR SWB, is about 135 m.

To retrieve vector winds, the parameters needed for wind retrieval process are estimated from the SAR image. The SAR images are projected to the Earth's surface using the Universal Transverse Mercator coordinate system. The incidence angle for each image pixel is calculated from ScanSAR SWA data using a method proposed by Shepherd in [45]. Because the format of ASF processed ScanSAR SWA data is not the same as CDPF products, the normalized radar cross section σ° is calculated from the digital number (DN) of each pixel using

$$\sigma^\circ = 10 \log_{10}[(DN_j^2 + A3)/A2_j] \quad \text{dB} \tag{5.1}$$

where $A2_j$ is the scaling gain value for the jth pixel, and $A3$ is the fixed offset to compensate for the noise floor. Since information is unavailable to calculate a nominal noise vector for ScanSAR SWA product, $A3$ is set to 0 for all ASF calibrated ScanSAR SWA products.

In the two ScanSAR images, rain bands exist next to the eyewall of Katrina and several long rain cell clusters span a wide range of incidence angles, providing a good data source to study rain effects on measurements at various incidence angles.

5.2.2 NOAA Hurricane Research Division H*wind Data

To validate the SAR retrieved wind fields and calculate the wind-induced backscatter, coincident H*wind surface wind fields [46] are used in the study. The H*wind Surface Wind Analysis System is an experimental high resolution hurricane research tool developed by the Hurricane Research Division (HRD) at the National Oceanic and Atmospheric Administration (NOAA). The H*wind system assimilates and synthesizes disparate observations into a consistent wind field. The H*wind system uses all available surface weather observations including NOAA P3 and G4 research aircraft measured data, retrieved winds from SSM/I radiometer, ERS and QuikSCAT scatterometers, and TRMM radiometer, and GOES cloud drift winds to predict surface wind fields. All data are processed to conform to a common framework for 10 m height, the same exposure, and the same averaging period using accepted methods from micrometeorology and wind engineering [47]. The analysis provides the maximum sustained 1-minute wind speed. Due to the limited coverage of the observations and the smoothing effect of the analysis process, fine scale details of the ocean surface winds are filtered out. The spatial resolution of H*wind estimates is 0.0542 degree in latitude and longitude, while the time resolution is 3 hours. The H*wind-predicted wind fields are trilinearly interpolated in space and time to RADARSAT-1 ScanSAR SWA data times and locations.

5.2.3 NEXRAD Doppler Weather Radar Data

Since the center of Hurricane Katrina is close to coastal line at the time when the RADARSAT-1 data was acquired, collocated NEXRAD-derived three-dimensional rain rates are used to evaluate the effects of rain on the SAR measurements. NEXRAD measures radar reflectivity and Doppler shift by employing a rotating 8.5-m paraboloid antenna with a output power of 750kW. NEXRAD radar operates at S-band (2.7-3.0 GHz). During storm events, NEXRAD uses a pre-programmed set of scanning elevations, Volume Coverage Pattern (VCP) 11, to acquire data. The radar successively scans 360° in azimuth angle in 1° increments and from 0.5° to 6.2° in 0.95° increments in elevation angle. Additional circular scans at a 7.5°, 8.7°, 10.0°,

12.0°, 14.0°, 16.7°, and 19.5° elevation angle are performed. The rotating speed of NEXRAD is about 3.4 rpm; hence, a volume scan is be completed in approximately 5 minutes.

In general, rain rates are derived from NEXRAD measurements of reflectivity Z by inversion of the reflectivity to rain rate (Z-R) relationship,

$$Z = aR^b \tag{5.2}$$

where constants a and b are dependent on drop-size distribution. The optimal Z-R constants determined by Jorgensen and Willis in mature hurricanes is $a = 300$ and $b = 1.35$. The NEXRAD Z measurements are estimated at 1 km resolution over the range of 1-460 km from the radar. NEXRAD level II data provided by the NOAA Radar Operations Center contains Z measurements.

To collocate the NEXRAD rain measurements with RADARSAT-1 ScanSAR SWA data, the NEXRAD measurements are converted from Plan Position Indicator (PPI) to Constant Altitude Plan Position Indicator (CAPPI) with 1 km $\times$ 1 km resolution in the horizontal and 1 km resolution in the vertical. Interpolation is used to project the measurements from PPI to CAPPI. The ray path is computed using the "four-thirds earth radius model" [19]. The NEXRAD rain rates are then projected to UTM coordinates.

As shown in Fig. 5.1, NEXRAD data from stations at New Orleans (LIX), Mobile (MOB), and Tallahassee (EVX and TLH) are used. In the overlapping area of two radars, we select the rain estimates from the nearest station. To ensure the quality of the rain estimates, we limit the maximum range of NEXRAD radar data subjectively to a 200 km radius.

5.3 SAR Wind Retrieval

As mentioned in Section 1, the wind direction can be derived from the orientation of wind-induced streaks, such as boundary layer rolls in the atmosphere, which are visible in many SAR images. In such images the spectrum method can be

implemented to estimate the wind direction. However, this method has not proved applicable to these RADARSAT-1 ScanSAR images, due to the inadequate spatial resolution of the images [10]. Therefore, additional information such as numerical predicted wind fields must be used to estimate of the wind direction. For a hurricane, the wind direction can also be estimated by combining the SAR images with hurricane dynamic models. In this study, the collocated H*wind direction field is used as the wind direction for SAR wind retrieval.

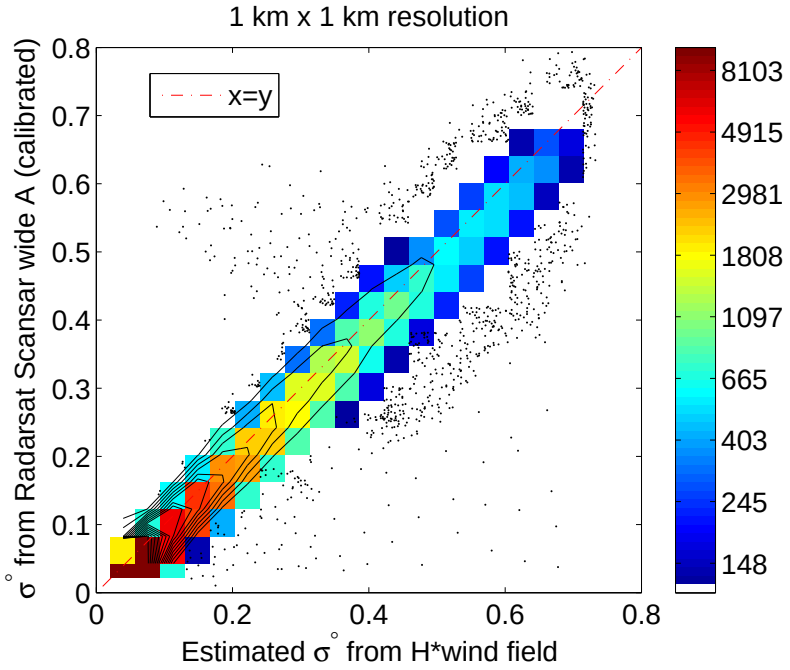

Figure 5.2: Scatter density plot of the σ° from re-calibrated SAR image A and σ° calculated from collocated H*wind. Both σ° axes are in normal space. The resolution of σ° is 1 km $\times$ 1 km.

Knowing the wind direction, the wind speed can be derived from the σ° by inversion of the GMF with input of the incidence angle θ, and the azimuth angle, and the wind directions. Lacking a well-validated GMF for C-band HH polarization, the GMF for C-band VV polarization is modified using the C-band polarization ratio to

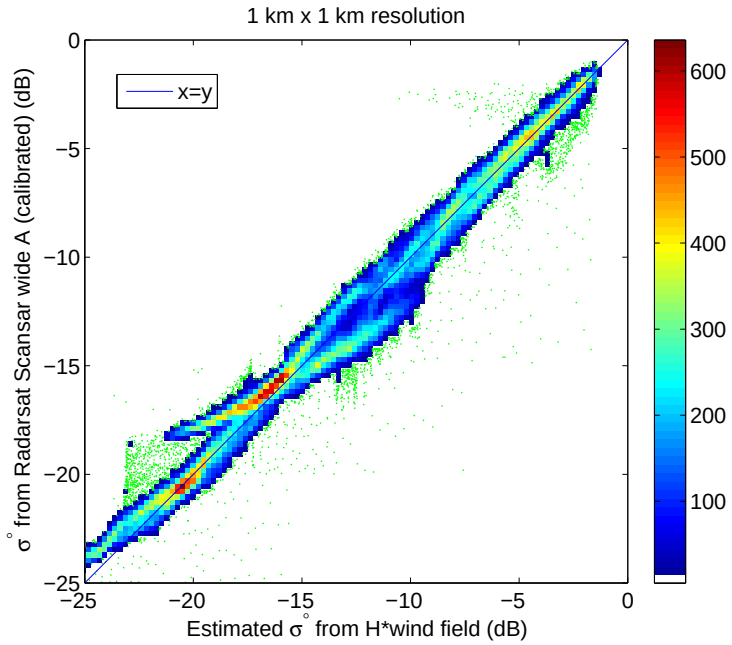

Figure 5.3: Scatter density plot of the σ° from re-calibrated SAR image A and σ° calculated from collocated H*wind. Both σ° axes are in log space.

estimate the σ°. The polarization ratio p is defined as

$$p = \frac{\sigma^\circ_{HH}}{\sigma^\circ_{VV}} \tag{5.3}$$

where σ°_{HH} and σ°_{VV} are the σ° in HH and VV polarization, respectively. The polarization ratio is less than one for moderate incidence angles (20° to 70°). For C-band, polarization ratio p is dependent on the incidence angle [48]. For low wind speed, p has some dependency on wind speed, while the variation of p with wind speed is quite small for medium to high wind speeds. A wind direction dependency is also observed by Mouche et al. [49] for the incidence angle of 45°. Several C-band polarization models have been proposed using different data sets. Thompson et al. [50] developed a model for the polarization ratio

$$p = \frac{(1 + \alpha \tan^2 \theta)^2}{(1 + 2\tan^2 \theta)^2} \tag{5.4}$$

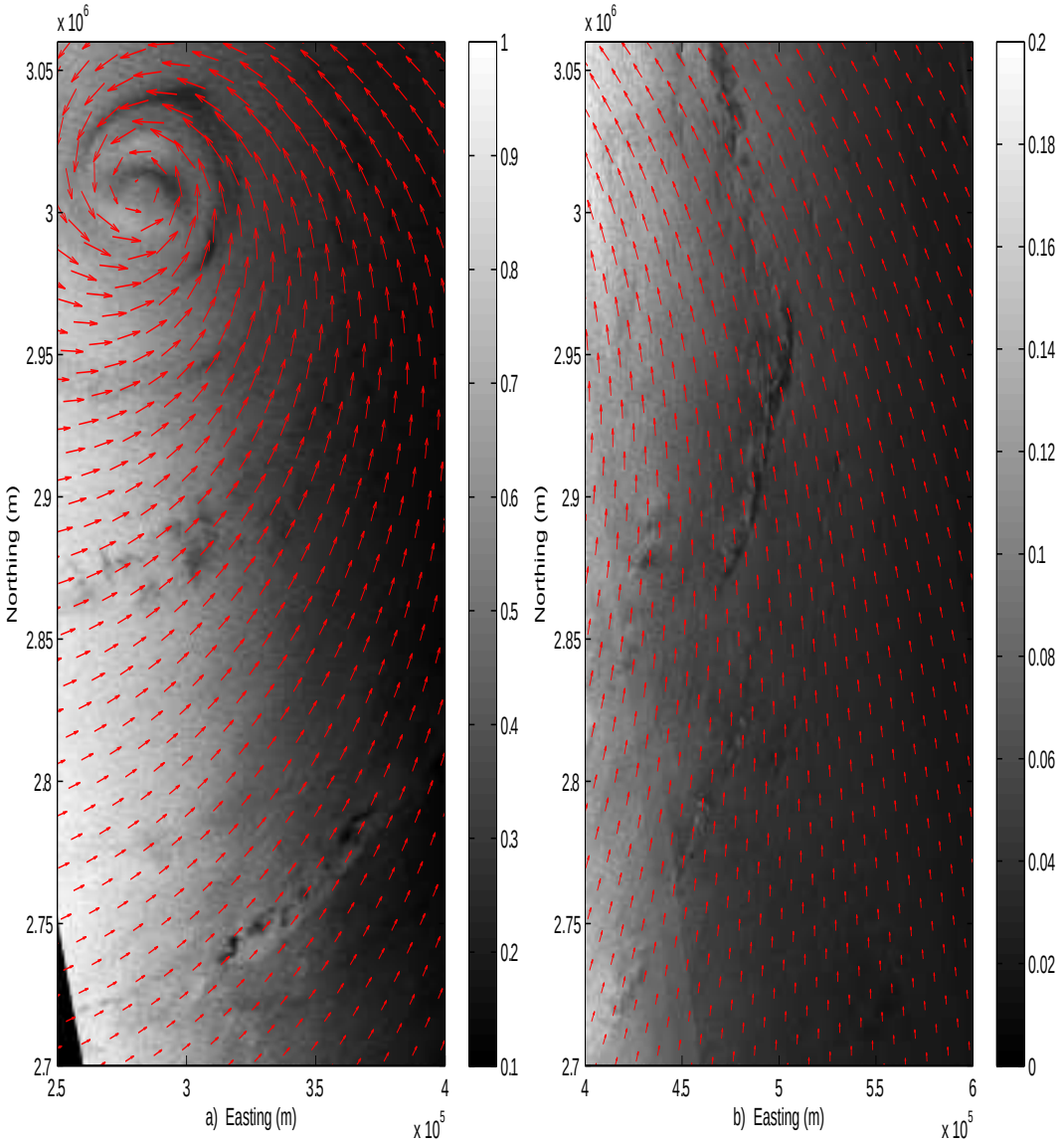

Figure 5.4: Two selected sub-areas of SAR image A. σ° is plotted with the collocated H*wind direction field. The resolution of σ° is 1 km $\times$ 1 km. The posting of H*wind vectors is about 10 km $\times$ 10 km. Due to decreasing of incidence angles from left to right, the σ° changes from light to dark. Because of the "recalibration" used, image artifacts can be observed along the azimuth direction. Rain bands are visible in both panels. Note that the color-scales of a) and b) are different.

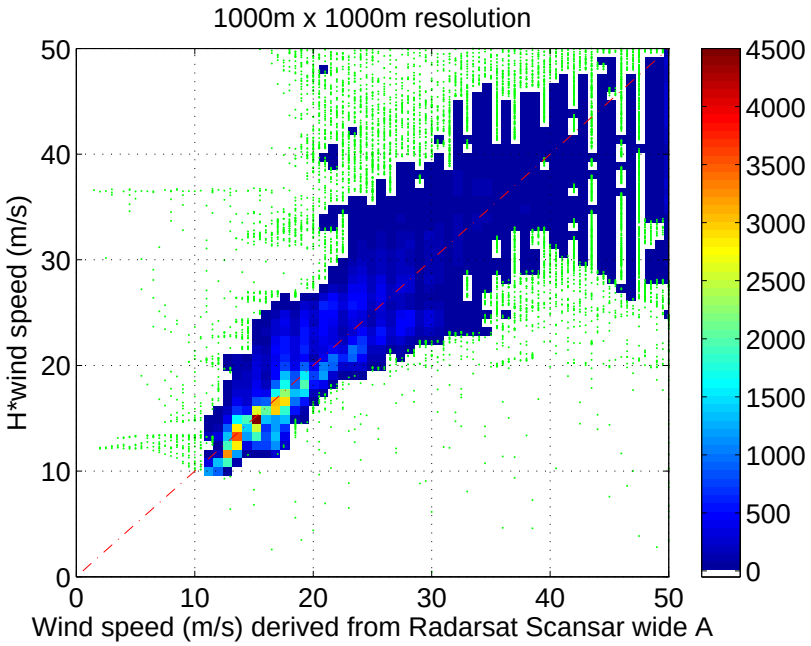

Figure 5.5: Scatter density plot for the SAR-derived wind speed and H*wind speed for SAR image A in (m/s).

where θ is the incidence angle, and α is a constant. The value of α was determined to be 0.6 by fitting the model to the data measured with an airborne SCAT by Unal et al. [48] for several moderate incidence angles with low to medium wind speeds. The value $\alpha = 0.6$ ensures that the proposed model is consistent with both the theoretical polarization ratio for Bragg scattering with $\alpha = 0$ and the Kirchhoff scattering with $\alpha = 2$. The $\alpha = 0.6$ was verified by Monaldo et al. [51] [52] using RADARSAT-1 data and *in situ* data, while Vachon and Dboson [40] found that using Thompson's model with $\alpha = 0.6$ leads to a wind speed overestimate, especially for high wind speeds. The value of α recommended by their study is 1.

Another model for the polarization ratio was proposed by Elfouhaily [53]

$$p = \frac{(1 + 2\sin^2\theta)^2}{(1 + 2\tan^2\theta)^2}. \tag{5.5}$$

The model is obtained by transforming the effective scattering Frensnel coefficient of vertical polarization to horizontal polarization. Using dual-polarization measurements from airborne radar observations, Mouche et al. [54] proposed an empirical

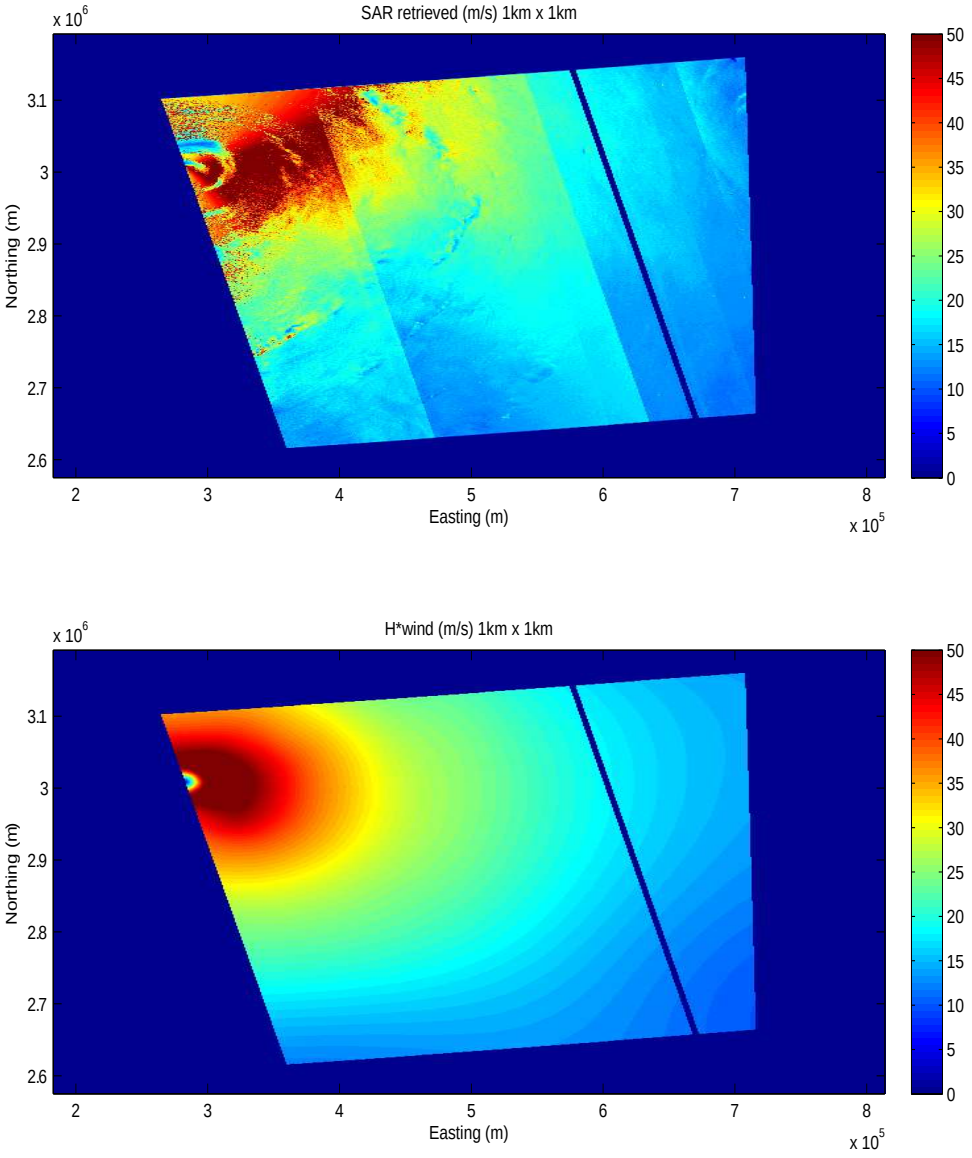

Figure 5.6: Comparison between SAR derived wind speed (top) and H*wind speed (bottom) for SAR image A in (m/s). Due to limitations in the "recalibration" procedure, image artifacts can be observed along the azimuth direction. Wind speeds are possibly overestimated in an area near the eye wall at about northing 3.08E6 m and easting 4.5E5 m. A dark stripe along the track is due to elimination of invalid data.

model

$$p = Ae^{B\theta} + C. \tag{5.6}$$

where $A = 0.008$, $B = 0.1255$, and $C = 0.9973$.

Because each model mentioned above is not well-validated and the model coefficients have a dependency on the specific data set, we compared different models using our data. The σ° estimates from SAR image DN values are compared with the σ° computed from H*wind wind estimates projected through CMOD5 and the polarization model. It is found that the Thompson's model fits image A relatively well, which was acquired on 23:49:05, while the other two models both underestimate the σ°. But all three models do not fit image B well, which was acquired on 23:50:50 UTC. Image B was acquired over the transition area between ocean and land, which may be the reason for the degraded calibration. To compensate for the limitations of the calibration procedure, we adopt a backscatter adjustment model proposed in [55] to recalibrate the SAR measurements. The model coefficients are "tuned" for optimum performance using collocated H*wind wind fields projected through CMOD5 and Thompson's polarization model [50].

The re-calibrated σ°_{re} can be expressed as

$$\sigma^\circ_{re} = \sigma^\circ_{es} G(\theta) M + O \tag{5.7}$$

where σ°_{es} is the σ° estimates from DN value using equation (1), $G(\theta)$ is a parameter dependent on incidence angle, M is a power correction parameter, and O is an offset correction parameter. $G(\theta)$ can be expressed as

$$G(\theta) = \sin^n(\theta) \tag{5.8}$$

where n is a real number. Since ScanSAR SWA combines data from four different beams, each with different incidence angles and different radiometric characteristics, the coefficients of the recalibration model are separately "tuned" for different inci-

dence angle ranges. Table 5.1 shows the recalibration coefficients of image A and B for three incidence angle bins of 22-31 degrees, 31-41 degrees, and 41-47 degrees, respectively. The scatter plots between the two σ° estimates (the re-calibrated ScanSAR σ° and the σ° estimated using H*wind) in normal space and log-log space for image A are shown in Figs. 5.2 and 5.3. It is noted that except for the incidence angle range 22-31 degrees, the coefficients of the recalibration model are very similar for each case, showing the recalibration model is consistent for different SAR image segments.

Table 5.1: Coefficients of the recalibration model.

Image name	incidence angle (degree)	n	M	O
A	22 - 31	-1.12	0.34	0.032
B	22 - 31	-1.7	0.22	0.002
A	31 - 41	-1.2	0.32	0.01
B	31 - 41	-1.18	0.27	0.008
A	41 - 47	-1.11	0.33	0.003
B	41 - 47	-1.115	0.33	0.0055

5.4 Wind Retrieval Results and Analysis

In this section, the vector winds retrieved from the two ScanSAR SWA images are presented. Wind retrieval is done at 1 km $\times$ 1 km by inversion of the GMF using recalibrated σ°. In Fig. 5.4, portions of both re-calibrated σ° and collocated H*wind wind direction vectors of image A are shown. Since the magnitude range of re-calibrated σ° is large, we display the re-calibrated σ° of image A in two sub-images. It is noted that the color-map of sub-image a) and b) are different. Visually, the H*wind wind directions agree well with the key features in the SAR image. Since the magnitude of re-calibrated σ° decreases with increasing incidence angle for a specific wind speed and direction, pixels generally becomes darker from left to right, since incidence angle decreases from left to right. Rain bands and rain cells are visible in σ° field. For the C-band SAR signal, the effects of rain on σ° vary with incidence

angle. At high incidence angles (approximately $\theta > 40°$), rain generally enhances the backscatter, while rain reduces the backscatter at low incidence angles. At moderate incidence angles (approximately $35° < \theta < 40°$), the effect of rain is complex. In Fig. 5.4, one can observe dark spiral rain bands around the hurricane eye, which is due to diminution of $\sigma°$ by rain. While rain adversely affects the wind accuracy, it is not considered in the wind retrieval. We evaluate the rain effect on SAR measurements in Section 5.5.

To validate the SAR-derived wind speeds, we show scatter density plots between the SAR retrieved wind speed fields and the collocated H*wind wind speed fields for image A in Fig. 5.5. Overall, SAR-derived wind speeds agree well with H*wind wind speeds. Except for the influence of rain, the largest errors of wind speed occur at high wind speed (over 25 m/s), where the SAR-derived wind speeds have considerable scatter in comparison to the H*wind wind speeds. These errors are mainly due to the saturation of the C-band GMF CMOD5. Another reason is the inaccuracy of CMOD5 for high wind speed. As shown in Fig. 5.7(c), the shape of $\sigma°$ as an function of wind speed becomes flat over 25 m/s and different wind speeds may produce the same $\sigma°$, as shown in 5.7(b). As a result, the wind retrieval becomes very sensitive to noise for high wind speed and variability of the wind estimates is increased. Figure 5.7(a) shows the percentage of SAR-retrieved wind speeds with a error between SAR-retrieved and H*wind wind speed ($|\mathrm{s}_{sar} - \mathrm{s}_{H*wind}|$) over 15 m/s and collocated H*wind estimated wind speed over 25 m/s, plotted versus wind direction. Compared with Fig. 5.7(b), the largest error percentage corresponds to the wind direction where the $\sigma°$ curves tangle with each other, suggesting that the wind retrieval skills of SAR varies for various wind directions. This limitation of SAR wind retrieval may be improved by using a model-based wind retrieval in hurricane conditions or by developing a wind ambiguity selection algorithm similar to scatterometer wind retrieval in the future.

We show the compact comparison between the two wind speed estimates for image A in Fig. 5.6. As mentioned above, the SAR-retrieved wind speed is noisier in high wind areas (near the hurricane eye). Wind speeds are possibly overestimated

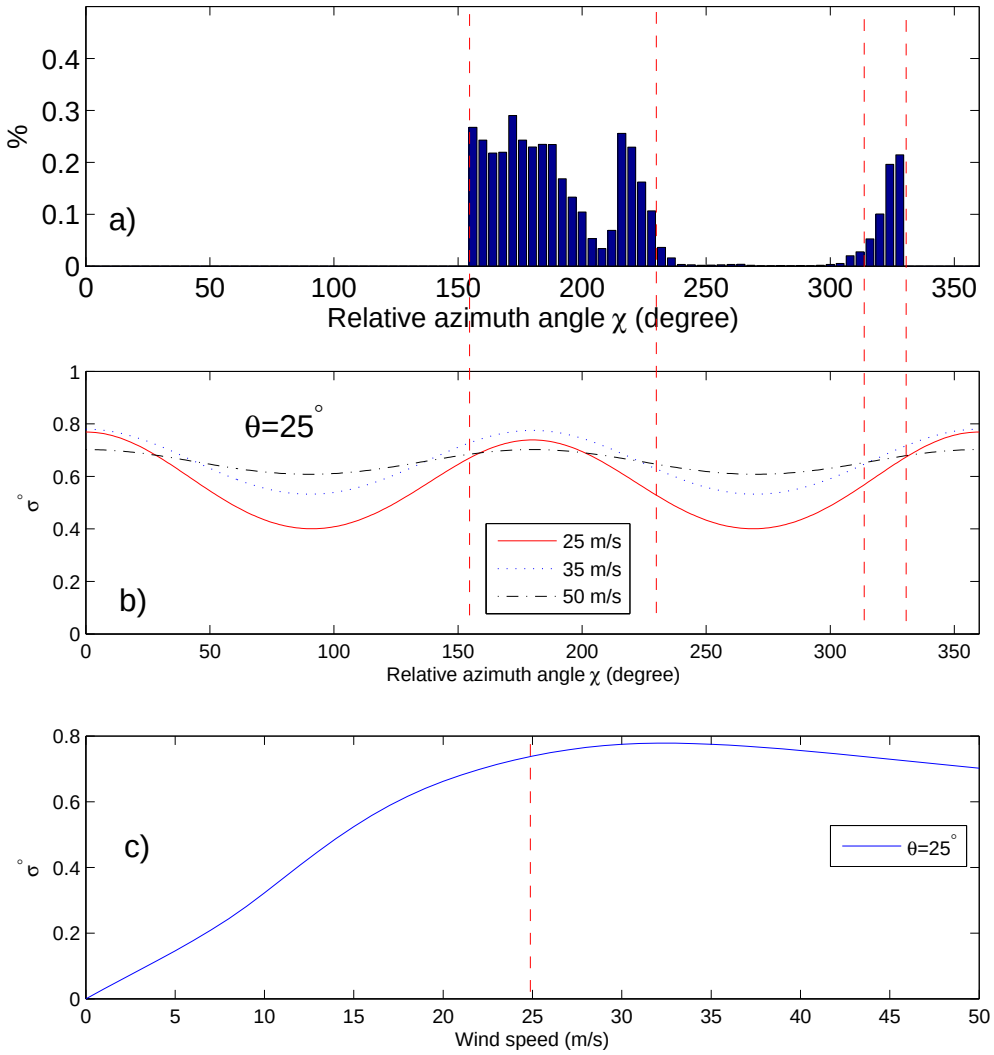

Figure 5.7: High wind speed retrieval performance. (a) The percentage of SAR-retrieved wind speed with a error over 15 m/s and collocated H*wind speed over 25 m/s with respect to relative wind direction. (b) σ° with respect to relative wind direction in the same range. (c) σ° versus wind speed for a relative azimuth angle of 180°.

in an area near the eye wall. Also due to "recalibration", scallops can be observed along the azimuth direction near subswath edges. Effects of rain are also noticeable in the SAR-retrieved wind speed field.

The mean error (SAR retrieved wind - H*wind wind) and RMS error between the two wind speed estimates are listed in Table 5.2. The ScanSAR SWA retrieved wind speed has a small bias, which is possibly caused by rain contamination. The overall root mean squared (RMS) error is below 6 m/s and RMS error for wind speed less than 25 m/s is below 4 m/s, demonstrating relatively high accuracy of SAR-retrieved wind speeds in hurricanes.

Table 5.2: Mean error and RMS errors between the SAR retrieved and H*wind speeds.

Image	Mean error (m/s)	RMS (overall) (m/s)	RMS(<25 m/s) (m/s)
A	-0.21	4.53	2.5
B	0.38	5.7	3.5

5.5 Rain Effects on RADARSAT ScanSAR SWA Measurements

As mentioned in Section 5.1, in raining areas the wind-induced SAR backscatter signature is altered by rain. In this section, we explore these effects.

5.5.1 Rain Effects on C-band SAR Measurements Over the Ocean

In the atmosphere, rain-induced volume-scattering increases the total power backscattered to the SAR, while the SAR signal is also attenuated by the raindrops. Besides rain atmospheric effects, raindrops striking the water create various splash products including rings, stalks, and crowns from which the signal scatters. The contribution of each of these splash products to the backscattering varies with incidence angle and polarization. Ring waves are found to be the dominant features for VV-polarization. For HH-polarization, the radar backscatter from non-propagating splash products increases with increasing incidence angles while the radar backscat-

ter from ring waves decreases. Raindrops impinging on the ocean surface also generate turbulence in the upper water layer which attenuate the short gravity wave spectrum. Using multi-frequency SIR-C/X-SAR data and ERS 1/2 SAR(C band, VV-polarization) data, Melsheimer et al. [9] demonstrate that the modification of the sea surface roughness by falling raindrops mainly depends on the wavelength of water waves. The net effect of the raindrops on the ocean surface is a decrease of the amplitude of water waves which have wavelengths above 10 cm and an increase of the amplitude of water waves with a wavelength below 5 cm. For waves with wavelengths between 5 cm and 10 cm, rain may increase or decrease the amplitude of the Bragg waves, while the critical transition wavelength at which increase turns to decrease is not well defined [9]. The critical wavelength is believed to depend on rain rate, drop size distribution, wind speed, and the temporal evolution of the rain event. The various rain effects on the ocean surface are illustrated in Fig. 5.8.

In addition to surface effects induced by raindrops, the sea surface roughness is also affected by the airflow (downdraft) associated with the rain event as shown in Fig. 5.8. When the downdraft reaches the sea surface, it spreads radially outward as a strong local surface wind that increases the sea surface roughness. Note that the gust front is the outer edge of the downdraft. When the mean ocean surface wind is low, the downdraft is often visible on SAR images over the ocean as a nearly circular bright pattern with a sharp edge [43] [56]. When the ocean surface wind is strong, the airflow pattern is distorted; hence the SAR signature shows bright and dark areas [57]. Using C-band scatterometer (ERS 1/2 VV-polarization) measurements, Nie and Long quantitatively analyzed the rain surface effects on C-band signal at incidence angles higher than 40°. Their study demonstrates that rain surface backscatter can dominate the total backscatter in moderate to heavy rains and a simple phenomenological backscatter model can be used to represent rain backscatter with relatively high accuracy [11]. RADARSAT-1 ScanSAR SWA measurements cover wind incidence angle ranges between 20° and 50°, providing a good opportunity to study the complicated rain effects for C-band HH-polarization SAR measurements at different incidence angles under hurricane conditions. To quantitatively analyze

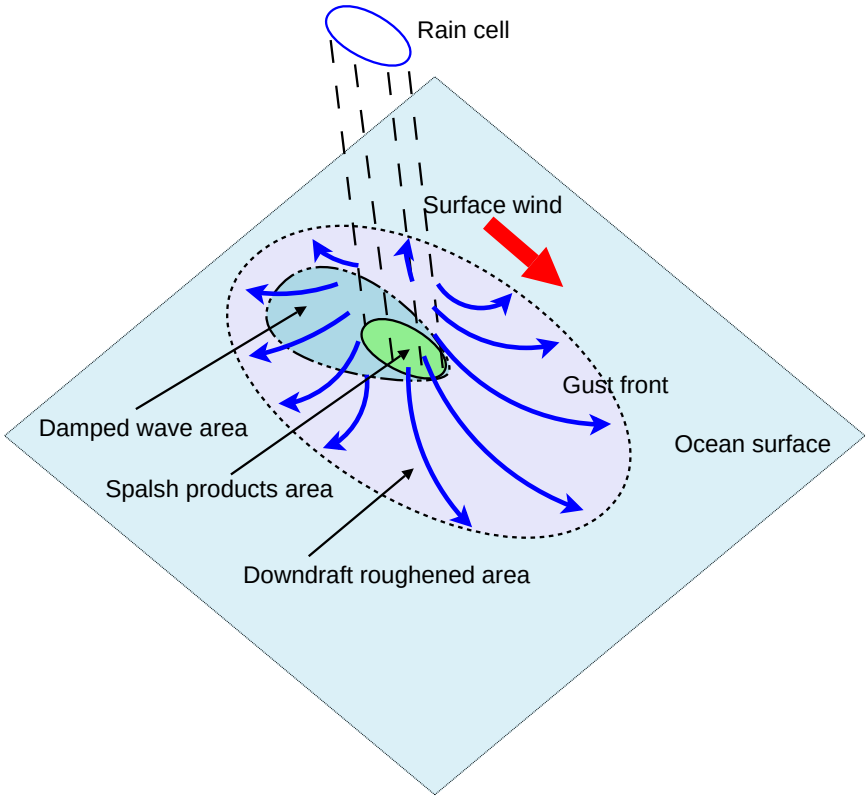

Figure 5.8: Schematic diagram of the various surface effects caused by a rain cell over the ocean. In the splash area, raindrops striking the water create splash products. The damped wave area is created by rain-generated turbulence in the upper water layer. The blue arrows illustrate the airflow of the downdraft, which spreads over and roughens the ocean surface.

the rain effects on SAR measurements, we use the simple backscatter model in [11], which is covered in the next subsection. The SAR response model due to rain atmospheric effects is developed in t he following subsection. Rain-induced atmospheric attenuation and backscatter are estimated using collocated NEXRAD weather radar data. Finally, rain surface perturbations are estimated and modeled.

5.5.2 Wind/Rain Backscatter Model for SAR

In raining areas, the measured normalized radar cross section by the SAR over the ocean is affected by rain atmospheric effects and various surface effects including splash products, turbulence, and downdraft. As shown in Fig. 5.8, the area affected by downdraft and turbulence is larger than the rain core area. Furthermore, the

effect of turbulence varies with the temporal evolution of the rain event. At the beginning of the rain event, the wave damping effect induced by rain is insignificant because surface turbulence is under development. The dampening grows during the rain event then decays after the rain moves on. Since the turbulence decays slowly due to the molecular viscosity of water and the length scales of the turbulence, the damping effect can exist for some time after a rain event ends [9]. Unfortunately, the lifetime of rain-induced turbulence in water has rarely been studied. As a reference, the lifetime of votex rings generated by rain drops impinging the water surface is of the order of a minute for a drop diameter of 1 mm [58]. In the analysis of the SAR measurements, damping effect is still observed about five minutes after rain events. Therefore, it is assumed that the lifetime of rain-induced surface turbulence is of the order of several minutes.

A detailed model of each of the surface effects is beyond the scope of this dissertation. Instead, we model the bulk effect of rain on the Bragg wave field in the rain core area by combining all the surface contributions together into a single rain surface perturbation term, σ_{surf}. σ_{surf} is assumed to be additive with the wind-induced surface backscatter. The rain-modified measured backscatter, σ_m, is represented by a simple additive model

$$\sigma_m = (\sigma_{wind} + \sigma_{surf})\alpha_{atm} + \sigma_{atm} \tag{5.9}$$

where σ_{wind} is the wind-induced surface backscatter, σ_{surf} is the rain-induced surface perturbation backscatter, α_{atm} is the two-way rain-induced atmospheric attenuation, and σ_{atm} is rain-induced atmospheric backscatter.

As before, the σ_{wind} is estimated by projecting H*wind wind speeds (s) and directions (d) through HH-polarization GMF,

$$\sigma_{wind} = \text{CMOD5}(s, d, \chi, \theta)p(\theta) \tag{5.10}$$

where χ is the azimuth angle of SAR measurements, θ is the incidence angle, and $p(\theta)$ is the recalibrated Thompson's polarization ratio model.

5.5.3 Evaluation of Atmospheric Attenuation and Backscattering

The SAR measurement geometry is displayed in Fig. 5.9. For simplicity, we

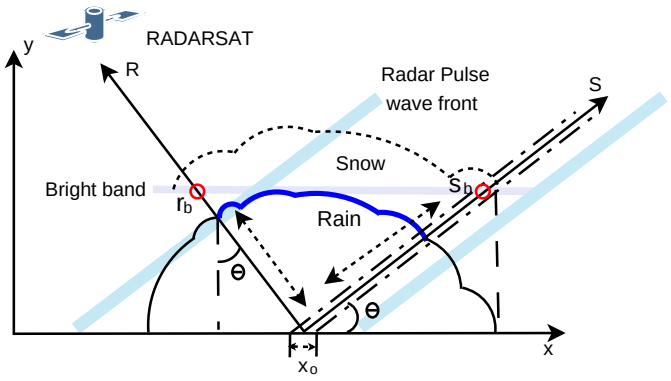

Figure 5.9: Schematic diagram of the SAR scattering geometry for a rain cell. The oblique lines represent the radar pulse under the approximation of plane wave incidence.

use a plane-wave incidence approximation to represent the synthetic aperture radar pulse. we define a new coordinate system $r - s$. r is along the SAR slant range and s is perpendicular to r. For the SAR surface backscatter at $x_\circ$, the atmospheric attenuation is contributed by the raindrops along coordinate r from the surface to the bright band altitude and by snow above the bright band. The typical altitude of the bright band is about 5 km.

The attenuation coefficient of rain, K_r, can be estimated using the k_r - R (R is rain rate in mm/hr) relationship [28]

$$K_r = aR^b \quad \text{dBkm}^{-1} \tag{5.11}$$

where $a = 0.0018\ dBkm^{-1}$ and $b = 1.05$ for a 5 cm SAR signal wavelength. R is the rain rate in mm/hr. The attenuation coefficient of snow is related to snowfall rate by [28]

$$K_s = 0.0222\frac{R^{1.6}}{\lambda^4} + 0.34\varepsilon_i''\frac{R}{\lambda} \quad \text{dBkm}^{-1} \tag{5.12}$$

where λ is the wavelength, $\varepsilon_i'' \simeq 10^{-3}$ at $-1°C$. For $\lambda = 5.6$ cm, $R = 100$ mm/hr, $K_s = 0.04$ dBkm^{-1}, while $K_r = 0.227$ dBkm^{-1} under the same conditions. Therefore, the attenuation due to snow is negligibly small and is ignored in the following analysis. Then, the path integrated attenuation (PIA) in dB is equal to the integration of $K_r(r,s)$ through the R axis ($s = 0$), from the bright band altitude, r_b (shown in Fig. 5.9), to the ocean surface, 0,

$$PIA = 2\int_0^{r_b} k_r(r,0)dr \quad \text{dB} \tag{5.13}$$

where $k_r(r,0) = aR(r,0)^b$. Since $r = (x_0 - x)/\sin\theta$ and $k_r(r,0) = k_r\Big(x, (x_0 - x)/\tan\theta\Big)$, the above equation can be expressed as

$$PIA = 2\frac{1}{\sin\theta}\int_{x_0 - r_b\sin\theta}^{x_0} k_r\left(x, \frac{x_0 - x}{\tan\theta}\right)dx \quad \text{dB}. \tag{5.14}$$

The two way atmospheric attenuation factor α_{atm} is calculated by converting the PIA to normal space,

$$\alpha_{atm} = 10^{-PIA/10}. \tag{5.15}$$

The atmospheric backscatter (σ_{atm}) observed by the SAR is estimated from the rain rate obtained from the NEXRAD measurements. For a specific position on coordinate s, the effective reflectivity of the atmospheric rain, $Z_e(0,s)$, is calculated using Equation (5.2). The volume backscattering coefficient σ_{vc} can be computed from [28]

$$\sigma_{vc}(0,s) = 10^{-10}\frac{\pi^5}{\lambda_\circ^4}|K_w|^2 Z_e(0,s) \ \ \text{m}^2/\text{m}^3 \tag{5.16}$$

where $\lambda_\circ = 5.6$ cm is the wavelength of RADARSAT-1 SAR, and $|K_W|^2$ is a function of the wavelength $\lambda_\circ$ and the physical temperature of the material. K_w is assumed to be 0.93 for the water and 0.19 for snow in this paper [12]. The quantity σ_{vc} represents physically the backscattering cross-section (m^2) per unit volume (m^3). According

to [59], the Z-R relationship for snow is $Z = 427R^{1.09}$. With the precipitation rate equal to $10mm/hr$, rain-induced backscattering is about 6 times the snow-induced backscattering. In addition, the range of snow precipitation rates is several times lower than that for rain because snowflakes fall at a much lower velocity than rain drops do [12]. Hence, we do not consider the snow-induced volume backscattering in this study.

The volume backscattering cross-section observed by the SAR is attenuated by the two-way attenuation factor, $\alpha_{atm}(0, s)$,

$$\sigma_{vro}(0, s) = \sigma_{vc}(0, s)\alpha_{atm}(0, s) \tag{5.17}$$

where $\alpha_{atm}(0, s)$ is the path integrated two-way attenuation at s on S axis. The total atmospheric rain backscatter as seen by SAR is $\sigma_{vro}(r, s)$ integrated through the radar pulse plane (along the S axis where $r = 0$) from the bright band altitude on the S axis (shown in Fig. 5.9), s_b, to the ocean surface, 0,

$$\sigma_{atm} = \sin\theta \int_0^{s_b} \sigma_{vro}(0, s)ds \quad \mathrm{m}^2/\mathrm{m}^2 \tag{5.18}$$

where θ is the incidence angle. Since $s = (x - x_0)/\cos\theta$ and $\sigma_{vro}(0, s) = \sigma_{vro}\Big(x, (x - x_0)\tan\theta\Big)$, the above equation can be transformed to coordinate $x - y$ as

$$\sigma_{atm} = \tan\theta \int_{x_0}^{x_0 + s_b\cos\theta} \sigma_{vro}\Big(x, (x - x_0)\tan\theta\Big)dx. \tag{5.19}$$

After calculating σ_{atm} and α_{atm}, we estimate the surface perturbation backscatter σ_{surf} by

$$\sigma_{surf} = \alpha_{atm}^{-1}(\sigma_m - \sigma_{atm}) - \sigma_{wind} \tag{5.20}$$

where the σ_{surf} can be negative at low incidence angles, corresponding to the loss of the wind-induced backscatter. A positive value is an increase in the net backscatter.

5.6 Results and Analysis

Based on the methods mentioned above, we quantitatively analyze the radar backscatter of several rain cells at different incidence angles as shown below.

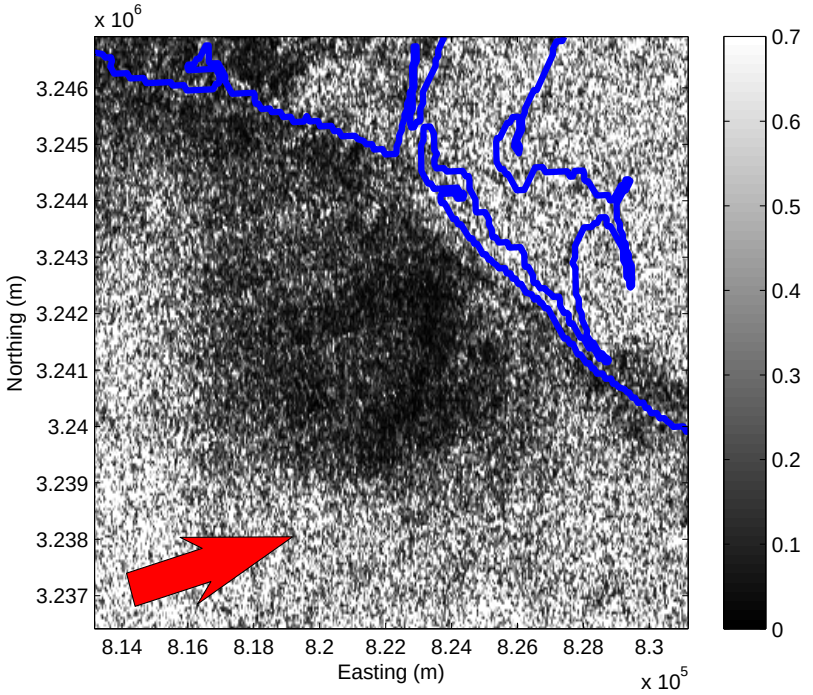

Figure 5.10: σ° of a rain cell located near the sea shore of New Orleans in hurricane Katrina. The coast line is marked using solid lines and the red arrow shows the azimuth direction of RADARSAT ScanSAR observation. The near-surface wind speed is $\approx$ 20 m/s.

5.6.1 Incidence Angle Between 22° and 23.6°

Figure 5.10 displays the SAR σ° of a typical rain cell located near the sea shore. The collocated H*wind speed and vectors are shown in Fig. 5.11. The incidence angles of the SAR measurements are between 22° and 23.6°. At this incidence angle, the dominant rain effect is a dampening of the the surface backscatter; hence, the rain cell looks darker than the surrounding rain free ocean in the SAR image. The H*wind model predicts that the wind speed in this area is essentially constant. Since the LIX

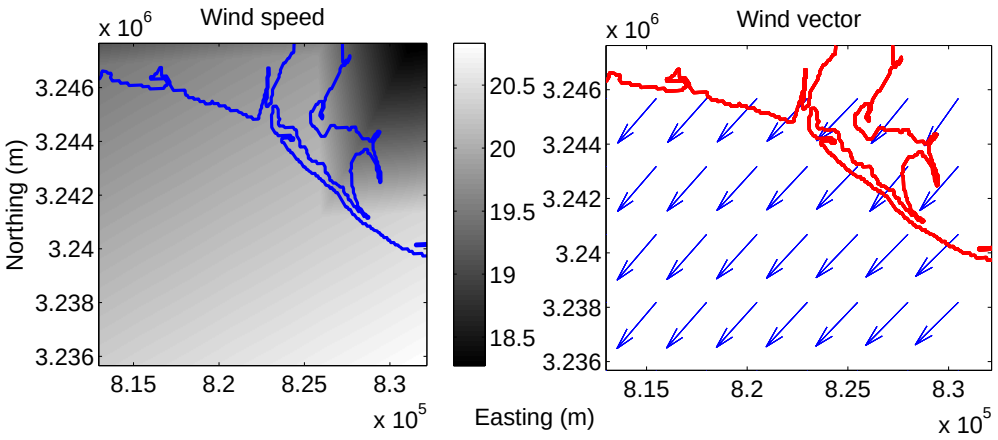

Figure 5.11: Wind speed and wind vectors for the collocated H*wind for the region in Fig. 5.10.

NEXRAD station is the closest, radar data from LIX station is used to calculate the rain rates.

Because the gain spatial response function is not uniform over the NEXRAD footprint, the NEXRAD-observed rain is a weighted-average of the rain. To compensate for this, the collocated SAR measurements are averaged over the NEXRAD footprint by weighting with the NEXRAD spatial response function within the 3-dB antenna pattern contour. Lacking accurate information for NEXRAD's spatial response function, we use a Gaussian radiation pattern in this study [19]. To minimize the errors introduced by the SAR and NEXRAD data processing, the different map projections, and the spatial and time differences between the two sensors, we assume the rain is uniformly distributed in the vertical direction and use the vertically-averaged rain rate as the surface rain rate.

Figure 5.12(a) and (b) displays the atmospheric attenuation and backscatter induced by rain. Compared with the surface σ° at this incidence angle range, the atmospheric backscatter is insignificant, while the atmospheric attenaution is significant in heavy rains. Due to the SAR geometry, the SAR measurements affected by rain atmospheric attenuation and backscattering are not limited to the rain-cell area. Figure 5.13(a) and (b) display the collocated σ_{surf} and the NEXRAD surface rain rate, respectively. In Fig. 5.13(c) and (d), the profiles of rain rate and σ_{surf} are

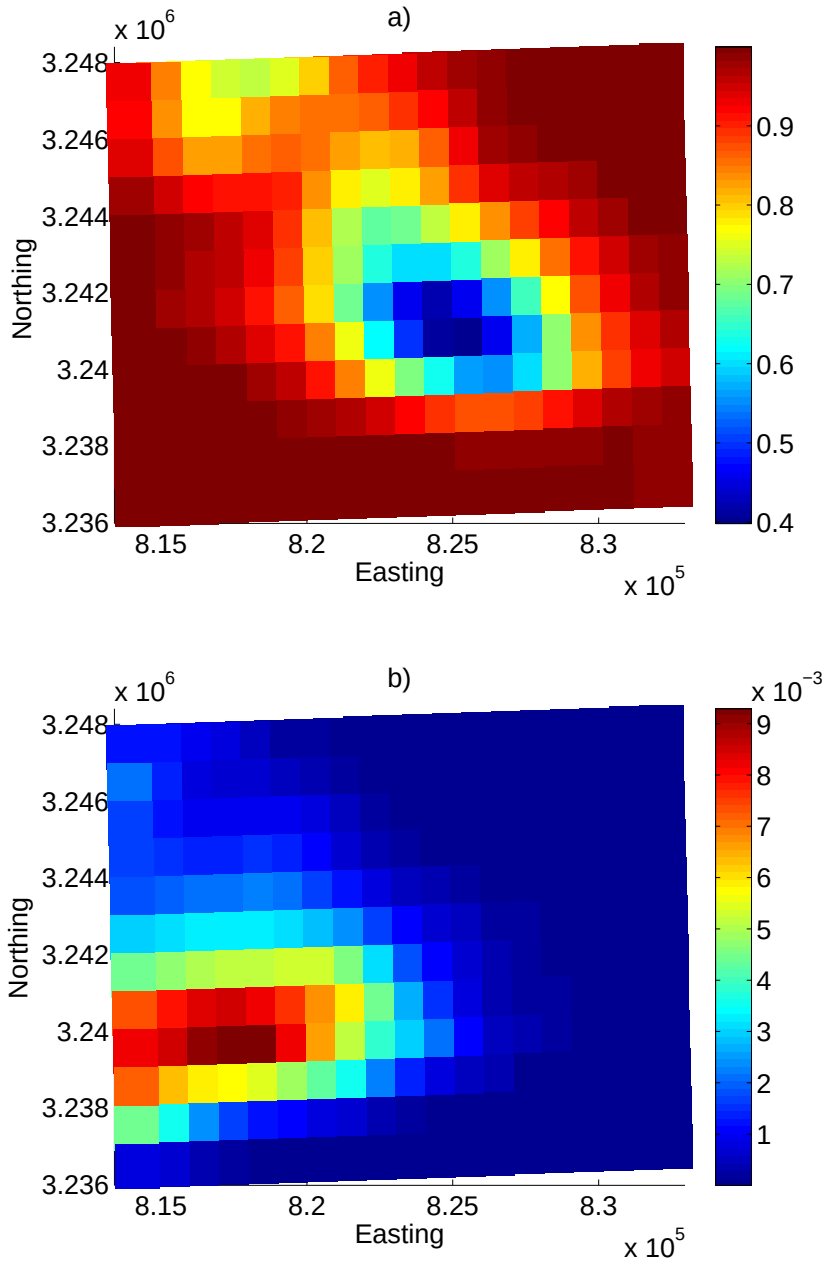

Figure 5.12: (a) Rain-induced atmospheric attenuation and (b) atmospheric backscatter of the region in Fig. 5.10.

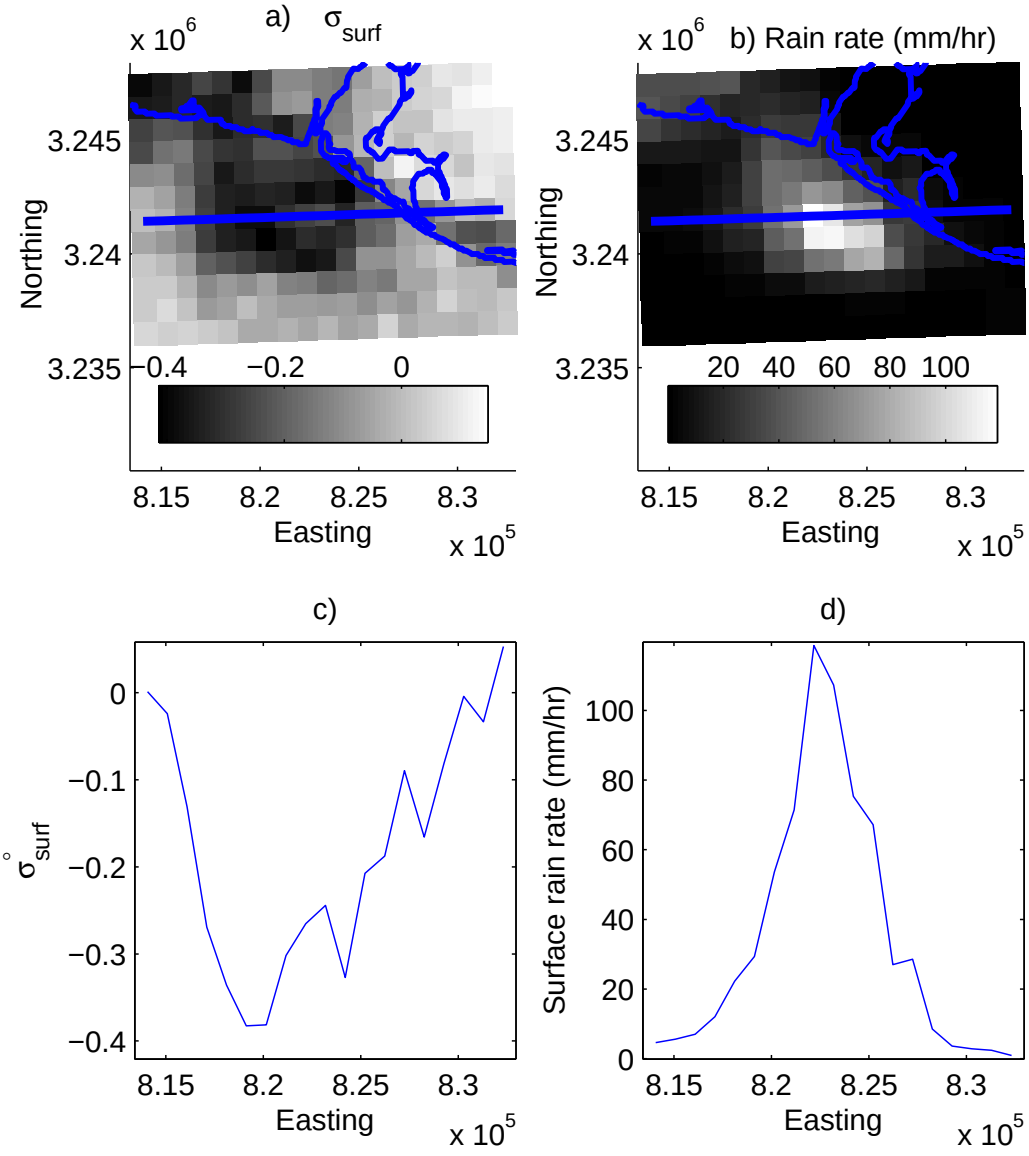

Figure 5.13: (a) σ°_{surf} of the rain cell in Fig. 5.10. (b) The collocated NEXRAD rain rate in mm/hr. (c) and (d) the profile of σ° and rain rate along the solid line plotted in (a) and (b).

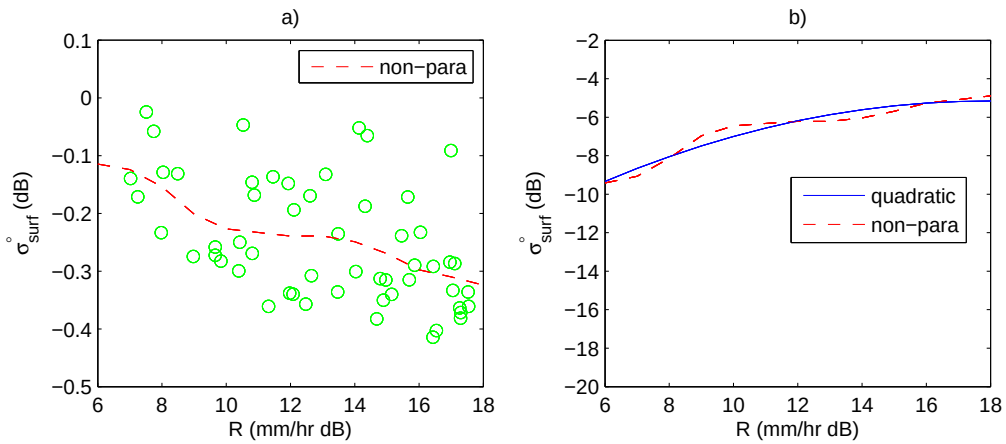

Figure 5.14: (a) σ°_{surf} versus rain rate nonparametric fit. (b) Quadratic fit to σ_{surf} in log-log space compared to the non-parametric fit.

plotted along the red solid line in Fig. 5.13(a) and (b). These show that the σ_{surf} generally decreases as rain rate increases. Note that the profile of σ_{surf} is wider than the rain rate profile.

To relate the σ_{surf} with rain rate, we use a power law model [11]. σ_{surf} can be expressed as polynomial function of rain rate,

$$10log_{10}(\sigma_{surf}(\theta)) \approx f_{sr}(R_{dB}) = \sum_{n=0}^{N} x_{sr}(n) R_{dB}^{n} \tag{5.21}$$

where $R_{\mathrm{dB}} = 10log_{10}(R_{surf(ant)})$, and $x_{sr}(n)$ are the corresponding model coefficients. $N = 1$ for the linear model, and $N = 2$ for the quadratic model. Because the estimate of σ_{surf} is relatively noisy, we first make a nonparametric estimate of σ_{surf} as a function of R_{dB} using an Epanechnikov kernel with a 2 mm/hr dB bandwidth in rain rate as shown in Fig. 5.14(a). Then, we estimate the model coefficients for the quadratic model using a linear least-squares fit as shown in Fig. 5.14(b). In the following analysis of other rain cells, we use this same method.

5.6.2 Incidence Angle Between 28° and 31.7°

Figure 5.15 displays the SAR signature of a rain cell over the ocean about 150 km from the MOB radar. At this incidence angle range, the damping effect of

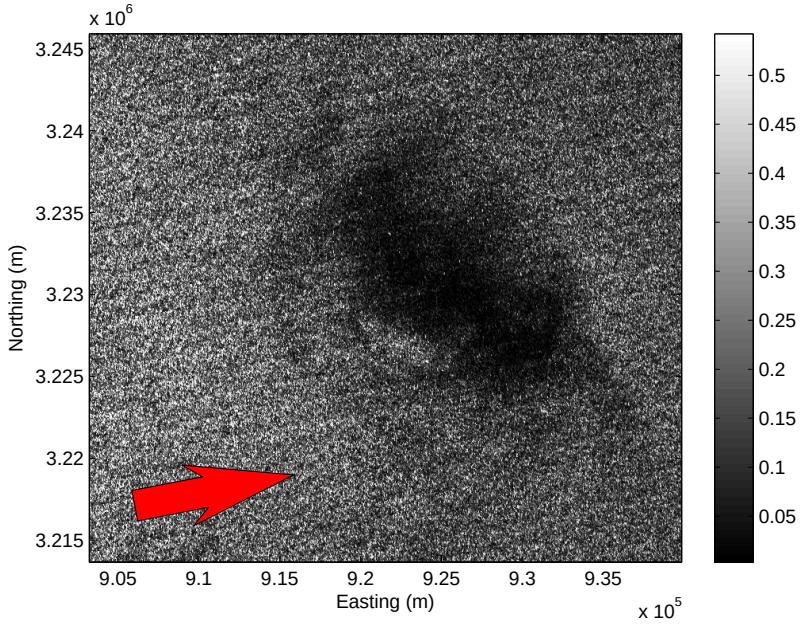

Figure 5.15: σ° of a rain cell located near the sea shore of New Orleans in hurricane Katrina. The red arrow shows the azimuth direction of RADARSAT ScanSAR observation. The near-surface wind speed is $\approx$ 22 m/s.

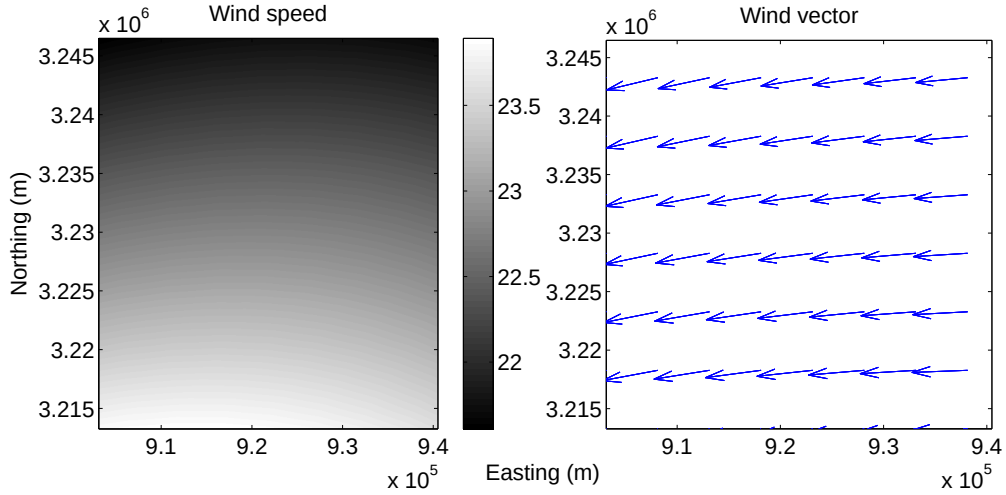

Figure 5.16: Wind speed and wind vectors for the collocated H*wind corresponding to Fig. 5.15.

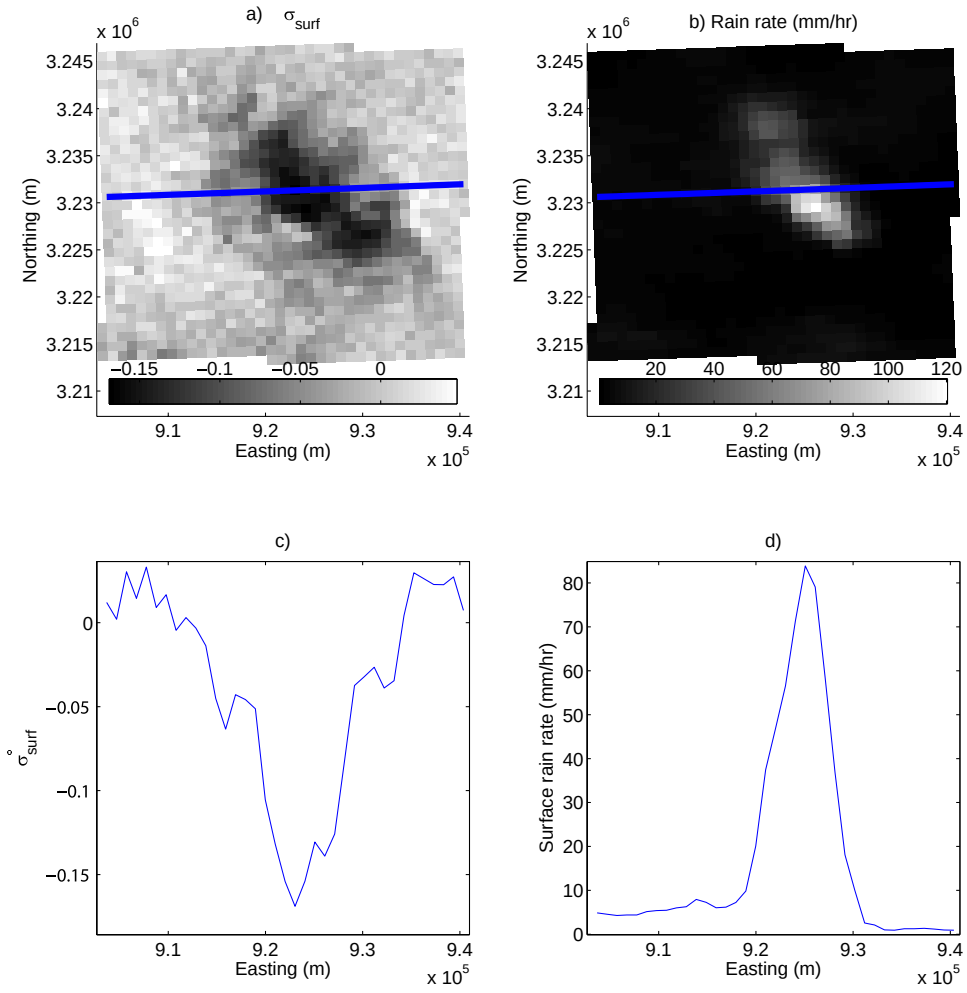

Figure 5.17: (a) σ°_{surf} of the rain cell in Fig. 5.15. (b) The collocated NEXRAD rain rate in mm/hr. (c) and (d) the profile of σ° and rain rate along the solid line plotted in (a) and (b).

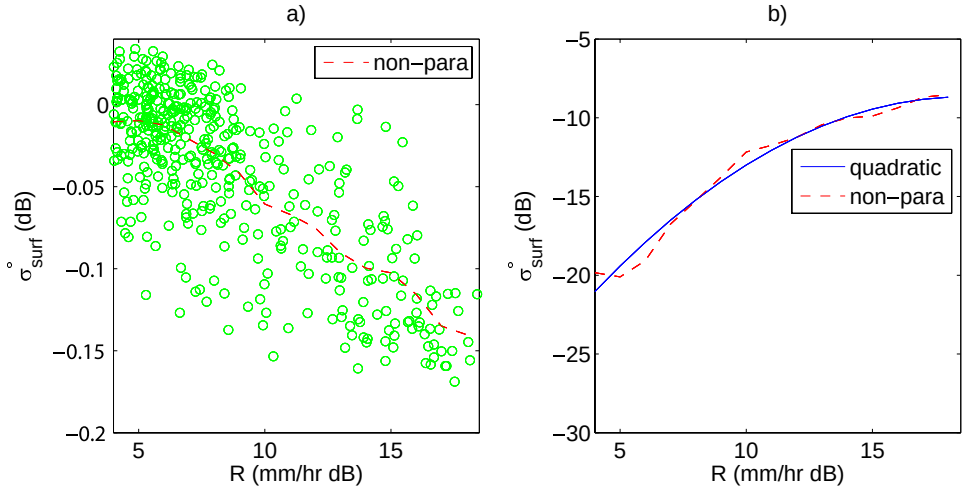

Figure 5.18: (a) Nonparametric fit to σ_{surf}. (b) Quadratic fit to the non-parametric fit of σ_{surf} in log-log space.

rain is dominant. Figure 5.17 displays the rain effect, which is a negative "surface backscatter", and the collocated NEXRAD rain field. Figure 5.16 displays the collocated H*wind speed and directions. Figure. 5.18(a) illustrates the non-parametric fit to the estimated σ_{surf} with respect to R_{dB} and (b) displays the quadratic fit to the non-parametric fit.

As shown in Fig. 5.18, the loss due to damping effect is as high as -7 dB when $R \approx 63$ mm/hr, which is significant compared to the wind-induced surface backscatter. Due to relatively large number of collocated data points, the nonparametric fit in Fig. 5.18(a) is smooth and the quadratic fit agrees well with the nonparametric fit in Fig. 5.18(b).

5.6.3 Incidence Angle Between 44° and 45.7°

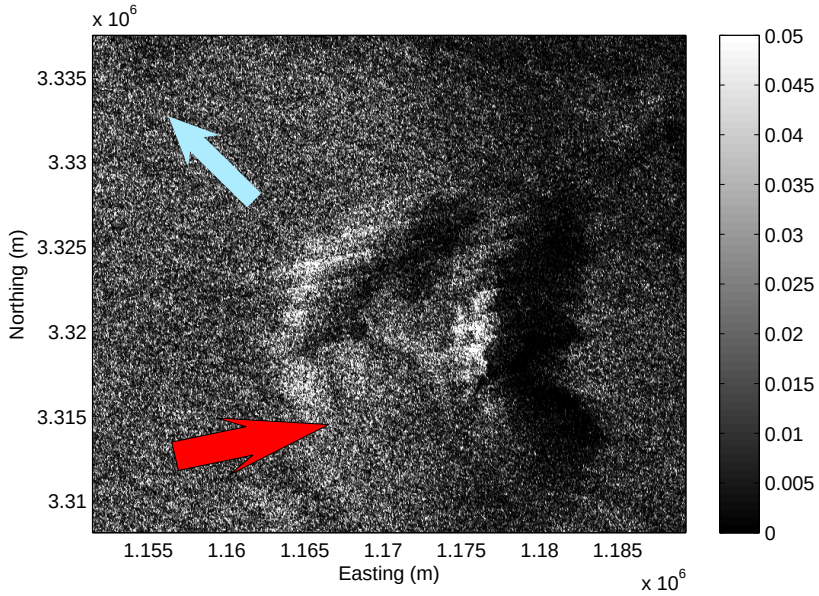

Figure 5.19: σ° of a rain cell located near the sea shore of New Orleans in hurricane Katrina. The red arrow shows the azimuth direction of RADARSAT ScanSAR observation and the light blue arrow shows the wind direction. The near-surface wind speed is ≈ 10 m/s.

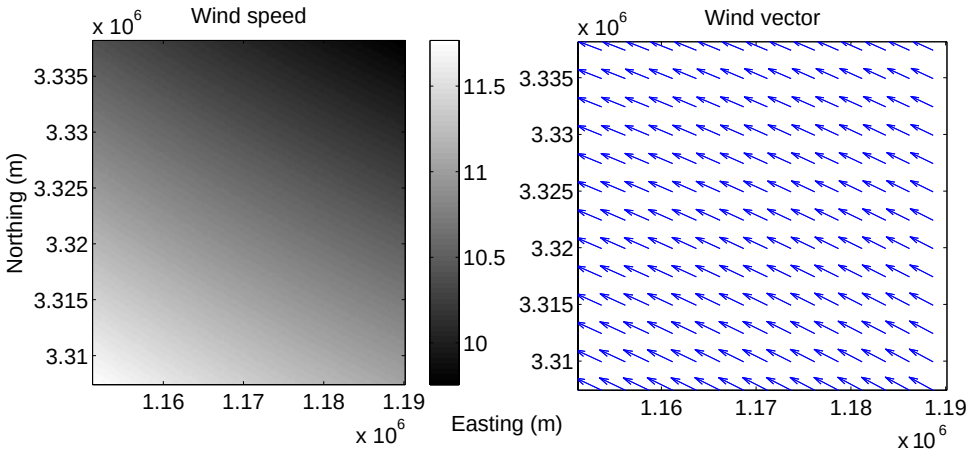

Figure 5.20: Wind speed and wind vectors for the collocated H*wind corresponding to Fig. 5.19

.

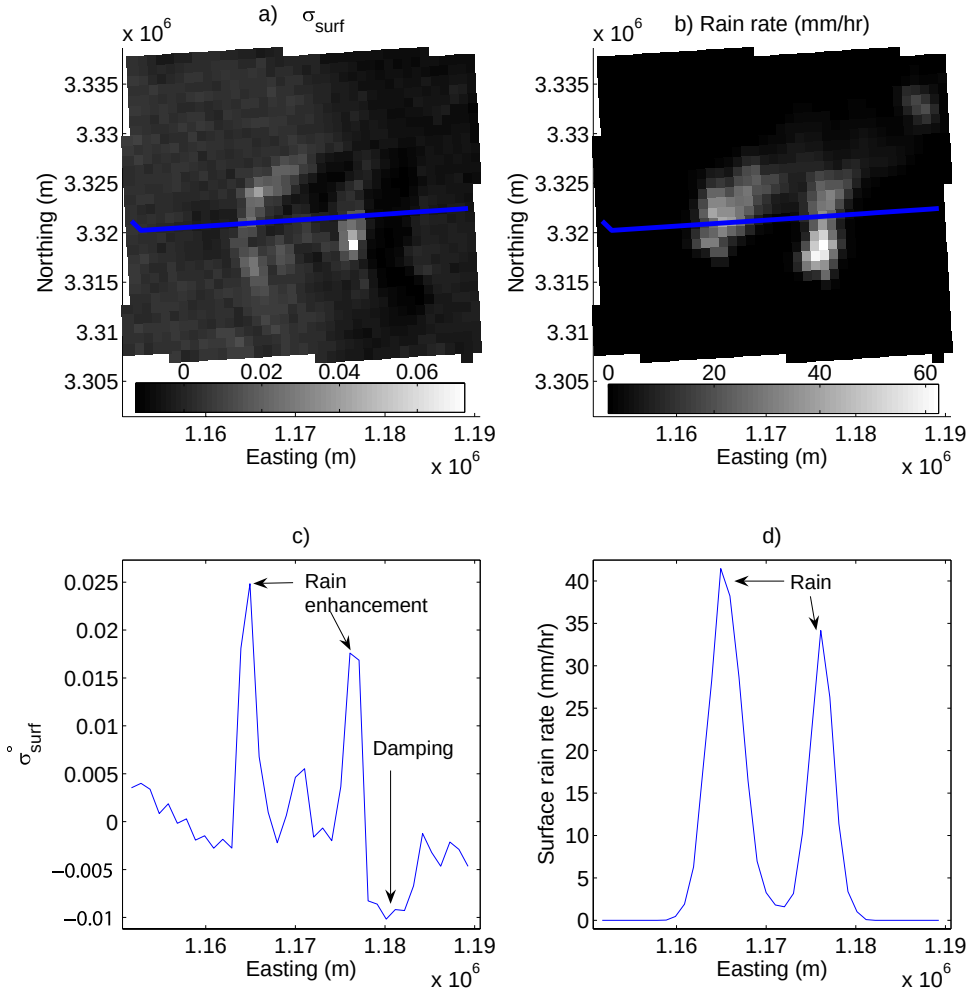

Figure 5.21: (a) σ°_{surf} of the rain cell in Fig. 5.19. (b) the collocated NEXRAD rain rate in mm/hr. (c) and (d) display the profile of σ° and rain rate along the solid line plotted in (a) and (b).

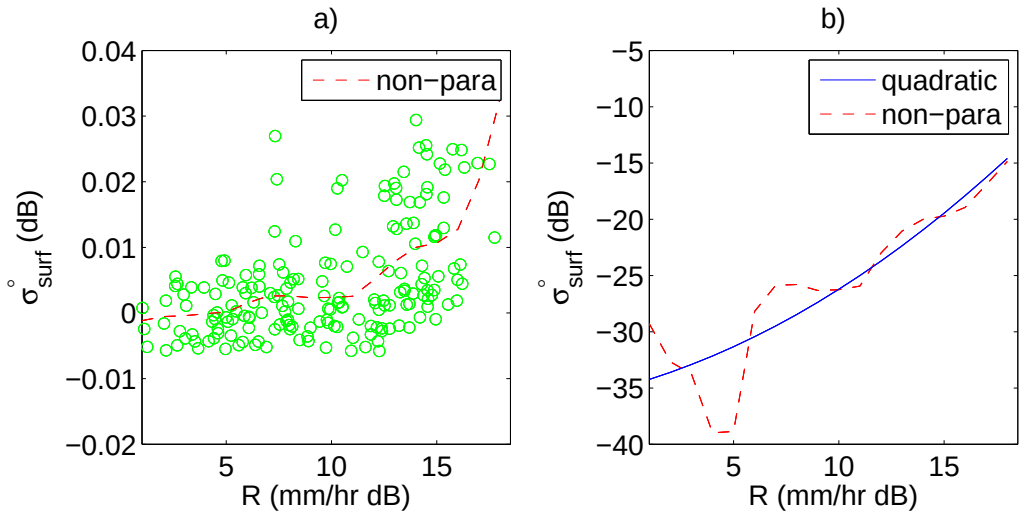

Figure 5.22: (a) Nonparametric fit to σ_{surf} for Fig. 5.19. (b) Quadratic and linear fits to the non-parametric fits of σ_{surf} in log-log space. Non-parametric fits are also plotted.

Figure 5.19 displays the SAR signature of a rain cell over the ocean which is about 70 km from the EVX radar. Through comparison between σ_{surf} and rain rate in Fig. 5.21, we find that the enhancing effect of rain is dominant within the rain cells. However, damping areas (which are darker due to reduced σ°) are found next to the rain enhanced areas. The damping areas have shapes similar to the rain cells but are shifted due to motion of the rain cell. Note that two negative peaks exist in the profile of σ_{surf} along the solid line, as shown in Fig. 5.21. Because the wind direction is pointing in the west-northern direction, as shown in Fig. 5.20, the rain cells is moving towards west-north, as shown in Fig. 5.24. The path of the rain cells shown in Fig. 5.24(b) matches the damping areas shown in Fig. 5.24(a). As discussed in Section 5.5.2, the damping effect continues after rain events. Hence the damping area is the result of the rain previously falling in the area. Since the rain cell is moving with the wind, it is leaving, in effect, a "trail" of damped wave surface. Unfortunately, the life time of damping effect is rarely been studied, while it might depend on many factors such as the type of rain, rain rate, drop size distribution, wind speed, incidence angle, and so on. As shown in Fig. 5.24(a) and (b), the damping area (near Easting 1.18×10^6 m) collocates with the rain measurements acquired 5

and 10 minutes ago. Therefore, the life time of the damping effect is approximately between 5 and 10 minutes, when wind speed is about 10 m/s, rain rate is about 70 mm/hr, and incidence angle is about 45 degree.

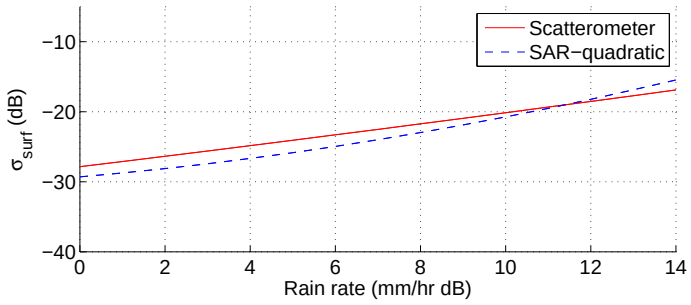

Figure 5.23: Surface perturbation, σ_{surf}, versus rain model comparison between SAR-derived quadratic model with a plot of the scatterometer-derived model shown.

Figure 5.22(a) illustrates the non-parametric fit to the estimated σ_{surf} with respect to R_{dB}, while Fig. 5.22(b) displays the quadratic and linear fits to the non-parametric fit. In Fig. 5.22(b), the linear and quadratic model are close, suggesting that σ_{surf} is almost a linear function of surface rain rate in log-log space.

Figure 5.23 compares the scatterometer C-band VV polarization backscatter model developed in Chapter 2 and the quadratic model derived from the HH polarization SAR measurements adjusted with the Thompson's polarization model (Equation 5.4) for this rain cell. The two models are close, suggesting that the SAR-derived σ_{surf} versus rain is consistent with the scatterometer-derived model when the polarization difference between HH and VV polarizations is considered. Unfortunately, systematic comparison between these two models is impossible due to a lack of sufficient data.

5.6.4 Rain Model Coefficients

In the previous section, three typical rain cells at different incidence angles are examined. The coefficients of the model for the three incidence angles are listed in Table 5.3. σ_{surf} versus rain rate at the different incidence angles is plotted in Fig. 5.25. The σ_{surf} versus rain model at high incidence angle is close to a linear model in log-

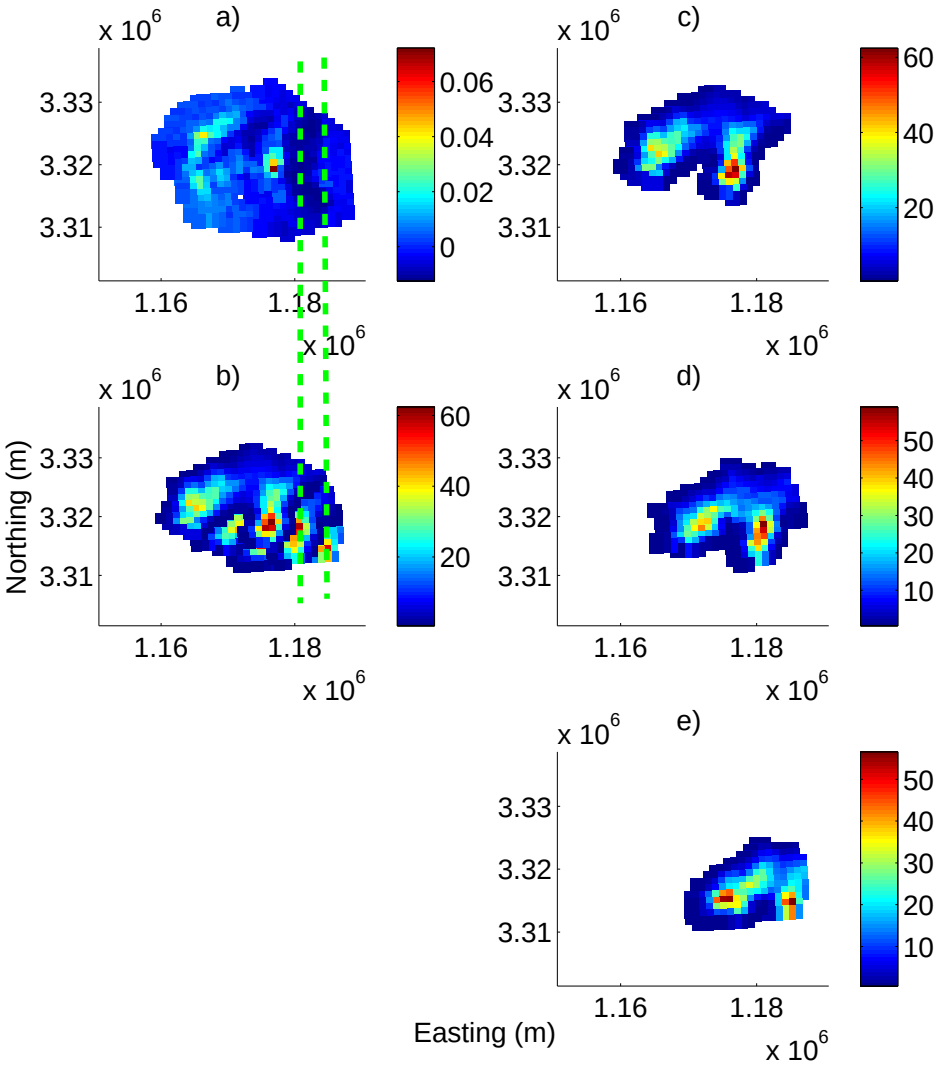

Figure 5.24: (a) σ_{surf} derived from RADARSAT image. (b) Overlay of the NEXRAD measurements from (c)-(e). (c) NEXRAD measurements collocated with the SAR measurement time. (d) NEXRAD measurements about 5 minutes prior to the SAR observation. (e) NEXRAD measurements about 10 minutes prior to the SAR observation. The arrow shows the moving direction of the rain cells.

log space. We further investigate the relationship between σ_{surf} and incidence angle by plotting the σ_{surf} with respect to incidence angle for a specific surface rain rate in Fig. 5.26. The magnitude of σ_{surf} generally decreases with incidence angles. At heavy rain rates, the decreasing ratio is smaller than at low to moderate rain rates.

Table 5.3: Coefficients of the σ_{surf} model at three incidence angles.

Incidence angle (°)	p(0)	p(1)	p(2)
22 - 23	-14.6081	1.0563	-0.0295
28 - 31.7	-28.6799	2.1404	-0.0572
44 - 45.7	-34.79	0.5249	0.0332

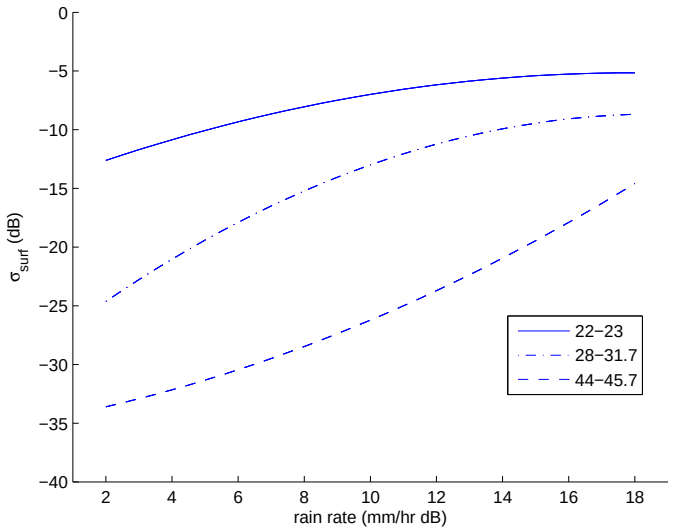

Figure 5.25: σ_{surf} versus rain rate at different incidence angles. Note that for incidence angle bins $22-23$ degree and $28-31$ degree $-\sigma_{surf}$ in dB is displayed (Due to damping effect, σ_{surf} is negative at these incidence angles).

As mentioned above, at low incidence angles loss of σ_{surf} occurs due to the damping effect of rain, while rain enhances the backscatter at high incidence angles. As shown in Fig. 5.26, both the loss and enhancement of σ_{surf} can be a significant

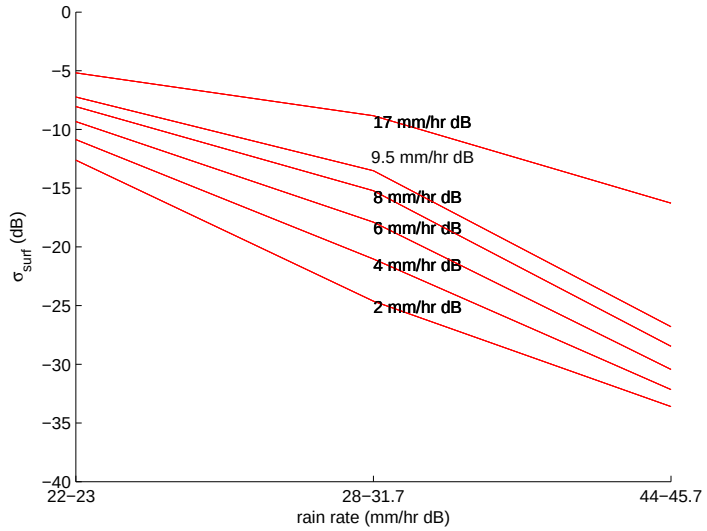

Figure 5.26: σ_{surf} versus incidence angle for various rain rates at different incidence angles. Note that for incidence angle bins $22-23$ degree and $28-31$ degree $-\sigma_{surf}$ in dB is displayed (Due to damping effect, σ_{surf} is negative at these incidence angles).

component of the total backscatter in moderate to heavy rain rates. Hence modeling the rain effects on C-band signals is very important for SAR wind retrieval.

5.7 Conclusion

RADARSAT-1 ScanSAR SWA images of Hurricane Katrina are used to retrieve the surface wind vectors over the ocean. Due to the inadequate spatial resolution of the ScanSAR SWA images, the spectrum method cannot be implemented to estimate the wind direction. Instead, collocated H*wind wind directions are used as wind direction estimates. Using these direction estimates the wind speed is derived from σ° by inversion of a C-band HH-polarization Geophysical Model Function (GMF), which is derived from the C-band VV-polarization GMF, CMOD5, using a polarization ratio model. Because existing polarization models do not fit the ScanSAR SWA data well, a recalibration model is proposed to recalibrate the ScanSAR SWA images. The coefficients of the recalibration model are tuned using collocated H*wind surface wind fields. To validate the SAR-retrieved wind speed, the mean and the RMS difference between SAR-retrieved and H*wind wind speed estimates are calculated.

The mean of difference is negligible and the RMS difference is below 4 m/s. Except for the influence from rain, the largest errors occur at high wind speed (over 25 m/s), which is due to the saturation of the GMF. While wind speed estimates over 25 m/s are noisy, no obvious bias is found, suggesting that the wind retrieval algorithm can work under hurricane conditions.

Using the recalibrated ScanSAR SWA measurements, collocated ground-based Doppler weather radar (NEXRAD) measurements, and collocated H*wind fields are used to study the complicated rain effects on the ScanSAR SWA measurement. Rain effects on ScanSAR SWA measurements include atmospheric effects (attenuation and backscattering) and surface effects. Rain surface effects on C-band SAR measurements can dominate the surface backscatter in moderate to heavy rains. For C-band, the rain surface effect varies with incidence angle. Using a simple wind/rain backscatter model and the collocated data set, we quantitatively analyze different rain effects on the ScanSAR measurements for three different incidence angle ranges and estimate the model coefficients. The SAR-derived σ_{surf} is found to be consistent with the scatterometer-derived model when the polarization difference between HH and VV polarizations is considered. While only three typical rain cells are analyzed in any detail in this chapter, more rain cells on the ScanSAR SWA images can be analyzed using the same approach to develop a more accurate model.

Chapter 6

Summary and Conclusion

This dissertation addresses rain effects on C-band scatterometer and SAR measurements, and presents a method for improving wind estimates in the presence of rain. Chapter 1 briefly describes the motivation and contributions of this dissertation. Chapter 2 provides background in scatterometry and describes rain estimation using weather radar data. Rain effects on C-band scatterometer data are analyzed in Chapter 3, and a wind/rain backscatter model is developed with the aid of TRMM precipitation radar data. The model is validated to be accurate within 3 dB. Using the wind/rain backscatter model, a method of simultaneously retrieving wind and rain from scatterometer data is developed, evaluated, and validated in Chapter 4. The rain effect on conventional wind-only retrieval is also described in the same chapter. A recalibration method is developed for RADARSAT-1 ScanSAR wind retrieval using the NOAA H*wind mode in Chapter 5. Using collocated NEXRAD rain observations, rain effects on ScanSAR data at various incidence angles are analyzed and modeled.

The main conclusion of the dissertation is that rain surface effects on C-band scatterometer and SAR measurements are significant and can be modeled by a wind/rain backscatter model. Further, rain-induced error in the C-band wind retrieval process can be reduced by using a simultaneous wind/rain retrieval method. These results are a significant contribution to C-band scatterometer wind retrieval and SAR wind retrieval.

6.1 Future Research

There are a number of areas of future research that may improve the results presented here. Some of these are described below.

6.1.1 Improving Ambiguity Selection of SWRR

The ambiguity selection method introduced in Chapter 4 is designed for wind-only retrieval without considering the rain information. Further research is needed to add rain rate in the algorithm for optimal performance in raining areas.

6.1.2 Application of Rain Model to ASCAT on Met-Op A

The Met-Op A satellite, which carries the ASCAT instrument, provides high-precision backscatter measurements over the ocean. Compared to ESCAT, ASCAT's measurements have higher incidence angles and are expected to be more sensitive to rain. Applying SWRR in ASCAT wind retrieval can benefit ASCAT wind retrieval.

In this dissertation, the MLE retrieval method similar to Ku-band scatterometer technique is used in the SWRR. A method of transformation to z space ($z = \sigma^{0.625}$) has been shown to be ideal for the wind-only inversion of C-band scatterometer wind retrieval. A SWRR using this method would achieve better wind and rain estimates in raining areas. In addition, Bayesian or MAP method can be implemented to improve the SWRR.

As mentioned in Section 4, it is more beneficial to implement SWRR only in raining areas. A Quality Control (QC) algorithm, which can determine raining areas, has been developed for ESCAT. Combining SWRR with the QC algorithm can provide an operational mode for implementing SWRR.

6.1.3 Exploratory Study of SAR Rain Retrieval in Hurricanes

The rain effect on SAR measurements is modeled at high and low incidence angles. Based on this model, the rain retrieval method may be developed for hurricanes, assuming the wind speed is almost constant in a small area. Although the proposed model function is not well-validated, further exploratory study of rain retrieval from SAR measurement over the ocean is very useful and necessary.

6.1.4 Model-Based MLE SAR Wind Retrieval in Hurricanes

Due to the saturation of CMOD5, the performance of SAR wind retrieval is degraded in high winds. In order to provide a more consistent wind field, a model-based MLE can be developed based on parametric hurricane vortex models (such as the Holland model). Model-based MLE would improve wind estimates in high winds or raining areas, although fine-scale events may be smoothed.

Bibliography

[1] JPL, *QuickSCAT Science Data Product User's Manual*. Pasadena, CA, Tech. Rep. D-18053: California Inst. Technol., Jet Propulsion Lab., 2001. 2, 18, 55, 56

[2] J. N. Huddleston and B. W. Stiles, "A multi-dimensional histogram rain flagging technique for SeaWinds on QuickSCAT," in *Proc. IEEE International Geoscience Remote Sensing Symposium*, vol. 3, Honolulu, HI, 2000, pp. 1232–1234. 2, 3, 58

[3] C. A. Mears, D. Smith, and F. J. Wentz, "Detecting rain with QuikSCAT," in *Proc. IEEE International Geoscience and Remote Sensing Symposium*, Honolulu, HI, 2000, pp. 1235–1237. 2

[4] B. W. Stiles and S. Yueh, "Impact of rain on spaceborne Ku-band wind scatterometer data," *IEEE Trans. Geosci. Remote Sens.*, vol. 40, no. 9, pp. 1973–1983, 2002. 3, 62

[5] D. E. Weissman, M. A. Bourassa, and J. Tongue, "Effects of rain rate and wind magnitude on SeaWinds scatterometer wind speed errors," *Journal of Atmospheric and Oceanic Technology*, vol. 19, pp. 738–746, 2002. 3

[6] J. Tournadre and Y. Quilfen, "Impact of rain cell on scatterometer data: 1. theory and modeling," *Journal of Geophysical Research*, vol. 108, no. C7, 3225, 2003. 3

[7] D. W. Draper and D. G. Long, "Evaluating the effect of rain on SeaWinds scatterometer measurements," *Journal of Geophysical Research*, vol. 109, no. C02005, 2004. 3, 25, 26, 28, 29, 30, 31, 32, 33, 35, 39, 48, 53, 56, 62, 69

[8] ——, "Simultaneous wind and rain retrieval using SeaWinds data," *IEEE Trans. Geos. Remote Sens.*, vol. 42, no. 7, 2004. 3, 65

[9] C. Melsheimer, W. Alpers, and M. Gade, "Simultaneous observations of rain cells over the ocean by the synthetic aperture radar aboard the ERS satellites and by surface-based weather radars," *Journal of Geophysical Research*, vol. 106, no. C3, pp. 4665–4677, 2001. 3, 25, 26, 53, 84, 100, 102

[10] J. Horstmann, W. Koch, S. Lehner, and R. Tonboe, "Wind retrieval over the ocean using synthetic aperture radar with C-band HH polarization," *IEEE Trans. Geosci. Remote Sens.*, vol. 38, no. 5, 2000. 3, 87, 90

[11] C. Nie and D. G. Long, "A C-band wind/rain backscatter model," *IEEE Trans. Geosci. Remote Sens.*, vol. 45, no. 3, pp. 621–631, 2007. 3, 5, 53, 62, 65, 66, 69, 81, 84, 100, 101, 110

[12] F. T. Ulaby, R. K. Moore, and A. K. Fung, *Microwave Remote Sensing Active and Passive.* Addison-Wesley Publishing Company, 1982, vol. I. 9, 20, 104, 105

[13] ——, *Microwave Remote Sensing Active and Passive.* Addison-Wesley Publishing Company, 1982, vol. II. 10, 33

[14] E. Attema, "The active microwave instrument onboard the ERS-1 satellite," in *Proc. IEEE International Geoscience Remote Sensing Symposium*, vol. 79, 1991, pp. 791–799. 13, 27

[15] H. Hersbach, A. Stoffelen, and S. de Hann, "A improved C-band scatterometer ocean geophysical model function: CMOD5," *Journal of Geophysical Research*, vol. 112, no. C3, 2007. 13, 28, 67

[16] T. E. Oliphant and D. G. Long, "Accuracy of scatterometer-derived winds using the Cramer-Rao bound," *IEEE Trans. Geos. Remote Sens.*, vol. 37, no. 6, pp. 2642–2652, 1999. 16, 56

[17] D. G. Long and M. W. Spencer, "Radar backscatter measurement accuracy for a spaceborne pencil-beam wind scatterometer with tansmit modulation," *IEEE Trans. Geosci. Remote Sens.*, vol. 35, pp. 102–114, 1997. 18, 56

[18] A. C. M. stoffelen and D. L. T. Anderson, "Scatterometer data interpretation: measurement space and inversion," *J. Atmos. Oceanic Technol.*, vol. 14, pp. 1298–1313, 1997. 18, 56, 64, 65, 80

[19] R. J. Doviak and D. S. Zrnic, *Doppler Radar and Weather Observations.* Florida: Academic Press INC., 1984, vol. 1. 19, 89, 107

[20] T. Kozu, T. Kawanishi, H. Kuroiwa, and et al., "Development of precipitation radar on-board the tropical rainfall measuring mission (TRMM) satellite," *IEEE Trans. Geosci. Remote Sens.*, vol. 39, pp. 102–116, 2001. 21, 28

[21] T. Iguchi, T. Kozu, R. Meneghini, J. Awaka, and K. Okamoto, "Rain profiling algorithm for the TRMM precipitation radar," *J. Appl. Meteorol.*, vol. 39, pp. 2038–2052, 2000. 22, 28

[22] I. I. Lin, D. Kasilingam, W. Alpers, T. K. Lim, H. Lim, and V. Khoo, "A quantitative study of tropical rain cells from ERS SAR imagery," in *Proc. IEEE International Geoscience and Remote Sensing Symposium (Singapore).* Piscataway, N.J.: IEEE Press, 1997, pp. 1527–1529. 25

[23] D. Kasilingam, I. I. Lin, H. Lim, V. Khoo, W. Alpers, and T. K. Lim, "Investigation of tropical rain cells with ERS SAR imagery and ground-based weather radar," in *Proc. The Third ERS Symposium.* Eur. Space Agency Spec. Publ. Sp-14, 1997, pp. 1603–1608. 25

[24] N. Braun, M. Gade, and P. A. Lange, "Radar backscattering measurements of artificial rain impinging on a water surface at different wind speeds," in *Proc. IEEE International Geoscience and Remote Sensing Symposium.* Piscataway, N.J.: IEEE Press., 1999, pp. 1963–1965. 25

[25] L. F. Bliven, P. W. Sobieski, and C. Craeye, "Rain generated ring-waves: measurements and modeling for remote sensing," *Int. J. Remote Sensing*, vol. 18, no. 1, pp. 221–228, 1997. 25, 26

[26] L. F. Bliven, J. P. Giovanangeli, and G. Norcross, "Scatterometer directional response during rain," in *Proc. IEEE International Geoscience Remote Sensing Symposium*, Inst. of Electr. and Electr. Eng, Vancouver, B.C., Can., 1989. 26

[27] A. Persson and F. Grazzini, *User guide to ECMWF forecast products.* European Centre for Medium Range Weather Forecasts, 2005. 27

[28] L. J. Battan, *Radar observation of the atmosphere.* The University of Chicago Press, 1973. 32, 33, 103, 104

[29] M. P. Wand and M. C. Jones, *Kernel Smoothing.* Chapman & Hall, 1995. 36

[30] R. F. Contreras and W. J. Plant, "Surface effect of rain on microwave backscatter from the ocean: measurements and modeling," *Journal of Geophysical Research*, vol. 111, p. C08019, 2006. 53

[31] M. Portabella and A. Stoffelen, "Rain detection and quality control of seawinds," *J. Atm.Oceanic Technol.*, vol. 18, pp. 1171–1183, 2001. 53

[32] ——, "A comparison of knmi quality control and jpl rain flag for seawinds," *Canadian Journal of Remote Sensing*, vol. 28, pp. 424–430, 2002. 53

[33] J. Figa and A. Stoffelen, "On the assimilation of ku-band scatterometer winds for weather analysis and forecasting," *IEEE Transactions on Geoscience and Remote Sensing*, vol. 38, pp. 1893–1902, 2000. 53

[34] D. W. Draper and D. G. Long, "Assessing the quality of SeaWinds rain measurements," *IEEE Trans. Geos. Remote Sens.*, vol. 42, no. 7, 2004. 58, 67

[35] M. W. Spencer and M. Shimada, "Effect of rain on Ku-band scatterometer wind measurements," in *Proc. IEEE International Geoscience and Remote Sensing Symposium*, vol. 3, 1991, pp. 1285–1288. 62

[36] S. J. Shaffer, R. S. Dunbar, S. V. Hsiao, and D. G. Long, "A median-filter-based ambiguity removal algorithm for NSCAT," *IEEE Trans. Geosci. Remote Sens.*, vol. 29, pp. 167–174, 1991. 64

[37] M. Portabella and A. Stoffelen, "Scatterometer backscatter uncertainty due to wind variability," *IEEE Trans. Geos. Remote Sens.*, vol. 44, no. 11, 2006. 65

[38] J. Goldhirsh, "Rain cell size statistics as a function of rain rate for attenuation modeling," *IEEE Trans. Antennas Propag.*, pp. 799–801, 1983. 66

[39] C. C. Wackerman, C. L. Rufenach, R. Schuchman, J. A. Johnnessen, and K. Davidson, "Wind vector retrieval using ERS-1 synthetic aperture radar imagery," *Journal of Geophysical Research*, vol. 34, pp. 1343–1352, 1996. 83

[40] P. W. Vachon and F. W. Dobson, "Validation of wind vector retrieval from ERS-1 SAR images over the ocean," in *Proc. Global Atmos. Ocean Syst.*, vol. 5, 1996, pp. 177–187. 83, 93

[41] S. Lehner, J. Horstmann, W. Koch, and W. Rosenthal, "Mesoscale wind measurements using recalibrated ERS SAR images," *Journal of Geophysical Research*, vol. 103, pp. 7847–7856, 1998. 83

[42] R. K. Raney, A. P. Luscombe, E. J. Langham, and S. Ahmed, "RADARSAT," in *Proc. IEEE International Geoscience and Remote Sensing Symposium*, 1991, pp. 839–849. 84, 86

[43] D. Atlas, "Footprints of storms on the sea: A view from spaceborne synthetic aperture radar," *Journal of Geophysical Research*, vol. 99, pp. 7961–7969, 1994. 84, 100

[44] W. Albright, *Calibration report for RADARSAT ScanSAR wide A on the ScanSAR processor.* Alaska SAR facility, Mar. 2004. 87

[45] N. Shepherd, *Extraction of beta nought and sigma nought from RADARSAT CDPF products.* Ottawa, ON, Canada: Can. Space Agency, 1998. 87

[46] M. D. Powell, S. H. Houston, L. R. Amat, and N. Morisseau-Leroy, "The HRD real-time hurricane wind analysis system," *J. Wind Engineer. and Indust. Aerodyn*, pp. 53–64, 1998. 88

[47] M. D. Powell, S. H. Houston, and T. A. Reinhold, "Hurricane Andrew's landfall in south Florida part I : Standardizing measurements for documentation of surface wind fields," *Wea. Forecast*, vol. 11, pp. 304–328, 1996. 88

[48] C. M. H. Unal, P. Snooji, and P. J. F. Swart, "The polarization-dependent relation between radar backscatter from the ocean surface and surface wind vectors at frequencies between 1 and 18 GHz," *IEEE Trans. Geosci. Remote Sens.*, vol. 29, pp. 621–626, 1991. 91, 93

[49] A. A. Mouche, D. Hauser, J. F. Daloze, and C. Guerin, "Dual-polarization measurements at C-band over the ocean: results from airborne radar observations and comparison with ENVISAT ASAR data," *IEEE Trans. Geos. Remote Sens.*, vol. 43, no. 4, 2005. 91

[50] D. R. Thompson, T. M. Elfouhaily, and B. Chapron, "Polarization ratio from microwave backscattering from the ocean surface at low to moderate incidence angles," in *Proc. IEEE International Geoscience and Remote Sensing Symposium*, Seattle, WA, 1998. 91, 95

[51] F. M. Monaldo, R. C. Beal, W. G. Pichel, and P. Clemento-Colon, "Comparison of SAR-Derived wind speed with model predictions and ocean buoy measurements," *IEEE Trans. Geos.Remote Sens.*, vol. 39, no. 12, pp. 2587–2600, 2001. 93

[52] F. M. monaldo, C. C. Wackerman, and P. Clemente-Colon, "A two scale model to predict C-band VV and HH normalized radar cross section values over the ocean," *Can. J. Remote Sens.*, vol. 28, no. 3, pp. 367–384, 2002. 93

[53] T. Elfouhaily, "Physical modeling of electromagnetic backscatter from the ocean surface; application to retrieval of wind fields and wind stress by remote sensing of the marine atmospheric boundary layer," Ph.D. dissertation, IFREMER, Plouzane, France, 1997. 93

[54] A. A. Mouche, D. Hauser, J. F. Daloze, and C. Guerin, "Dual-polarization measurements at C-band over the ocean: results from airborne radar observations and comparison with ENVISAT ASAR data," *IEEE Trans. Geos.Remote Sens.*, vol. 43, no. 4, 2005. 93

[55] J. Gower and S. Skey, "Wind, slick, and fishing boat observations with RADARSAT ScanSAR," *Johns Hopkins APL Technical Digest*, vol. 21, no. 1, 2000. 95

[56] D. Atlas, "Origin of storm footprings on the sea seen by synthetic aperture radar," *Science*, vol. 266, pp. 1364–1366, 1994. 100

[57] L. M. Mitnik, "Mesoscale coherent structures in the surface wind field during cold air outbreaks over the eastern seas from the satellite side looking radar," *La Mer*, vol. 30, pp. 297–314, 1992. 100

[58] J. Hallet and L. Christensen, "Splash and penetration of drops in water," *J. Rech. Atmos.*, vol. 18, pp. 225–242, 1984. 102

[59] Y. Fujiyoshi, T. Endoh, T. Yamada, K. Tsuboki, Y. Tachibana, and G. Wakahama, "Determination of a Z-R relationship for snowfall using a radar and high sensitivity snow gauges," *Journal of Applied Meteorology*, vol. 29, pp. 147–152, 1990. 105